

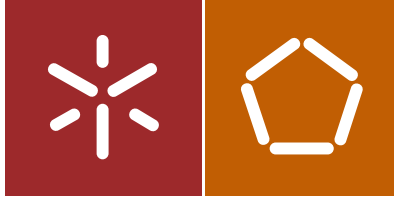


Bruno Miguel Faria do Vale

Development of a coextrusion system of multifunctional filaments for the production of high performance ropes

Universidade do Minho
Escola de Engenharia





Universidade do Minho
Escola de Engenharia

Bruno Miguel Faria do Vale

Development of a coextrusion system of
multifunctional filaments for the
production of high performance ropes

Dissertação de Mestrado
Ciclo de Estudos Integrados Conducentes ao
Grau de Mestre em Engenharia de Polímeros

Trabalho efetuado sob a orientação de
Professor Doutor João Miguel Nóbrega
Doutor Célio Bruno Pinto Fernandes
Mestre Fernando Eblagon

DECLARAÇÃO

Nome:

Bruno Miguel Faria do Vale

Endereço eletrónico: brunofaria_777@hotmail.com Telefone: 912884791

Número do Bilhete de Identidade: 143100297ZY5

Título da dissertação:

Development of a multifunctional filament coextrusion system for producing high performance ropes

Orientador(es):

Professor Doutor João Miguel Amorim Novais Costa Nóbrega

Doutor Célio Bruno Pinto Fernandes

Mestre Fernando Eblagon Ano de conclusão: 2016

Designação do Mestrado ou do Ramo de Conhecimento do Doutoramento:

Mestrado Integrado em Engenharia de Polímeros

DE ACORDO COM A LEGISLAÇÃO EM VIGOR, NÃO É PERMITIDA A
REPRODUÇÃO DE QUALQUER PARTE DESTA TESE/TRABALHO

Universidade do Minho, ___ / ___ / _____

Assinatura:

ACKNOWLEDGMENTS

The execution of this MSc thesis was only possible due to the contribution and guidance of several people.

Firstly, I want to sincerely express my gratitude to my advisers Professor Doctor João Miguel Nóbrega, Doctor Célio Fernandes and Master Fernando Eblagon. To Professor Doctor João Miguel Nóbrega and Master Fernando Eblagon I want to thank for the guidance and support during this project and for making available all the resources needed to perform this MSc project. I thank to Doctor Célio Fernandes for the patience demonstrated in help me solving all the many problems and challenges faced and for the knowledge provided regarding the OpenFOAM® framework computational library.

I also want to thank to all the people in Lankhorst for the demonstrated sympathy and the knowledge provided.

In addition, I like to thank all my co-workers in Polymer Engineering Department of the University of Minho for the support and friendship. I want to highlight Ananth Rajkumar for providing the tool required to simulate the extrusion process and to António Abreu for providing the experimental results needed to validate the solvers used.

To my closest friends who accompanied me over these five years, especially to Miguel Coelho and Melisa Freitas, I am so grateful for all the support and friendship given to me.

Lastly but not least, I would like to express my gratitude to my family. I thank to my father Fernando, my mother Joana and my brother Rui for the support that they give to me, for the patient and for always believe in me. I also want to dedicate this thesis to my grandmother Maria, who sadly passed away, but I know that she is very proud and she will always guide me wherever she is.

To all a big thank you.

ABSTRACT

Due to the increasingly demand on performance, several products that were in the past manufactured using just one material, are nowadays designed to incorporate more than one. This allows to take advantage of the specific properties of each material employed, like mechanical, barrier, chemical resistance, etc. However, the difficulties to anticipate the flow of several rheologically complex materials inside the production tools, are significantly increased when more than one material flows in the same channel.

Based on the above, numerical modelling tools may play an important role to support the designer's activity, especially when dealing with products for which there is no previous experience. This MSc project aims to evaluate the capability of using OpenFOAM[®] framework to support the design of coextrusion processing tools and to develop a new semi-industrial filament coextrusion die. The numerical code assessment was started with verification studies, where numerical results obtained with the OpenFOAM[®] framework code were compared with data available in the scientific literature. Subsequently the assessment was performed with two experimental case studies, corresponding to extrusion dies to produce simple and coextruded filaments. The results obtained show clearly that OpenFOAM[®] was able to capture several flow effects, namely the interface location, and thus seems to be adequate to support the design of coextrusion production tools. The final part of the work comprised the design of a semi-industrial filament coextrusion die capable of produce filaments with different formulations, at a relative wide range of mass flow rates, which was done with the support of the OpenFOAM[®] computational library.

Keywords

Filament, Coextrusion, Coextrusion Die Design, OpenFOAM[®], Verification, Experimental Assessment

RESUMO

Devido à crescente procura de melhores propriedades, muitos produtos que no passado eram produzidos só com um material, são nos dias de hoje projetados para serem constituídos por mais do que um material. Este facto permite tirar partido de propriedades específicas de cada material utilizado, como propriedades mecânicas, barreira, resistência química, etc. Contudo, as dificuldades em antecipar o fluxo de vários materiais reologicamente complexos dentro das ferramentas de produção são significativamente aumentadas quando mais do que um material flui no mesmo canal.

Baseado no anteriormente exposto, as ferramentas de modelação numérica podem desempenhar um papel importante no apoio à atividade do projetista, especialmente quando aplicadas em produtos nos quais não existe experiência prévia. Este projeto de mestrado pretende avaliar a capacidade em usar a biblioteca computacional OpenFOAM[®] no auxílio à conceção de ferramentas para o processo de coextrusão e em desenvolver uma nova cabeça de coextrusão de filamento semi-industrial. A avaliação do código numérico começou com estudos de verificação, conseguidos pela comparação de resultados obtidos através do OpenFOAM[®] com dados disponíveis na literatura científica. Subsequentemente a avaliação foi realizada para dois casos de estudo experimentais, correspondentes a cabeças de extrusão utilizadas para produzir filamentos simples e coextrudidos. Os resultados obtidos demonstram que a biblioteca computacional OpenFOAM[®] é capaz de capturar vários efeitos no fluxo, nomeadamente a localização da interface, parecendo assim adequado para auxiliar a conceção de ferramentas de coextrusão. A última tarefa do projeto consistiu na conceção de uma cabeça de coextrusão de filamentos semi-industrial capaz de produzir filamentos com diferentes formulações, numa relativa vasta gama de débitos mássicos, conseguida com a ajuda da biblioteca computacional OpenFOAM[®].

Palavras-Chave

Filamento, Coextrusão, Conceção de Cabeças de Coextrusão, OpenFOAM[®], Verificação, Avaliação Experimental

Contents

Acknowledgments	iii
Abstract	v
Resumo	vii
List of Figures	xi
List of Tables.....	xv
List of Abbreviations and Acronyms	xvii
1. Introduction.....	1
1.1 State of the art.....	1
1.1.1 Filament extrusion and coextrusion	1
1.1.2 Filament coextrusion die	4
1.1.3 Rheological defects	6
1.1.4 Interface distortions in coextrusion	9
1.1.5 The importance of Computer Aided Engineering in die design.....	11
1.1.6 OpenFOAM®	13
1.2 Motivation	15
1.3 Objectives	15
1.4 Thesis structure.....	16
2. Verification case – 2D coextrusion.....	17
2.1 Geometry generation	18
2.2 Mesh generation	19
2.3 Properties of the polymeric blends	22
2.4 Boundary conditions.....	24
2.5 Results and discussion	25
3. OpenFOAM® experimental assessment.....	33
3.1 Rheological models and properties of the blends	33
3.2 Extrusion of Monofilaments.....	37
3.2.1 Geometry and operating conditions	38
3.2.2 Mesh and boundary conditions	39
3.2.3 Results and discussion.....	42
3.3 Coextrusion of the blends	46

3.3.1	Geometry and operation conditions	47
3.3.2	Mesh and boundary conditions	49
3.3.3	Results and discussion.....	52
4.	Design of a semi industrial multifilament coextrusion die	63
4.1	Die constructive solution	63
4.2	Mesh and boundary conditions.....	67
4.3	Results and discussion	70
5.	Conclusions and future work	91
5.1	Conclusions	91
5.2	Future work.....	92
	Bibliographic references	93
	Appendixes.....	97
	Appendix A – Developed flow in the more refined mesh created using <i>blockMesh</i>	97
	Appendix B – Interface in cases with mesh created using <i>blockMesh</i>	97
	Appendix C – Streamlines in cases with mesh created using <i>blockMesh</i>	98
	Appendix D – Velocity profile and pressure field in Cases 3, 4 and 5	99
	Appendix E – 2D drawings of all components of the filament coextrusion die.....	101

LIST OF FIGURES

Figure 1 - Scheme of a typical filament extrusion line adapted from (Giles, Wagner, & Mount, 2004).....	2
Figure 2 - Scheme of the filament coextrusion line used by Glauß and his co-workers (Glauß et al., 2013).....	4
Figure 3 - Cross section of a sheath-core filament.....	5
Figure 4 - Monofilament coextrusion die used by Martins and his co-workers (Martins et al., 2014).....	5
Figure 5 - Scheme of the rearrangement of the velocity profile at the die exit (Carneiro & Nóbrega, 2012).....	7
Figure 6 - The most frequent forms of melt fracture (Rauwendaal, 2014).	7
Figure 7- Illustration of die drool formation, accumulation and eventual removal by the extrudate (Carneiro & Nóbrega, 2012).	8
Figure 8 - Overall structure of OpenFOAM® (Greenshields, 2015).....	14
Figure 9 - Schematic representation of the double-layer coextrusion die used by Hannachi and Mitsoulis (Hannachi & Mitsoulis, 1993) (all design measures are given in mm).	17
Figure 10 - Geometry obtained with the SolidWorks CAD software: a) frontal view; b) isometric view.	18
Figure 11 - Example of the eight vertices points that define one single block of the geometry.	19
Figure 12 - Meshes created with cfMesh: (a) coarser mesh (M1) and (b) more refined mesh (M4).....	20
Figure 13 - Meshes created with blockMesh: (a) coarser mesh (M1) and (b) more refined mesh (M4).....	21
Figure 14 - Rheological curves of the polymer blend P2 and P3 (Hannachi & Mitsoulis, 1993).	23
Figure 15 - Initial domain distribution used for all the computational runs: the red field represents the P2 mixture and the blue field represents the P3 mixture.	25
Figure 16 - Steady state flow for 2D coextrusion case study, for the more refined mesh created using cfMesh in: a) Case 1; b) Case 2; c) Case 3.	26
Figure 17 - Interface coordinates for Case 1 (mesh created using cfMesh).....	27
Figure 18 - Interface coordinates for Case 2 (mesh created using cfMesh).....	27

Figure 19 - Interface coordinates for Case 3 (mesh created using cfMesh).....	28
Figure 20 - Interface coordinates for Case 1 (mesh created using blockMesh).....	28
Figure 21 - Streamlines obtained by Hannachi and Mitsoulis (Hannachi & Mitsoulis, 1993).	30
Figure 22 - Representation of the streamlines (coloured according with the velocity intensity) for the more refined mesh created using cfMesh in: a) Case 1; b) Case 2; c) Case 3.....	31
Figure 23 - Viscosity curves using the Carreau model for Blend A.	35
Figure 24 - Viscosity curves using the Carreau model for Blend B.	35
Figure 25 - Viscosity curves using the Carreau model for Blend A and B at 230°C.	36
Figure 26 - 3D geometry of the extrusion die used in the extrusion process.	38
Figure 27 - Geometry of the extrusion die flow channel.	38
Figure 28 - Slice of the flow channel used in the simulations: (a) frontal view and (b) isometric view.	40
Figure 29 - Meshes used in the simulations of the extrusion of the filaments: (a) coarser mesh (M1) and (b) more refined mesh (M3).	41
Figure 30 - Evolution of the residuals along the simulated time in the extrusion process.....	42
Figure 31 - Pressure field predicted by the code along the die during the extrusion process of the Blend A (a) and Blend B (b).	44
Figure 32 - Velocity field predicted by the code along the die during the extrusion process of the Blend A (a) and Blend B (b).	44
Figure 33 - Temperature field predicted by the code along the die during the extrusion process of the Blend A (a) and Blend B (b).	45
Figure 34 - 3D model of the coextrusion die modules used to produce the multifunctional filaments.	47
Figure 35 - Geometry of the flow channels of the original coextrusion die.	47
Figure 36 - Geometry of the coextrusion die flow channels using Configuration 1.....	48
Figure 37 - Geometry of the coextrusion die flow channels using Configuration 2.....	48
Figure 38 - Meshes created using Configuration 2 geometry: (a) coarser mesh (M1) and (b) more refined mesh (M3).....	50
Figure 39 - Interface between the two materials at the die exit at (a) 7 seconds and at (b) 9 seconds for configuration 1.	52
Figure 40 - Flow along one transversal section of the coextrusion die using configuration 1.	52
Figure 41 - Interface between the two materials at the die exit at (a) 7 seconds and at (b) 9 seconds for configuration 2.	53
Figure 42 - Flow along one transversal section of the coextrusion die using configuration 2.	53

Figure 43 - Evolution of the residuals along the simulated time in the coextrusion process...	54
Figure 44 - Location of the four points of the domain used.....	55
Figure 45 - Interface location between the two materials at 2.5 seconds (a), at 4.5 seconds (b) and at 5.5 seconds (c).	56
Figure 46 - Pressure drop along the coextrusion die obtained with the more refined mesh. ...	56
Figure 47 - Pressure in function of the mesh cell size.	58
Figure 48 - Interface location at the outlet in each mesh used.	59
Figure 49 - Interface shape obtained using the extrapolated parameters.	61
Figure 50 - Microscopy picture of the produced filaments (Abreu, To be published).	61
Figure 51 - Assembly of all the components that composes the die that Lankhorst owns.	64
Figure 52 - Design of the multifilament coextrusion die channels for Solution 1.	64
Figure 53 - Design of the multifilament coextrusion die channels for Solution 2.	65
Figure 54 - Overall view of the 3D model of the designed die (a) and bottom view of the 3D model of the designed die (b).	66
Figure 55 - Typical geometry of the distributor used to create the mesh.....	67
Figure 56 - Example of a typical mesh used in the simulations.....	68
Figure 57 - Evolution of the residuals along the simulated time in the coextrusion process...	71
Figure 58 - Location of the four points of the domain used.....	71
Figure 59 - Representation of the undeveloped flow at: (a) 1 second and (b) 4 seconds.	72
Figure 60 - Representation of the developed flow at: (a) 4.5 second and (b) 6 seconds.	73
Figure 61 - Distributor created in the first iteration: geometry (a) and flow of the blends in the distributor (b).....	74
Figure 62 - Distributor created in the sixth iteration: geometry (a) and flow of the blends in the distributor (b).....	74
Figure 63 - Representation of the distributor used in the design of the die	76
Figure 64 - Distributor created in the last iteration: geometry (a) and flow of the materials in the distributor (b).....	76
Figure 65 - Interface location with an angle of 60° and 70° in the convergent channel of the die.	77
Figure 66 - Pressure drop in the two distributors in study: (a) with an angle of 60° and (b) with an angle of 70° in the convergent channel.	77
Figure 67 - Interface location and graphical representation of the equations for the Reference case.	80
Figure 68 - Interface location and graphical representation of the equations for Case 1.....	80

Figure 69 - Velocity profile along the distributor in the Reference case.	83
Figure 70 - Pressure field along the distributor in the Reference case.....	83
Figure 71 - Velocity profile along the distributor in Case 1.	83
Figure 72 - Pressure field along the distributor in Case 1.....	84
Figure 73 - Interface location in Case 2: (a) rupture of the interface and (b) instabilities in the die parallel zone.	85
Figure 74 - Interface location and graphical representation of the equations for Case 3.....	85
Figure 75 - Interface location and graphical representation of the equations for Case 4.....	86
Figure 76 - Interface location and graphical representation of the equations for Case 5.....	86
Figure 77 - Representation of the fully developed flow for the more refined mesh created using blockMesh in: a) Case 1; b) Case 2; c) Case 3.....	97
Figure 78 - Interface coordinates for Case 2 (mesh created using blockMesh).....	97
Figure 79 - Interface coordinates for Case 3 (mesh created using blockMesh).....	98
Figure 80 - Representation of the streamlines for the more refined mesh created using blockMesh in: a) Case 1; b) Case 2; c) Case 3.....	98
Figure 81 - Velocity profile along the distributor in Case 3.	99
Figure 82 - Pressure field along the distributor in Case 3.....	99
Figure 83 - Velocity profile along the distributor in Case 4.	99
Figure 84 - Pressure field along the distributor in Case 4.....	100
Figure 85 - Velocity profile along the distributor in Case 5.	100
Figure 86 - Pressure field along the distributor in Case 5.....	100
Figure 87 - 2D drawing of the filament coextrusion die frame.....	101
Figure 88 - 2D drawing of the module 1 of the filament coextrusion die.....	102
Figure 89 - 2D drawing of the module 2 of the filament coextrusion die.....	102
Figure 90 - 2D drawing of the module 3 of the filament coextrusion die.....	102
Figure 91 - 2D drawing of the module 4 of the filament coextrusion die.....	102
Figure 92 - 2D drawing of the seal module of the filament coextrusion die.....	102
Figure 93 - 2D drawing of the filament coextrusion die cover.	102

LIST OF TABLES

Table 1 - Relevant data for all the meshes generated with cfMesh.....	20
Table 2 - Relevant data for all the meshes generated with blockMesh.....	22
Table 3 - Rheological constants and density of the materials for the Carreau model.....	24
Table 4 - Inlet velocities for the three cases documented in the paper.	25
Table 5 - L_1 errors for the meshes created using cfMesh and blockMesh for the three case studies.....	29
Table 6 - Rheological constants for the Carreau model.	34
Table 7 - Rheological constants for the Power Law model.	35
Table 8 - Relative content of blend materials and the properties calculated using the law of mixtures.....	36
Table 9 - Values of the thermal diffusivity coefficient and the alpha for the Blend A and B. .	37
Table 10 - Inlet velocities of the Blend A and B in the extrusion process.....	41
Table 11 - Evolution of the velocity and pressure values in three different points along the simulated time.	43
Table 12 - Pressures obtained using the simulations and experimentally in the same spot and the error between them.....	46
Table 13 - Relevant information about the meshes created using Configuration 2.	51
Table 14 - Inlet velocities of the Blend A and B in the coextrusion process.	51
Table 15 - Evolution of the velocity and pressure values in four different points along the simulated time.	55
Table 16 - Values of pressure at the die inlet, in the missing section and the corrected pressure.	57
Table 17 - Constants of the ellipse equation for all meshes and the ones calculated using the Richardson extrapolation.....	60
Table 18 - Relevant information about the example of a typical mesh used in the simulations.	69
Table 19 – Inlet velocities of the Blend A (inlet 2) and Blend B (inlet1) in the coextrusion process.....	70
Table 20 - Evolution of the velocity and pressure values in four different points along the simulated time.	72
Table 21 - Diameters and areas of the channels for each blend.	75

Table 22 - Shear rates and shear stresses developed in each of channel in all the processing conditions considered..... 79

Table 23 - Constants of the ellipse and the circumference equations for the Reference case and for Case 1. 81

Table 24 - Minimum and maximum sheath thickness of the filament for the Reference case and for Case 1. 81

Table 25 - Minimum and maximum tolerance (radius) of the interface location in Reference case and Case 1. 82

Table 26 - Constants for the ellipse and circumference equations for Cases 3, 4, and 5. 87

Table 27 - Minimum and maximum thickness of the filament sheath for Cases 3, 4 and 5... 87

Table 28 - Minimum and maximum tolerance (radius) of the interface location in Cases 3, 4 and 5. 88

LIST OF ABBREVIATIONS AND ACRONYMS

CAE – Computer Aided Engineering

CFD – Computational Fluid Dynamics

FVM – Finite Volume Method

HPC – High Performance Computing

OpenFOAM – Open Source Field Operation and Manipulation

STL – STereoLithography

1. INTRODUCTION

1.1 State of the art

1.1.1 Filament extrusion and coextrusion

The extrusion process allows the production of products usually with constant cross section. This process is applied in the processing of a wide range of materials, e.g. metal, food, chemicals substances (pharmaceutic industry) and plastic products (pipes, profiles, films, among others) (Gonçalves, 2013; Rauwendaal, 2014).

In the case of interest, which is the processing of polymeric materials, the extrusion can be subdivided in various sub techniques (pipe extrusion, profile extrusion, film extrusion and filament extrusion), which comprises specific post extrusion equipment, such as dies and calibrators (Gonçalves, 2013). The intrinsic properties of the polymers make them ideal to process by extrusion, because it is theoretically possible to obtain products with any cross section, at high production rates and quality. Thus they have been used to satisfy the constant demand of ever more complex products.

Since the main topic of this MSc project is the production of filaments, only the filament extrusion processing technique is going to be described in detail.

The filament extrusion technique is used to produce products that are employed to manufacture a wide range of objects that we use in our day life such as ropes, fishing lines, strings for racquets used in various sports, synthetic yarns, among several others (Giles, Wagner, & Mount, 2004).

A typical filament extrusion line is generally composed by an extruder, an extrusion die (mounted at the extruder exit), a water bath, godet rolls, draw ovens (heaters) and optionally a winding storage rolls. Figure 1 illustrates a typical filament extrusion line.

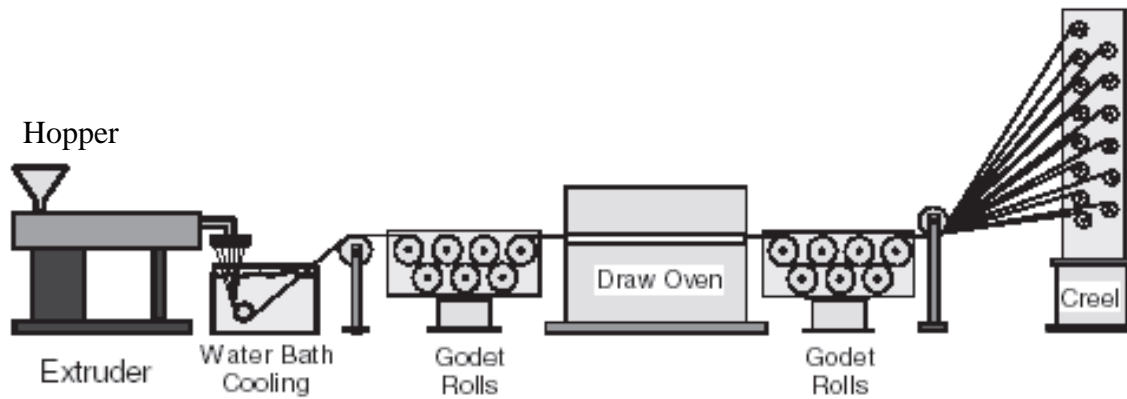


Figure 1 - Scheme of a typical filament extrusion line adapted from (Giles, Wagner, & Mount, 2004).

In this process the polymer pellets are fed to a hopper which by the action of the gravity force feeds the extruder (Gonçalves, 2013). The extruder contains one or more screws (for instance a multiscrew extruder) which rotate permanently and are responsible for the mixing, pressuring and transport of the polymeric material inside the barrel flow channel (Gonçalves, 2013). A group of heaters mounted along the extruder barrel, along with the viscous dissipation phenomena that happens when polymeric material is subjected to shearing forces, are responsible for generating the heat required to melt the polymer pellets. At the extruder outlet, the material is forced to pass through the die which transforms the circular flow from the extruder outlet into a flow with the required cross section (Gonçalves, 2013).

Frequently, between the extruder and the extrusion die a gear pump is used in order to provide a more controlled flow rate. Otherwise, due to the natural slight variations verified in processing conditions, the diameter of the filaments could vary and, thus affect negatively the product quality (Giles, Wagner, & Mount, 2004).

Subsequently, the extruded filaments are forced into a cooling bath (Ferreira et al., 2011; Giles, Wagner, & Mount, 2004). Exiting the cooling bath, the filaments are dried and passed through godet rolls (the number of godet rolls used depends of the required draw forces) which control the speed and the drying of the filaments from the die until that point in the extrusion line (Ferreira et al., 2011; Giles, Wagner, & Mount, 2004). Between the first set of godet rolls and the second set, there is a draw oven which heats the filaments, in order to promote mobility to the polymer chains which makes it easier to orientate and elongate by the action of the second set of godet rolls (Giles, Wagner, & Mount, 2004). The second godet rolls presented in Figure 1, runs at a higher linear speed

than the first set, and this determines the stretch ratio developed inside the oven, which promotes the orientation of the polymer chains in the flow direction. The effectiveness of this orientation affects directly the filament mechanical strength (Ferreira et al., 2011; Giles, Wagner, & Mount, 2004). At the end of the extrusion line, the filaments are wound, using a method that varies with the product (for instance, textiles filaments are frequently wound in bobbins) (Giles, Wagner, & Mount, 2004).

Sometimes the intrinsic properties, or cost, of the polymeric material are inadequate to satisfy the required specifications for a given application. In those cases, it is common to combine two or more different materials, or the same material with different formulations, in order to obtain products with better properties formed by well-bounded layers of those materials (Giles, Wagner, & Mount, 2004; Rauwendaal, 2014; Riquelme, 1995). This variant of the extrusion technique is called coextrusion, and consists in extruding two or more materials simultaneously to obtain a product that combines the most favourable properties of its constituents.

The driving force for the development of the coextrusion process it is the need of obtaining even more cheaper, appealing and resistant products (Giles, Wagner, & Mount, 2004; Rauwendaal, 2014). In the case of the filament industry, this process has been applied in order to obtain filaments with more and more resistance (for instance, to manufacture high strength ropes), filaments with conductive properties (Glauß et al., 2013; Martins et al., 2014), optical fibres, among others.

The filament coextrusion line is quite similar to the filament extrusion line already illustrated in Figure 1, as it can be seen in Figure 2 that presents the filament coextrusion line (in this figure are missing the water bath and the draw oven, that most of filament coextrusion lines possess) used by Glauß and his co-workers (Glauß et al., 2013). In fact, the main differences between the extrusion and the coextrusion line, in almost all the known processes, are related to the die and to the fact that more than one extruder is used, as it can be verified when comparing a typical extrusion line with the experimental setups described in the works of Martins et al (Martins et al., 2014), Wang et al (Wang et al., 2013), Dooley (Dooley, 2002) and Glauß et al (Glauß et al., 2013).

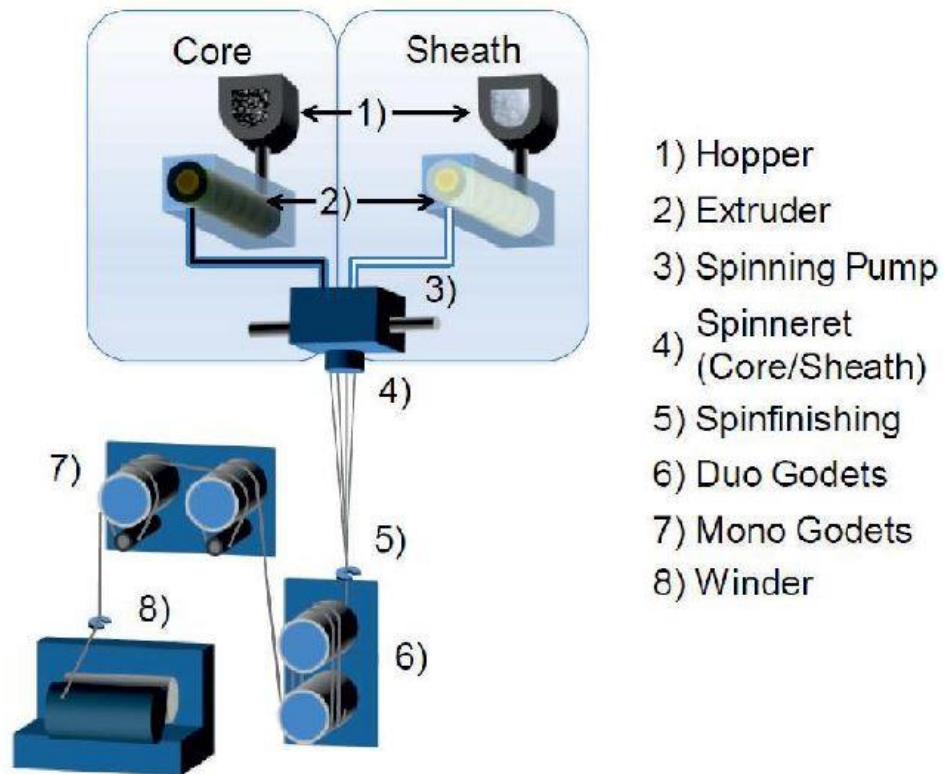


Figure 2 - Scheme of the filament coextrusion line used by Glauß and his co-workers (Glauß et al., 2013).

1.1.2 Filament coextrusion die

The filament coextrusion die is very similar to the most dies used for coating products like pipes, electric wires, among other products with circular cross section. Both of those dies allows the production of circular sheath-core products, where these are made of concentric layers of different materials and where only the polymer that forms the outer layer is in contact with the die walls, as it can be seen in Figure 3 (Martins et al., 2014; Giles, Wagner, & Mount, 2004; Riquelme, 1995). It is important to enhance that there are more types of filaments available on the market, but for the purpose of this MSc thesis only the coextrusion dies that produce sheath and core filaments are relevant.

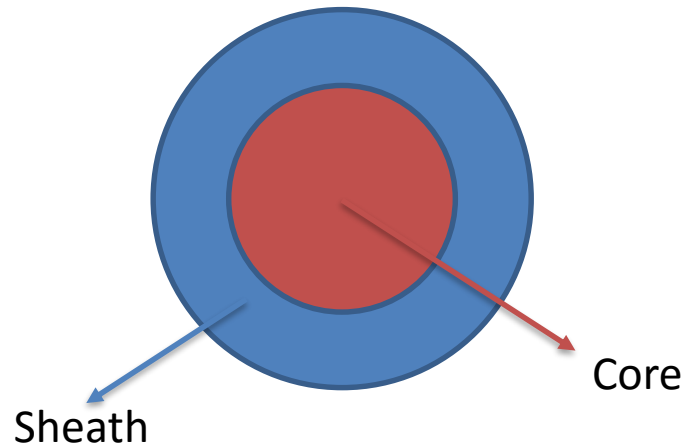


Figure 3 - Cross section of a sheath-core filament.

The main difference between the two types of dies is that in the die used for coating, a semi-finished product (like electric wire, a pipe, among others) has to be inserted in the die and the molten polymer is used to coat the product (Giles, Wagner, & Mount, 2004), and in the coextrusion dies, there is no need to do that. In fact, in this type of dies, a first material is extruded and then in the same die it is possible to combine materials with different layout, to achieve the desired distribution (Glauß et al., 2013; Martins et al., 2014).

Figure 4 illustrates a typical filament coextrusion die used by Martins and his co-workers to produce piezoelectric filaments, which is one of the very few cases of filament coextrusion documented in the literature (Martins et al., 2014).

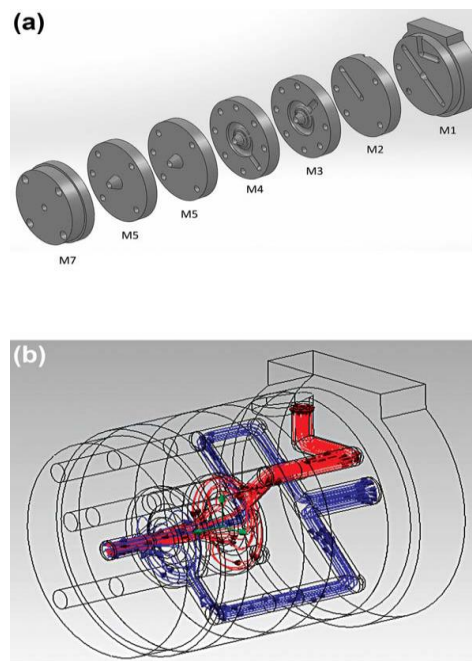


Figure 4 - Monofilament coextrusion die used by Martins and his co-workers (Martins et al., 2014).

Through the analysis of Figure 4 we can see that both materials are being extruded at the same time (which means that two extruders are being used). The first extruder feeds the material represented by the blue streamlines and then the flow is divided in two sub flows, where one is used to form the core and the other is used to form the outer layer of the filament. The middle layer is composed by the material represented by the red streamlines and is being fed by a second extruder. Finally, for each material the flow channels are guided to the main channel in specific locations, called distributors, in order to produce the filament with the required configuration (Martins et al., 2014). More than one set of distributors can be used in order to produce more than one filament at once, thus obtaining a multifilament coextrusion die.

The correct coextrusion die design is a challenging task to achieve due to the polymers complex rheological properties, therefore it is necessary to understand better the rheological defects and the interface distortion phenomena associated with the filament coextrusion, in order to design a suitable tool that produces products with the desired layer configuration.

1.1.3 Rheological defects

Shark skin

The shark skin is a surface defect that increases the roughness and decreases the gloss of the extruded product surface (Carneiro & Nóbrega, 2012; Rauwendaal, 2014; Vlachopoulos & Strutt, 2003).

This defect generally happens at the die parallel zone and/or in the die exit (Carneiro & Nóbrega, 2012; Rauwendaal, 2014; Vlachopoulos & Strutt, 2003). The main causes that are thought to lead to this defect are: the stick-slip phenomena at the flow channel wall, the high normal stresses induced at the die exit caused by the sudden acceleration of the melt, and coalescence of small voids promoted by negative pressures on the metal/polymer boundary or in the bulk (Carneiro & Nóbrega, 2012).

The most acceptable cause to explain this defect is the high normal stresses induced at the die exit, as shown in the work of Agassant and co-workers (Agassant et al., 2006; Carneiro & Nóbrega, 2012). Figure 5 shows the rearrangement of the melt

velocity profile at the die exit, where the velocity of the outer layers passes from zero (if no slip at the wall is assumed) to the average extrusion speed, which causes a sudden extensional acceleration of the melt and give rise to the development of stresses in the melt, which starts the formation of the characteristics ridges of the shark skin defect (Carneiro & Nóbrega, 2012; Rauwendaal, 2014).

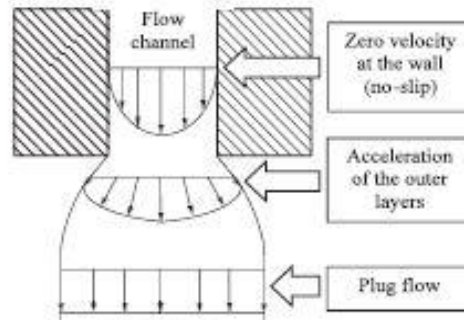


Figure 5 - Scheme of the rearrangement of the velocity profile at the die exit (Carneiro & Nóbrega, 2012).

Melt fracture

The melt fracture is a severe defect that affects the bulk extrudate and can present itself in several forms, as illustrated in Figure 6 (Carneiro & Nóbrega, 2012; Rauwendaal, 2014).

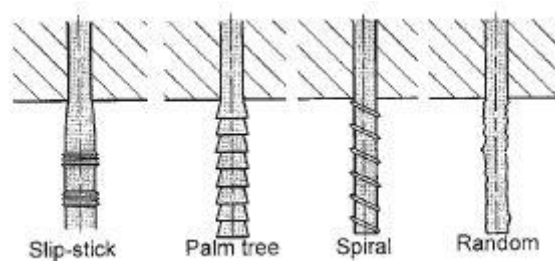


Figure 6 - The most frequent forms of melt fracture (Rauwendaal, 2014).

There is no clear agreement in the mechanism that causes this defect and in fact some authors believe that it can depend on the polymer and/or the geometry of the flow channel (Carneiro & Nóbrega, 2012; Rauwendaal, 2014). However, two mechanisms are usually referred as being the cause of melt fracture: the slip-stick phenomena at the flow channel wall and the high extensional stresses experienced by the melt during the extensional flow developed (Carneiro & Nóbrega, 2012; Rauwendaal, 2014; Vlachopoulos & Strutt, 2003). According with some studies the second cause is the more plausible, in fact the work of Agassant and co-workers showed that the onset of this defect

happens in the convergent flow zone of the die, where the melt is subjected to high extensional deformations (caused by high extensional stresses) (Agassant et al., 2006; Carneiro & Nóbrega, 2012).

Die drool

Die drool is a problem that affects most of the polymer processing techniques. In extrusion, this phenomenon leads to the progressive accumulation of material at the die exit, as illustrated in Figure 7. That material solidifies and may partially obstruct the flow of the extrudate and in severe cases, the aesthetics and the properties of the product can be affected (Carneiro & Nóbrega, 2012; Vlachopoulos & Strutt, 2003).

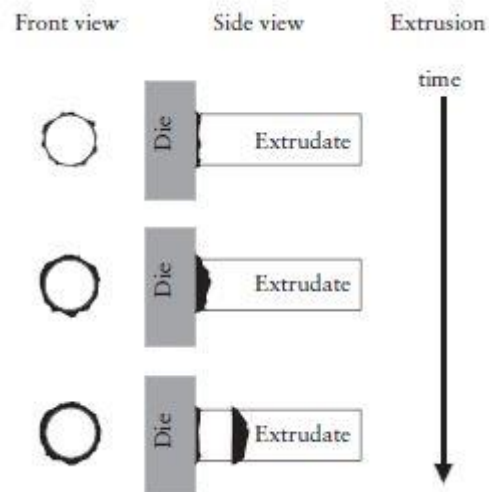


Figure 7 - Illustration of die drool formation, accumulation and eventual removal by the extrudate (Carneiro & Nóbrega, 2012).

Once this defect develops, the only way to remove the excess of material is by stopping the extrusion line and perform a cleaning operation, which obviously is a time consuming and expensive solution that should be avoided with a proper die design (Carneiro & Nóbrega, 2012; Vlachopoulos & Strutt, 2003).

Several causes for this problem have been suggested, but some of these are still under research and debate (Carneiro & Nóbrega, 2012; Vlachopoulos & Strutt, 2003). The most frequently suggested causes are the following (Carneiro & Nóbrega, 2012): (a) low molecular weight polymer species; (b) volatiles present in the melt; (c) the presence of a filler; (d) poor dispersion of pigments; (e) high draw down rates; (f) the amount and rate of extrudate-swell; (g) die exit angles, land length and land entrance size; (h)

dissimilar component viscosities; (i) die condition (including cleanliness, presence of damage, defects, etc.); (j) pressure fluctuations in screw channel; and (k) inadequate melt temperature.

The work of Zatloukal and co-workers helped to improve the characterization and understanding of the die drool phenomena. According to their experiments there are two types of die drool, the external die drool and the internal die drool (Carneiro & Nóbrega, 2012).

The external type occurs due to negative pressures that are a consequence of the elasticity of the melt and the streamline curvature, which leads to the generation of normal stresses that causes a local pressure decrease. This negative pressure may promote the accumulation and adhesion of material at the die exit and the migration and accumulation of low molecular weight species to the die exit surface (Carneiro & Nóbrega, 2012).

The internal die drool results of molecular weight fragmentation induced by the flow before the die exit, which causes the accumulation of low molecular weight species to the die walls surface (Carneiro & Nóbrega, 2012).

1.1.4 Interface distortions in coextrusion

The rheological information of the polymers is a key piece of the coextrusion die design process (Dooley, 2002). In fact, polymers are non-Newtonian materials and their viscoelastic interactions and rheological properties (like viscosity, shear rate, among others) are highly dependent on the processing conditions (temperature, flow rate, etc.), on the die channel geometry and, in coextrusion, on the position and the thickness of the layers (a surface layer experiences higher shear rates than a core layer) (Dooley, 2002; Rauwendaal, 2014).

In the following sections it will be discussed the four major causes of the interface distortion on the layers present in the coextrusion process.

Interfacial distortions due to flow instabilities

This type of interfacial distortions can cause variations on the thickness of the individual layers but the overall thickness of the product maintains constant, so it's

possible to understand that this phenomenon can lead to uneven interfaces and in severe cases intermixing between two adjacent layers may happen (Dooley, 2002).

At higher flow rates these instabilities are more noticeable, because a wave like structure begins to appear in the interface of the layers (Dooley, 2002). The main mechanism that causes this type of distortions has not been conclusively identified, but the work of Schrenk and Alfrey (Schrenk & Alfrey, 1978) showed that this type of instabilities can be correlated with critical interfacial shear stresses, being the skin-layer viscosity, the skin-to-core thickness ratio, the total extrusion rate and the die gap the main variables that influence this instability (Dooley, 2002).

Interfacial distortions from viscosity mismatch

When two materials with different viscosities are processed together, the material with the lower viscosity tends to flow to areas with higher shear rates, seeking the path of less resistance, thus tending to encapsulate the material with high viscosity, which promotes the formation of interface distortions (Dooley, 2002). In coextrusion of sheath and core filaments, this phenomenon constitutes a problem in cases where the sheath polymer is more viscous than the core polymer, since the last one tends to migrate to the walls, where the shear rate is higher, which modifies the filament cross section geometry. The main variables affecting the degree of distortion of the interface are the viscosity difference between the two materials, the shear rate and the residence time. Dooley made experiments with different materials in order to confirm the existence of interface distortion related to viscosity mismatch, and his results confirmed that phenomenon (Dooley, 2002).

Interfacial distortions from viscoelasticity

When two or more polymers with the same or similar viscosities are processed together, viscous encapsulation phenomena may be happening as Dooley showed (Dooley, 2002; Rauwendaal, 2014). With his experiments he linked this type of interfacial distortions to the development of second normal stresses in melt, as result of viscoelastic interactions (Dooley, 2002; Rauwendaal, 2014). Polymers with higher elastic components produce secondary flows that are normal to the primary flow direction, causing a greater interface distortion (Dooley, 2002).

Dooley (Dooley, 2002) conducted several experiments with different materials and die geometries and found out that this type of distortion is highly dependent of the die geometry. In circular die geometries, which is the case of the filament coextrusion die, this distortion is practically non-existent, because in this type of dies no secondary flows are observed and consequently no second normal stresses are developed in the melt.

Interfacial distortions due to the geometrical encapsulation

Another possible explanation for the interface distortion was proposed by Perdikoulis and his co-workers (Perdikoulis, Zatloukal, & Touré, 2004). They performed experiments with Newtonian fluids (the second normal stresses difference is null for this materials) wherein the viscosities were similar. They showed that interface distortions still happened in contrast with the expect results (Perdikoulis, Zatloukal, & Touré, 2004; Rauwendaal, 2014).

They called this effect geometrical encapsulation and linked it to the parabolic velocity profiles that are developed in the die flow channels. Because the velocity is higher in the centre of the channel the thickness of this layer tends to increase in this region and decrease near the walls (where the velocity is smaller), in contrast with the outer layers (Perdikoulis, Zatloukal, & Touré, 2004; Rauwendaal, 2014).

1.1.5 The importance of Computer Aided Engineering in die design

As mentioned before, the main function of the extrusion die is to transform the circular flow of the material from the extruder outlet into the required cross section of the desired product at high rate and quality (Carneiro & Nóbrega, 2012; Gonçalves, 2013; Kostic & Reifschneider, 2006). Produce at high rate and quality is often proven to be very difficult, due to the intrinsic characteristics of the polymers, produce at higher rates causes a significant loss in the quality (Carneiro & Nóbrega, 2012).

An approach to maximize the rate of production and the quality of the product is through the optimization of the process conditions and the tools involved in the process (Carneiro & Nóbrega, 2012). To perform that optimization, specifically in the dies, it

requires a deep knowledge of the polymers rheological behaviour and the phenomena that happens during the extrusion/coextrusion process (Gonçalves, 2013; Carneiro & Nóbrega, 2012; Kostic & Reifschneider, 2006). Thus, to achieve a proper tool design the following points have to be considered (Gonçalves, 2013):

- the maximum flow rate above which shark skin occurs;
- the maximum angle of convergence above which melt fracture in extension dominated flows occurs;
- the correction of the cross-section of the parallel zone to anticipate post extrusion effects (stretching, swelling and shrinkage);
- the control over both the total pressure drop and the appearance of hot spots (local increases in melt temperature) resulting from excessive viscous dissipation.

Being dependent of the knowledge and experience of the designer as stated before, the die design process is more an art than a science (Rauwendaal, 2014; Carneiro & Nóbrega, 2012; Gonçalves, 2013), wherein the die is designed following an iterative methodology, requiring several trials until reach a design capable of manufacturing products with the required geometry and quality (Rauwendaal, 2014; Gonçalves, 2013). It is easy to understand that this methodology requires a huge amount of time and resources (both material and equipment), leading to higher development times and higher costs of the products.

Advances in computational capabilities have made possible the appearance of an increasingly higher number of Computer Aided Engineering (CAE) software packages, which allows the designer to improve the design of the products/tools using computer simulations instead of experimental trials (Gonçalves, 2013; Kostic & Reifschneider, 2006), save money (there is no excess of use of the available resources) and in most of the cases, time. These software packages can also supply data for all the domain in the simulated geometry and it is possible to obtain details in specific zones of the geometry and thus obtain more accurate values for that zones, which is impossible to achieve using experimental trials (Gonçalves, 2013).

There is a wide range of CAE software products, but in die design the more relevant ones are those that allow users to make an analysis of systems where there is

fluid flow, heat transfer and other associated phenomena, and these are called Computational Fluid Dynamics (CFD) tools (Gonçalves, 2013; Kostic & Reifschneider, 2006). The CFD software products can be divided in two subcategories, the commercial and the opensource software.

Regarding the die design, mainly commercial software products like ANSYS, Polyflow, Dieflow, HyperXtrude, FLOW 2000 and PROFILECAD are being used by the designers to simulate the flow of the melt through the die in order to optimize the design (Gonçalves, 2013). Some opensource software, like the OpenFOAM[®], have shown great potential to replace the commercial software already mentioned. It has proven to be effective and adequate to solve a wide range of problems in various fields, including polymer processing. Regarding to design of dies, the OpenFOAM[®] has been used by Ananth Rajkumar and his co-workers to help the design process of profile extrusion dies (Rajkumar, et al., Accepted for publishing).

OpenFOAM[®] was used in all the simulations performed along this MSc thesis and it will be described in the next section.

1.1.6 OpenFOAM[®]

OpenFOAM[®] computational library stands for Open Source Field Operation and Manipulation and it was developed by Henry Weller and Hrvoje Jasak at the Imperial College in London in the early nineties (Wuthrich, 2007; Haider, 2013). Being OpenFOAM[®] a opensource software, the cost of the licenses are free (Stephens, 2016; Verhoeven, 2011), and it was available to the general public in 2004 under the GNU general public licence (Andersson, 2011; Wuthrich, 2007), which means that the user is free to use the source code of the software to build tools to suit his requirements and needs (Andersson, 2011; Haider, 2013; Stephens, 2016; Verhoeven, 2011) and to take advantage of all computational resources available (such as HPC units), by performing simultaneous (one in each processor) or parallel runs (Andersson, 2011; Stephens, 2016; Verhoeven, 2011). But as all opensource software, OpenFOAM[®] requires more specialized man power which can be a potential downside, due to the costs associated to the steep learning curve (Stephens, 2016). Ultimately, from a business point of view, the choice between the opensource and the commercial software is a cost/benefit/risk

analyses that considers the resources that the company possesses and the objectives to reach (Stephens, 2016).

OpenFOAM[®] framework consists of a C++ library that contains a large range of solvers, based in the Finite Volume Method (FVM), and utilities used to solve continuum mechanics problems, which concerns the stress in solids, liquids and gases along their flow and deformation (Haider, 2013; Greenshields, 2015; Wuthrich, 2007). The solvers are, like the name suggests, routines used to solve equations that represent the physical reality of one given problem using the FVM, following these basic steps (Herrerias & Izarra, 2013):

- Integration of the governing equations over all the control volumes of the domain;
- Conversion of the integral equations into a system of algebraic equations by means of discretization;
- Solution of the algebraic equations.

The utilities are applications designed to perform tasks that involve data manipulation (Greenshields, 2015). There are two types of utilities, the ones used in pre-processing, which means that they are used in the case study setup and the ones used in post-processing, helping in the analyses of the results provided by the simulations (Greenshields, 2015; Wuthrich, 2007). The OpenFOAM[®] framework overall structure is represented in Figure 8.

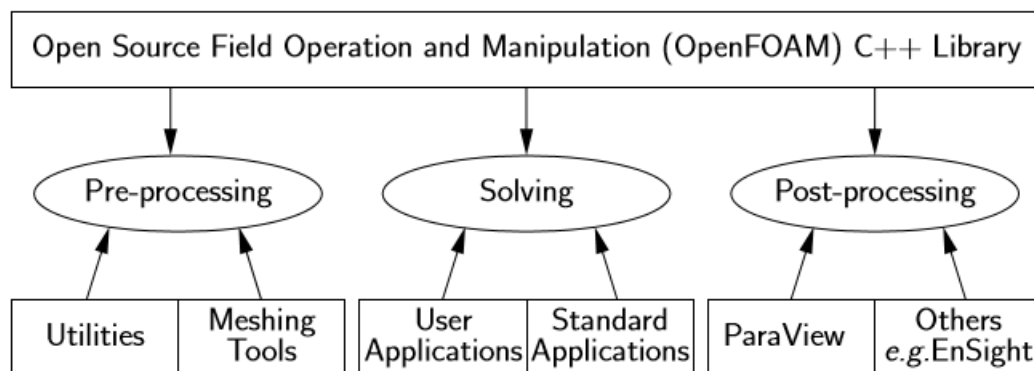


Figure 8 - Overall structure of OpenFOAM[®] (Greenshields, 2015).

1.2 Motivation

The coextrusion process is a very important process in a wide range of industries, in particular in the rope industry, because it allows the products to be manufactured with improved properties combining two or more materials, instead of using only one material with the required properties, which is often more expensive.

As seen in the state of the art, the filament coextrusion is a very complex process, that presents intricate challenges, which need to be overcome in order to design suitable tools, guarantee high quality in the manufactured products and to ensure a stable process. Regarding the design of the die, which is the main objective of this MSc thesis, there are two methodologies to optimize the design: the trial and error method, which presents a large number of limitations and disadvantages, and the numerical simulation of the process. Concerning the numerical simulation of the filament coextrusion, there are only a handful of tools that are capable of simulating the process, that demand complex cases verification to gain confidence on that tools, but they can provide a precious help to solve the inherent process problems and difficulties.

Considering the previous experience using the computational library OpenFOAM® at Minho University and the fact that it has proven his ability to simulate processes of several fields, including the polymer processing field, it would be pertinent test it and apply it to coextrusion problems, namely filament coextrusion.

1.3 Objectives

The main objective of this MSc thesis is to design a multifilament coextrusion die for Lankhorst Euronete capable of coextruding a sheath and core filament and fulfil some specified requirements, with the support of a numerical code based on the OpenFOAM® framework. Prior to the design and to accomplish the main objective, some studies were performed: namely, perform a numerical simulation of a benchmark case study described in the literature, and compare the results obtained numerically for the extrusion and coextrusion (producing sheath and core filaments) of the blends with data collected in experimental studies. These preliminary studies were extremely important to verify if the

results provided by the OpenFOAM® computational library are accurate and thus gain confidence in the capabilities of the tool to simulate the filament coextrusion process.

1.4 Thesis structure

This MSc thesis is divided in five major Sections. The present one contains the state of the art regarding the main subjects covered on the present study, which helps to better understand the filament coextrusion process, the challenges faced in the process and the potential solutions available for its optimization. This section also presents the motivation and the main objectives of the work. Section 2 comprises the studies performed to setup the code verification using a benchmark case study described in the literature. Section 3 covers the experimental assessment performed to the numerical code, which starts with the methodology used to fit the rheological models of the two material blends used to produce the filaments, and is followed by the experimental assessment studies undertaken. Section 4 presents the work performed to design a semi-industrial multifilament coextrusion die, done with the support of the numerical code. The last Section presents the conclusions outlined throughout this MSc project and proposals for future work.

2. VERIFICATION CASE – 2D COEXTRUSION

This section presents a comparison between results available in the literature and computed with the OpenFOAM[®] framework for two incompressible, isothermal immiscible fluids using a volume of fluid (VOF) interface capturing approach. The solver used for this type of computations is called *interFoam* and more information about this solver can be obtained in the work of Herreras and Izarra (Herreras & Izarra, 2013).

The benchmark case study was selected from the paper of Hannachi and Mitsoulis (Hannachi & Mitsoulis, 1993) and describes the development of the interface location in two-dimensional sheet coextrusion. This paper contains studies describing the two-layer coextrusion of polymer solutions in isothermal conditions and the three-layer coextrusion in non-isothermal conditions (Hannachi & Mitsoulis, 1993). Only the first was chosen for the OpenFOAM[®] verification studies.

The case of interest consists on the simulation of a two-dimensional sheet coextrusion of two polymer solutions, namely two polyisobutylene mixtures, considering incompressible and isothermal flow conditions (Hannachi & Mitsoulis, 1993). Figure 9 represents schematically the geometry of the coextrusion die used by the authors of the paper in their numerical simulations of the sheet coextrusion process.

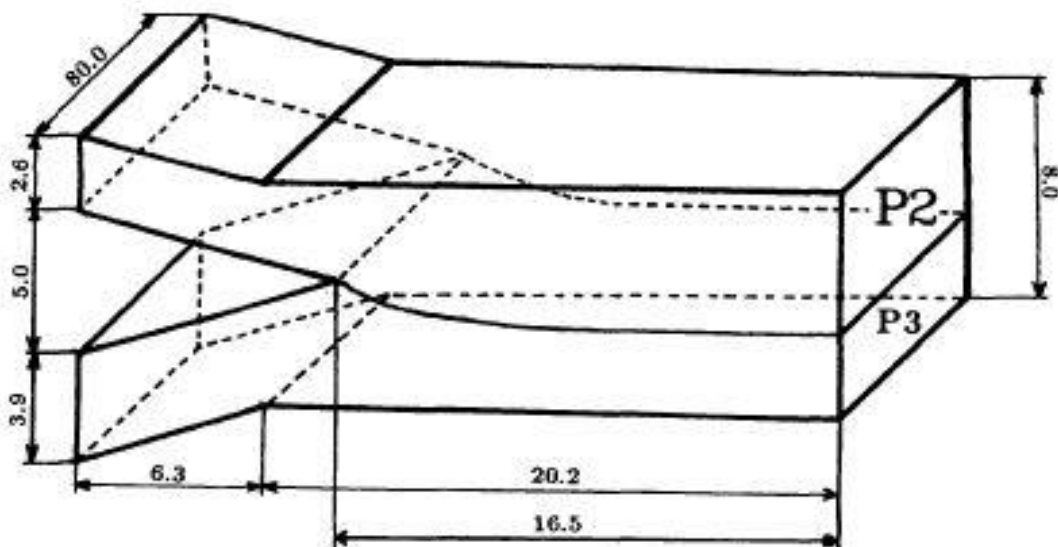


Figure 9 - Schematic representation of the double-layer coextrusion die used by Hannachi and Mitsoulis (Hannachi & Mitsoulis, 1993) (all design measures are given in mm).

In order to gain insight of the mesh generation tools available, and its impact on the results obtained, two alternative tools were used. These results were then compared with the results presented in the paper to study the OpenFOAM® solver accuracy and reliability.

2.1 Geometry generation

Two methodologies were used to obtain the double-layer coextrusion die geometry shown in Figure 9. These geometries will later be used to generate the computational mesh.

The first methodology consisted of using the SolidWorks CAD software to generate the required geometry and save it in a STEP file. Figure 10 shows two views of the geometry created in the software, wherein the dimensions used are equal to the ones presented in Figure 9.

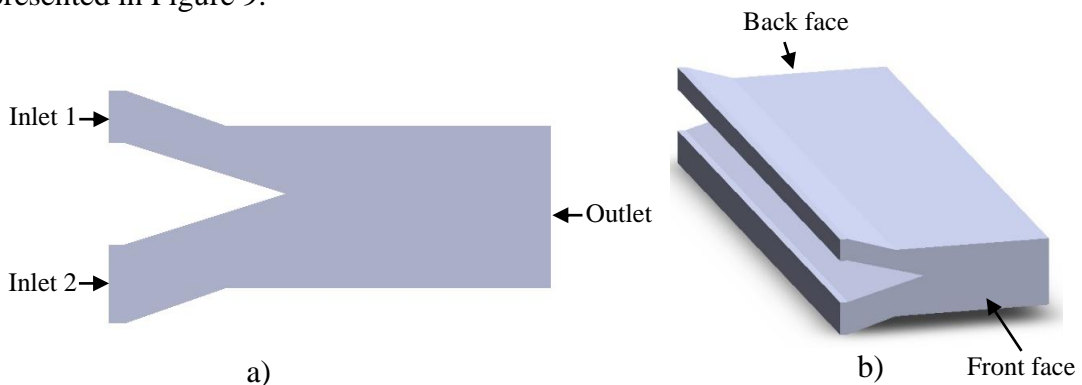


Figure 10 - Geometry obtained with the SolidWorks CAD software: a) frontal view; b) isometric view.

After creating the geometry, it is necessary to define the geometry boundaries, which was done using the opensource CAD software Salome. For this case study, according to Figure 10, the two inlet and the outlet faces are defined with type *patch*, which means that the fluid can enter (inlet) or exit (outlet) the channel through those faces (Herrerias & Izarra, 2013). The front face and the back face are defined with type *empty*, a boundary condition that instructs OpenFOAM® to solve the problem in 2D. The rest of the geometry faces are defined with type *wall* because, where null velocity is imposed to the fluid. Finally, the geometry and the boundaries are saved in a STL file because that's the necessary type of file to generate the mesh in the OpenFOAM® utility called *cfMesh* (Juretić, 2015) (which will be described in the following section).

The second mesh generation methodology consists in the division of the geometry in blocks, wherein each single block is defined by the coordinates of eight vertices points (Greenshields, 2015), as presented in Figure 11. Those coordinates, the boundaries of the geometry (the necessary faces are defined by the coordinates of the four vertices points) and the mesh features (which will be later explained) are then defined in a *blockMeshDict* file which will be used in the generation of the geometry by the OpenFOAM® utility *blockMesh* (Greenshields, 2015). The geometry boundaries are the same as in the first methodology.

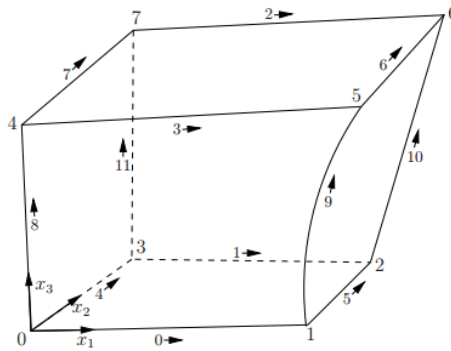


Figure 11 - Example of the eight vertices points that define one single block of the geometry.

2.2 Mesh generation

As mentioned before, the geometry created by the first methodology was used to generate a mesh by the OpenFOAM® mesh utility called *cfMesh*. In order to do that, a maximum cell size in a *meshDict* file must be defined, wherein the dimensions of each individual computational cell of the mesh cannot exceed the specified value. After that, using the *cartesian2Dmesh* command, a 2D mesh with the defined conditions is generated (Juretić, 2015). More information about the generation of meshes using *cfMesh* can be obtained through the *cfMesh* user guide (Juretić, 2015).

In order to perform a mesh refinement study 3 meshes were generated, specifying for the initial one a maximum cell size of 0.5 mm, and dividing this value by 2 in each subsequent mesh. In this way, the coarser mesh (M1) has a maximum cell size of 0.5 mm and contains 922 mesh cells, and the more refined mesh (M4) has a maximum cell size of 0.0625 mm and contains 53062 mesh cells. Figure 12 shows the coarser and the more refined meshes and Table 1 provides some data of the four meshes generated by the *cfMesh* utility, which was obtained with the *checkMesh* utility, included in the OpenFOAM® framework.

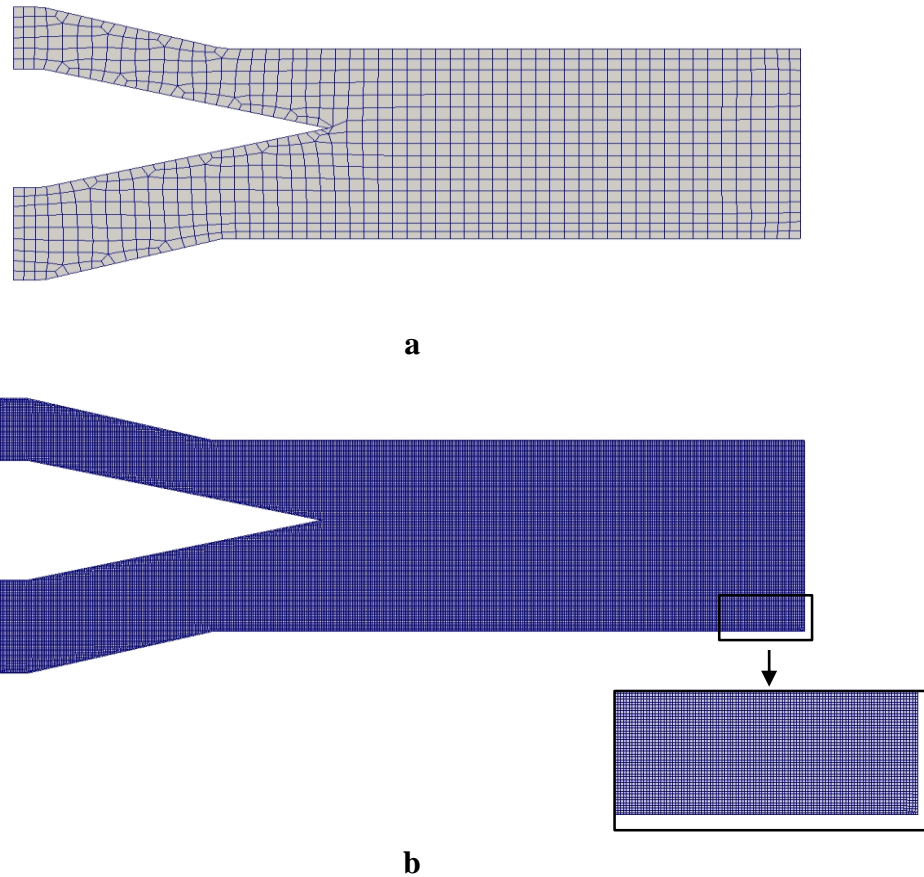


Figure 12 - Meshes created with cfMesh: (a) coarser mesh (M1) and (b) more refined mesh (M4).

Table 1 - Relevant data for all the meshes generated with cfMesh.

	Mesh 1 (M1)	Mesh 2 (M2)	Mesh 3 (M3)	Mesh 4 (M4)
Maximum cell size (mm)	0.5	0.25	0.125	0.0625
Number of points	2054	7308	27692	107732
Number of hexahedra cells	922	3450	13442	53062

Analysing Table 1 is possible to observe that at each refinement performed the number of cells increases circa 4 times, thus quadrupling the number of cells in the mesh.

Another method used in the mesh generation was through the *blockMesh* utility. With this method it is possible to control the number of cells in each block edge. In order to keep the number of cells in each mesh similar to the number of cells of the meshes

created by the *cfMesh* utility, the length and height of each block that composes the geometry was divided by the maximum cell size defined for the correspondent *cfMesh* mesh, thus obtaining the number of cells in the x axis and in the y axis for each block, required by *blockMesh*. In the z axis direction the number of cells is equal to 1, so that the problem is solved in two dimensions. After setting the *blockMeshDict* file, the mesh is created executing the command *blockMesh* (Greenshields, 2015). As it was done with the previous meshes, the quality and some data regarding the mesh can be obtained through the application of the *checkMesh* utility. In Figure 13 it is represented the coarser mesh (M1) and the more refined mesh (M4) and in Table 2 it is represented some data of the four meshes created by the *blockMesh* utility.

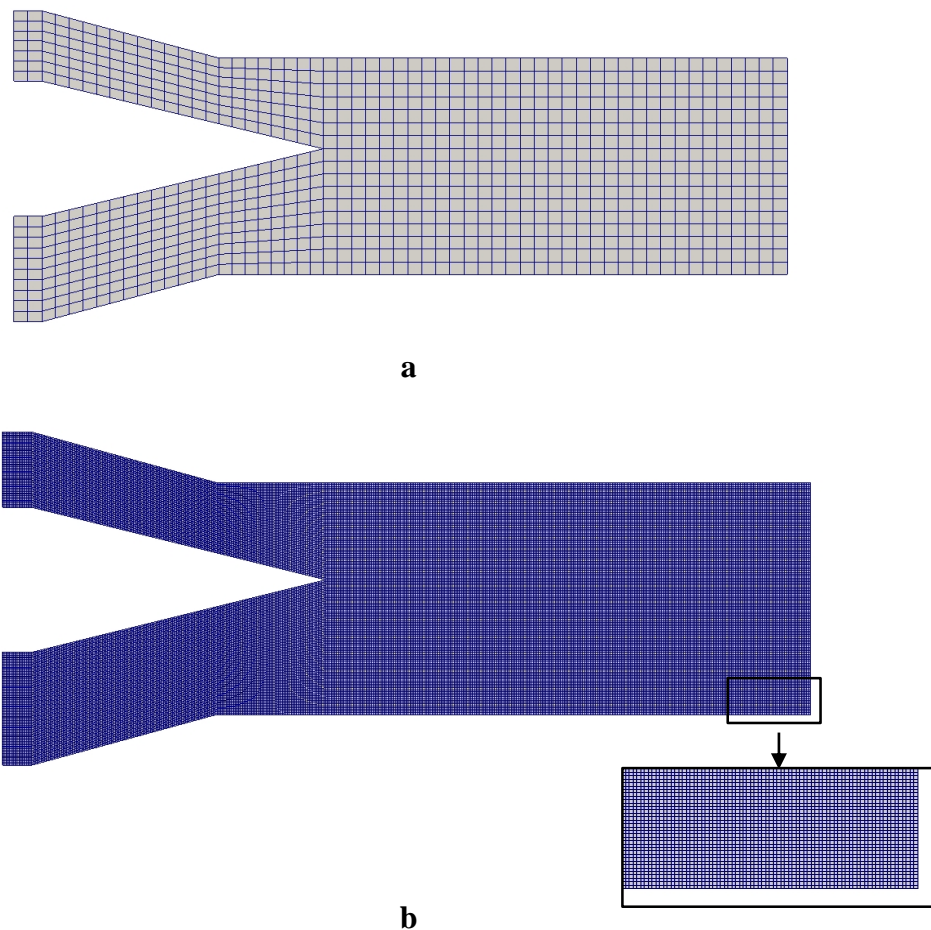


Figure 13 - Meshes created with *blockMesh*: (a) coarser mesh (M1) and (b) more refined mesh (M4).

Table 2 - Relevant data for all the meshes generated with *blockMesh*.

	Mesh 1 (M1)	Mesh 2 (M2)	Mesh 3 (M3)	Mesh 4 (M4)
Number of points	2098	7414	28906	114130
Number of hexahedra cells	952	3520	14080	56320

Like the meshes created using *cfMesh*, analysing Table 2 it is possible to conclude that in each refinement, the number of cells in the mesh increases circa 4 times.

Comparing the data in Table 1 and the data in Table 2, it is possible to see that the meshes created by the *blockMesh* utility have a little bit more cells than the respective meshes created by the *cfMesh* utility, despite the efforts to try to keep this number equal in both cases. However, the number of cells in both cases are of the same order of magnitude for each mesh refinement, which means that similar results are expected to be obtained on those similar meshes.

In terms of quality, all the generated meshes passed the *checkMesh* utility tests, thus they are not expected to affect negatively the results accuracy.

2.3 Properties of the polymeric blends

As stated above, the two materials used in the performed simulations are two polyisobutylene blends (usually denominated as opannols), designated as P2 and P3 (Hannachi & Mitsoulis, 1993). Being polymeric materials these blends present non Newtonian shear thinning behaviour, which means that the viscosity of the material decreases with the increase of the deformation rate. In Figure 14 the rheological curves of the materials are represented and analysing the figure is possible to understand that the P2 presents a much higher viscosity than the P3.

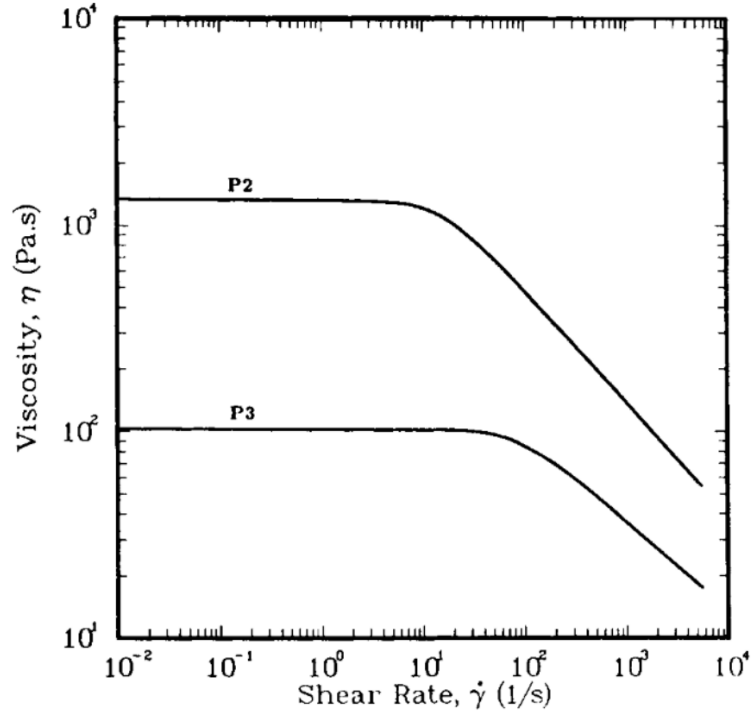


Figure 14 - Rheological curves of the polymer blend P2 and P3 (Hannachi & Mitsoulis, 1993).

The paper authors used the Carreau model to fit the rheological data, whose analytical expression is provided in Equation 1 (Hannachi & Mitsoulis, 1993).

$$\eta = \eta_0 [1 + (\lambda \dot{\gamma})^2]^{\frac{n-1}{2}} \quad (1)$$

where η (Pa.s) is the viscosity, η_0 (Pa.s) is the viscosity at zero shear rate, λ (s) is the material relaxation time, n is the Power Law index and $\dot{\gamma}$ (s^{-1}) is the shear rate.

The value of rheological constants of the model are listed in Table 3, where the dynamic viscosity has to be converted into the kinematic viscosity because OpenFOAM[®] framework uses the kinematic viscosity for the simulation of incompressible flows. This conversion is performed according to Equation 2.

$$v = \frac{\eta}{\rho} \quad (2)$$

where v is the kinematic viscosity, η is the dynamic viscosity and ρ is the density of the material.

Table 3 - Rheological constants and density of the materials for the Carreau model.

	η_0 (Pa.s)	v_0 (m ² /s)	λ (s)	n	ρ (kg/m ³)
P2	1334.9	1.472	0.06520	0.458	907
P3	102.2	0.112	0.01152	0.577	915

Another parameter that has to be defined is the surface tension between the two materials. Since the paper does not define that value, the default value of *interFoam* solver tutorial which is equal to 0.07 kg/s^2 was used.

2.4 Boundary conditions

In terms of boundary conditions, the *interFoam* solver provided by the OpenFOAM[®] framework requires the user to set the velocities of the flow, pressures and material volume fraction in the geometry boundaries.

Regarding the velocities, in the paper three different cases are illustrated with different combinations of inlet mass flow rates. For the runs, these inlet mass flow rates had to be transformed in inlet velocities. With some geometrical measures obtained from Figure 9 and using Equations 3 and 4, it is possible to obtain the required velocities values.

$$Q = \frac{\dot{m}}{\rho} \quad (3)$$

$$v = \frac{Q}{A} \quad (4)$$

where Q is the volumetric flow rate, \dot{m} is the mass flow rate, ρ is the density of the material, v is the flow average velocity and A is the section area of the inlet face.

Table 4 provide the velocities values employed for each case study, which result from the application of the above equations to the mass flow rates given in the comparison paper (Hannachi & Mitsoulis, 1993).

Table 4 - Inlet velocities for the three cases documented in the paper.

Case	\dot{m}_{P3} (g/s)	\dot{m}_{P2} (g/s)	v_{P3} (m/s)	v_{P2} (m/s)
1	5.56	5.44	0.019	0.029
2	2.77	15.28	0.01	0.081
3	22.22	15.28	0.078	0.081

According to the defined inlets, the velocity vector to be specified in each inlet, has only one non null component which is perpendicular to the boundary, which varies with the case and the material, in accordance with the information provided in Table 4. The outlet velocity is defined as *zeroGradient*, which means that the velocity gradient at the outlet is zero. At the walls the velocity is also defined as *fixedValue* but it is set to zero, due to the standard no slip condition of the fluid at the walls.

Regarding the pressure field, since the velocity is fixed in the inlets and the walls, the dynamic pressure is set to *zeroGradient*, so that the gradient normal to the faces is zero, which enables the pressure to float as the velocity is fixed (Herreras & Izarra, 2013). At the outlet, the pressure is defined as being constant and null using the *fixedValue* boundary condition.

2.5 Results and discussion

In order to reduce the computational time of the simulations they were performed admitting that in the initial instant of the flow the die is already filled by the two materials, as illustrated in Figure 15. Then running the simulation with the conditions already stated, the flow tends to reach a steady state, where the velocity profiles are stable and it is possible to observe the interface developed between the two materials.

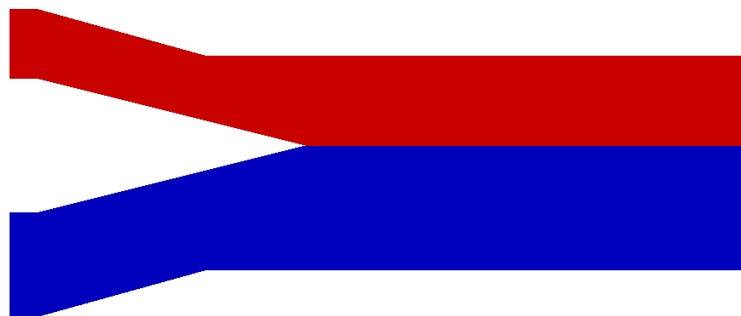


Figure 15 - Initial domain distribution used for all the computational runs: the red field represents the P2 mixture and the blue field represents the P3 mixture.

After performing a test simulation in order to optimize some parameters required by the *interFoam* solver, by checking the results obtained it was observed that after three seconds the flow reached steady stated conditions. For that reason, all the simulations were performed for a maximum time of 3 s and the time step used (including the test simulation) was equal to 1×10^{-6} s. Figure 16 shows the materials distribution when the equilibrium is reached for the three case studies, with the more refined mesh created using *cfMesh* (in the Appendix A are the results to the corresponding meshes created using *blockMesh*).

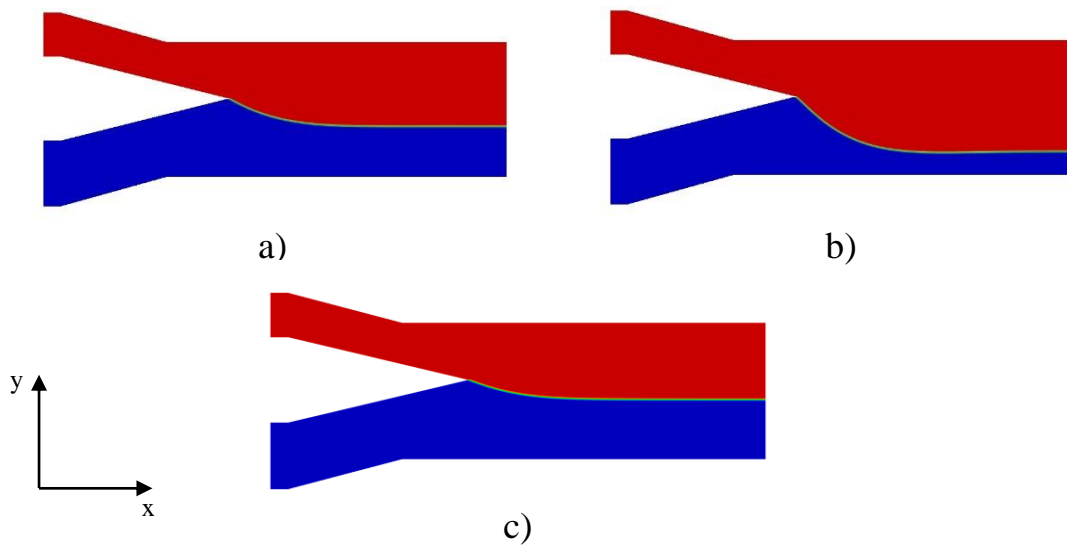


Figure 16 - Steady state flow for 2D coextrusion case study, for the more refined mesh created using *cfMesh* in: a) Case 1; b) Case 2; c) Case 3.

Analysing Figure 16, it can be observed that the less viscous layer (P3 blend) is suppressed by the one with the higher viscosity (P2 blend) in all the tested cases. In Case 2, due to the difference between the velocity imposed to the P2 blend and the velocity imposed to the P3 blend, the suppression of the P3 mixture is more severe than in the other two cases, while in these two cases the suppression of the less viscous layer is more or less the same. This domain distribution is a direct outcome of the viscosity differences, since the flow domains arranged in order to have the same axial pressure gradient. Since P2 has a higher viscosity the layer must be thicker to reduce its velocity and, thus the axial pressure gradient, and the opposite occurs for P3. In this way the axial pressure gradient is balanced in both domains.

Showing the location of the domain containing 50% of the both phases, it is possible to obtain the coordinates of the interface points and thus compare those with the

interface points presented in the comparison paper (Hannachi & Mitsoulis, 1993). Attending to the fact that the paper only possesses a graphical representation of the interface points, it was necessary to obtain the coordinates of these points. Those calculations were made by the open source software *Engauge Digitizer*, where defining the coordinate system, the software generates the coordinates of a set of points belonging to the interface between the two materials. It is important to mention that the figures used from the paper are old and with poor resolution, which may lead to some inaccuracy of the results. Figures 17, 18 and 19 illustrate the graphics comparing the localization of the interface obtained with the OpenFOAM computational library with the results presented in the paper.

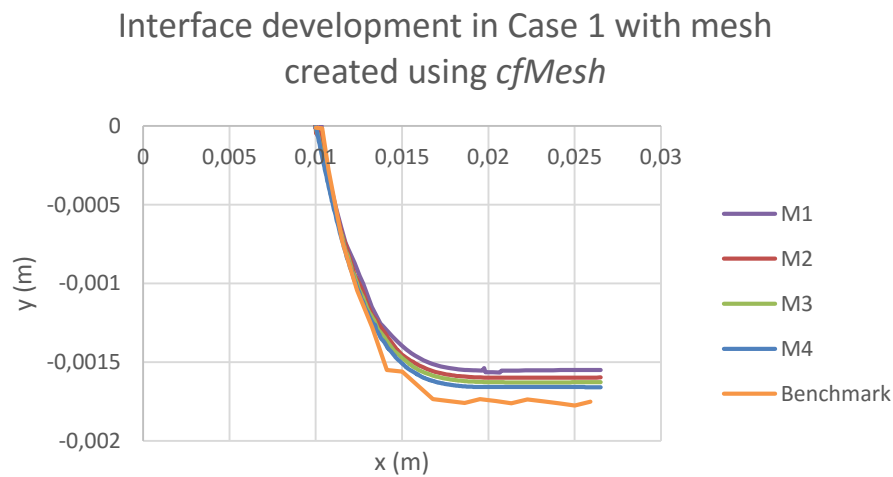


Figure 17 - Interface coordinates for Case 1 (mesh created using *cfMesh*).

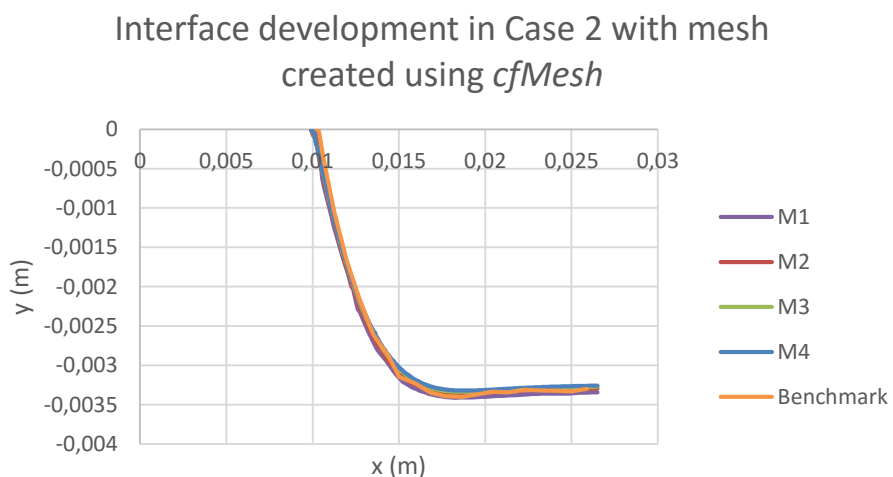


Figure 18 - Interface coordinates for Case 2 (mesh created using *cfMesh*).

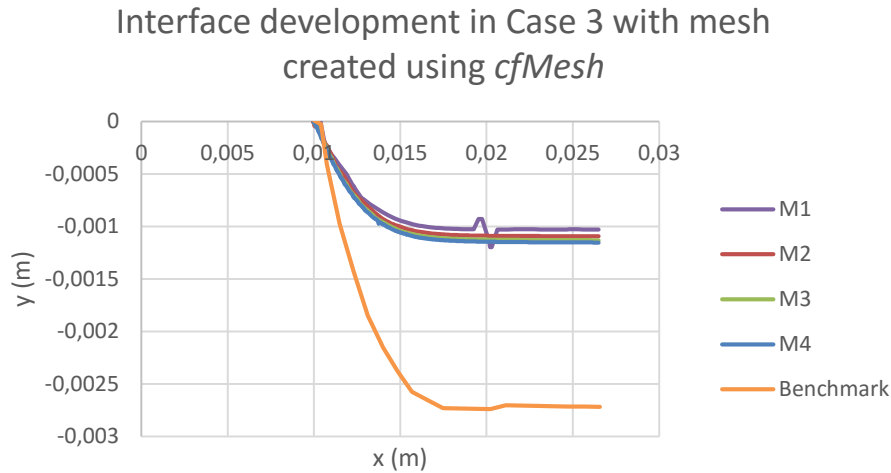


Figure 19 - Interface coordinates for Case 3 (mesh created using *cfMesh*).

From the previous figures it is possible to observe that in Case 1 and in Case 2, as the mesh is refined, the interface position tends to converge to the solution presented in the paper (benchmark). In Case 3, the results obtained are converging to a solution that is not the solution presented in the paper. This may be explained by an error in the mass flow rates provided in the paper.

Regarding the results obtained with the meshes created by the *blockMesh* utility, they are more or less the same than those obtained for the meshes created with *cfMesh*, not having significant differences between them, as can be seen comparing Figure 17 with Figure 20 (in the Appendix B are the graphics for the other cases).

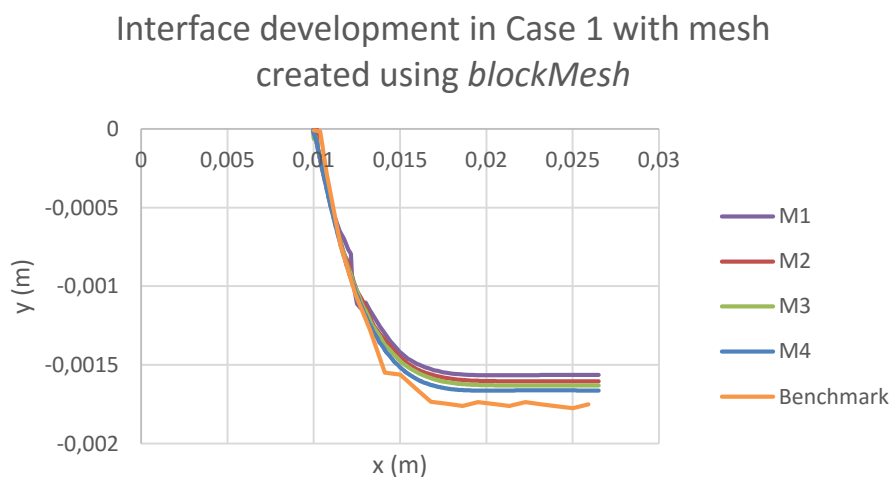


Figure 20 - Interface coordinates for Case 1 (mesh created using *blockMesh*).

In order to ascertain the error between the solution obtained with the OpenFOAM[®] computational library and the solution from the paper, in the cases studied, the L_1 error was determined. This value measures the average error between an infinitely refined mesh and the real solution.

The first step in this methodology is to apply the Richardson extrapolation technique for a set of points of three different meshes. Through Equation 5 the apparent order is computed.

$$p = \frac{|\ln|(T_3 - T_2)/(T_2 - T_1)||}{\ln(r)} \quad (5)$$

where r is the refinement factor (equals to 2) and T_i is the value of the property in mesh i .

Then, the value obtained for the apparent order of the method can be used to compute the extrapolated value of the property in study for an infinitely refined mesh, as defined by Equation 6.

$$T_{ext} = \frac{(r^p T_2 - T_3)}{(r^p - 1)} \quad (6)$$

The second part of the methodology consists in finding the L_1 error using Equation 7, which requires the values calculated for an infinitely refined mesh and the values obtained from the paper (admitting those values as the real values), for a set of 100 points.

$$L_1 = \frac{\sum |T_{real} - T_{ext}|}{n_{points}} \quad (7)$$

Table 5 contains the values of the L_1 error for the two types of meshes used in the three case studies.

Table 5 - L_1 errors for the meshes created using *cfMesh* and *blockMesh* for the three case studies.

	Case 1		Case 2		Case 3	
	<i>cfMesh</i>	<i>blockMesh</i>	<i>cfMesh</i>	<i>blockMesh</i>	<i>cfMesh</i>	<i>blockMesh</i>
L_1 (mm)	0.082	0.092	0.41	0.18	1.34	1.35

Analysing the errors value for the three cases, it can be concluded that Case 3 has a higher error than the other two cases, which was expected due to the differences between the numerical solutions and the paper solutions. In addition, the numerical solutions obtained for Case 1 are the ones that are more close to the paper solutions. Regarding the differences between the meshes created using *cfMesh* and *blockMesh*, we can state that the difference between them is very small, so it can be concluded that both meshing methods produce very similar results.

In order to compare the flowlines and confirm the interface results presented above, the streamlines of the flow field were assessed. Figures 21 illustrates the results achieved by the authors of the paper (Hannachi & Mitsoulis, 1993) and Figure 22 presents the results obtained in the more refined meshes generated by *cfMesh* for the three case studies (in Appendix C are the results for the corresponding meshes generated by *blockMesh*).

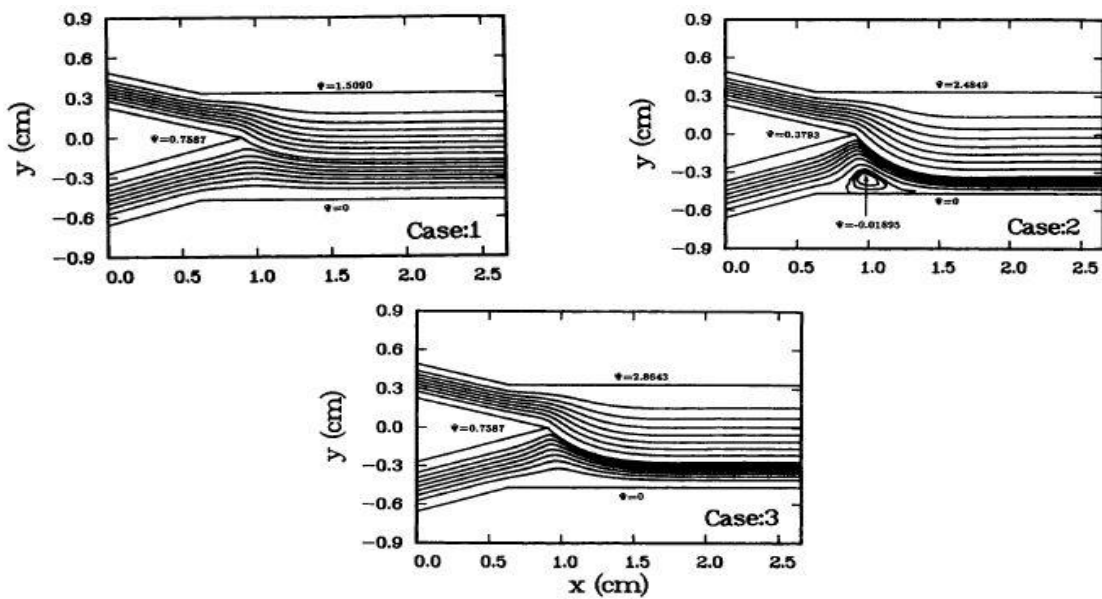


Figure 21 - Streamlines obtained by Hannachi and Mitsoulis (Hannachi & Mitsoulis, 1993).

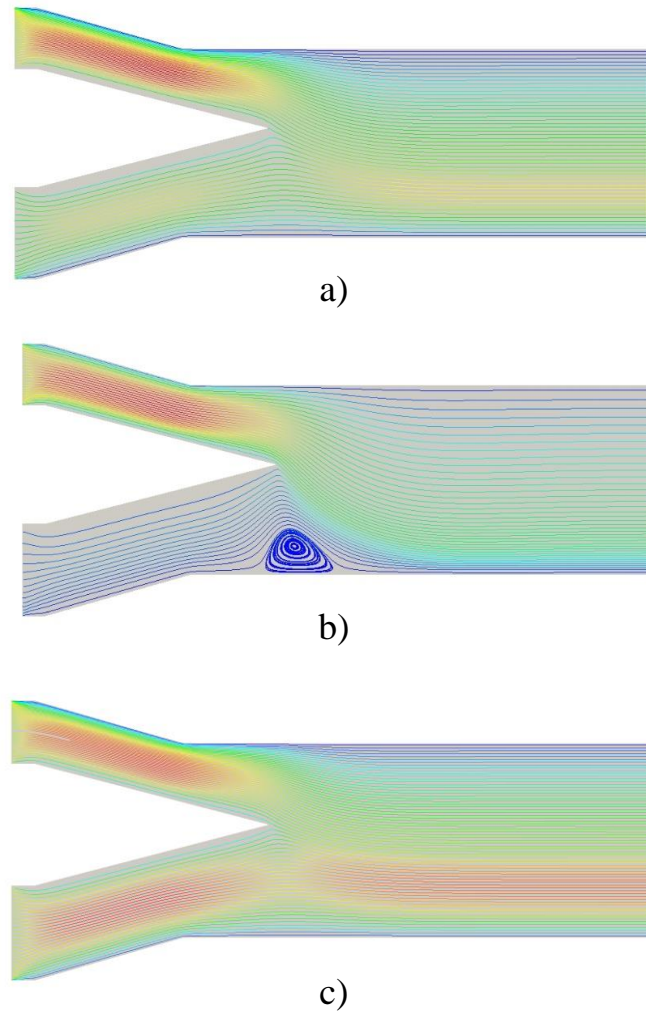


Figure 22 - Representation of the streamlines (coloured according with the velocity intensity) for the more refined mesh created using *cfMesh* in: a) Case 1; b) Case 2; c) Case 3.

Analysing Figure 22, it is possible to observe that in the two inlets, due to the mass flow rates imposed, the velocity of the P2 blend is higher than the one of the P3 blend in Cases 1 and 2, while in Case 3 the velocities of the blends are quite similar. Afterwards, the two materials join each other in the die land, and it can be observed that only in Case 3, where the suppression of the P3 blend is less severe, the parabolic velocity profile in this layer can fully develop, since there is a higher velocity near the centre than the boundaries of the layer (if the boundary is a wall, usually the velocity is considered null). In the other two cases, due to the suppression caused by the P2 blend, the full development of the velocity profile of the P3 layer is never completed, which means that at the interface between the two materials the velocity is higher. Regarding the velocity profile of the P2 layer, in all the cases the last one does not develop completely, which as stated above, leads to the development of the higher velocity at the interface.

Comparing the streamlines in Figure 22 with the streamlines obtained by the authors of the paper (see Figure 21), it can be concluded that in Case 1 and 2 the results presented in Figure 22 are very similar to the results presented in the paper, shown in Figure 21, since the suppression of the less viscous layer is well predicted, the streamlines are very steady with very little instabilities and in Case 2 the presence of a recirculation region is obtained. As expected in Case 3 the streamlines are slightly different than the streamlines presented in the paper, possible due to the reasons stated above.

3. OPENFOAM[®] EXPERIMENTAL ASSESSMENT

In this Section the OpenFOAM[®] software is used to simulate the extrusion and coextrusion of the two blends, in order to produce one material and two material filaments, in this last case to obtain sheath and core filaments.

The conditions used in the simulations followed the ones employed António Abreu and described in his MSc thesis (Abreu, To be published), in order to assess experimentally the numerical results and gain more confidence in the simulation capabilities in complex processes of the OpenFOAM[®] framework.

3.1 Rheological models and properties of the blends

In order to perform the simulation of the processes mentioned before, it is necessary to obtain the rheological data and other physical properties of the blends.

To obtain the blends flow curves, they were characterized using parallel plate, for low shear rates, and capillary rheometry, for high shear rates. Given the experimental procedures and results described in António Abreu MSc thesis (Abreu, To be published), the following step was to fit the experimental measurements to an adequate constitutive model.

The time-temperature superposition principle was applied to extend the characterization window of the material, making possible to calculate the viscosity at any temperature from the viscosity at a reference temperature (Carneiro & Nóbrega, 2012).

The models used to fit all the rheological data points were constituted by the Carreau model, and also for the data points at higher shear rates by the Power Law model (which will be used to compute the pressure drop in a missing zone of the geometry used in Section 3.3), in order to account the effect of the shear rate on viscosity, and the Arrhenius law to consider the temperature effect. Equation 8 states the Arrhenius law, and Equations 9 and 10 define the Carreau/Arrhenius and Power Law/Arrhenius model, respectively.

$$a_T = e^{\frac{E}{R} \left(\frac{1}{T} - \frac{1}{T_{Ref}} \right)} \quad (8)$$

where E (J/mol) is the material activation energy, R (J/K.mol) is the gas constant, T (K) is the temperature and T_{Ref} (K) is the reference temperature.

$$\eta = \eta_0 a_T [1 + (\lambda a_T \dot{\gamma})^2]^{\frac{n-1}{2}} \quad (9)$$

where η (Pa.s) is the viscosity, η_0 (Pa.s) is the viscosity at zero shear rate, λ (s) is the material relaxation time, n is the Power Law index, a_T is the shift factor and $\dot{\gamma}$ (s⁻¹) is the shear rate.

$$\eta = k (a_T \dot{\gamma})^{n-1} \quad (10)$$

where k (Pa.sⁿ) is the consistency index.

Using the *Excel* software, the equations mentioned above were applied to the rheological data points for each blend and for three temperatures (210°C, 230°C which is the reference temperature and 260°C) as described in Ant3nio Abreu MSc thesis (Abreu, To be published). The procedure used to obtain the models rheological constants consist in optimizing the rheological constants using the *Excel* tool *Solver* to minimize the differences between the viscosity values obtained experimentally and by the fitting models. To do so, the *Solver* algorithm was set to use evolutionary methods, thus providing the best possible results. Table 6 shows the rheological constants for the Carreau model of the blends and Table 7 the constants for the Power Law model.

Table 6 - Rheological constants for the Carreau model.

	η_0 (Pa.s)	λ (s)	n	E (J/mol)
Blend A	14684.43	0.498	0.23	20690.09
Blend B	9239.17	0.73	0.309	38734.86

Table 7 - Rheological constants for the Power Law model.

	k (Pa.s ⁿ)	n	E (J/mol)
Blend A	24998.16	0.23	20690.09
Blend B	11416.38	0.31	38734.86

The values obtained were used to plot the flow curves for the two blends. In Figures 23 and 24 are illustrated the flow curves using the Carreau/Arrhenius model for Blend A and Blend B, respectively.

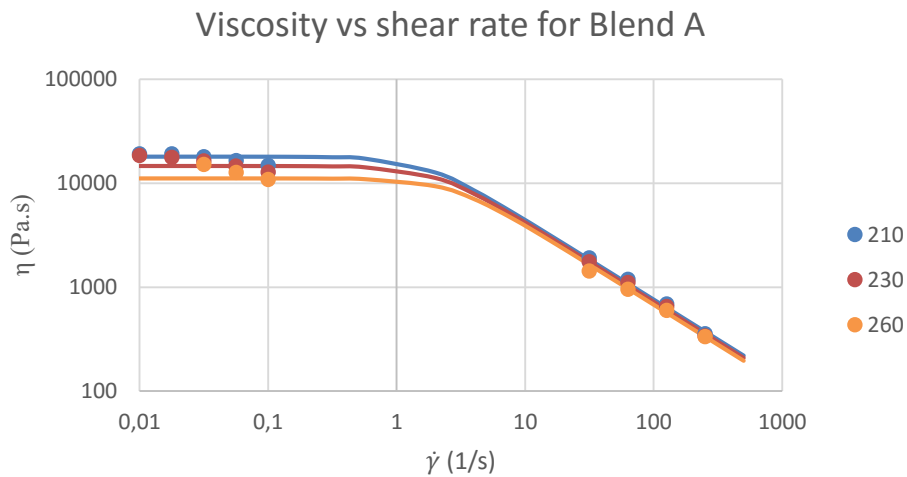


Figure 23 - Viscosity curves using the Carreau model for Blend A.

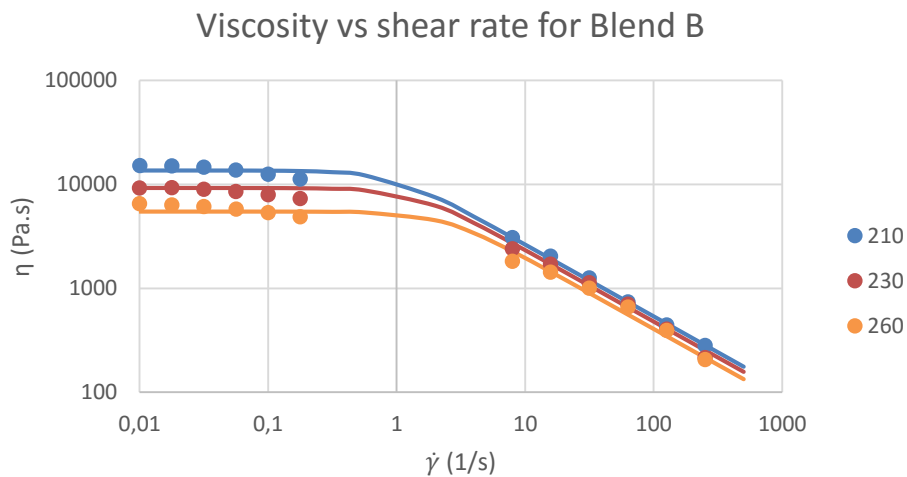


Figure 24 - Viscosity curves using the Carreau model for Blend B.

Plotting the viscosity curves of the two blends at the reference temperature (230°C), as shown in Figure 25, it is possible to confirm that the two blends have a slight viscosity mismatch between them, and that Blend A is more viscous than Blend B. However, the viscosity mismatch between the two blends is relatively small and it should

not cause significant instabilities in the coextrusion process, especially if Blend A is the inner material of the filament.

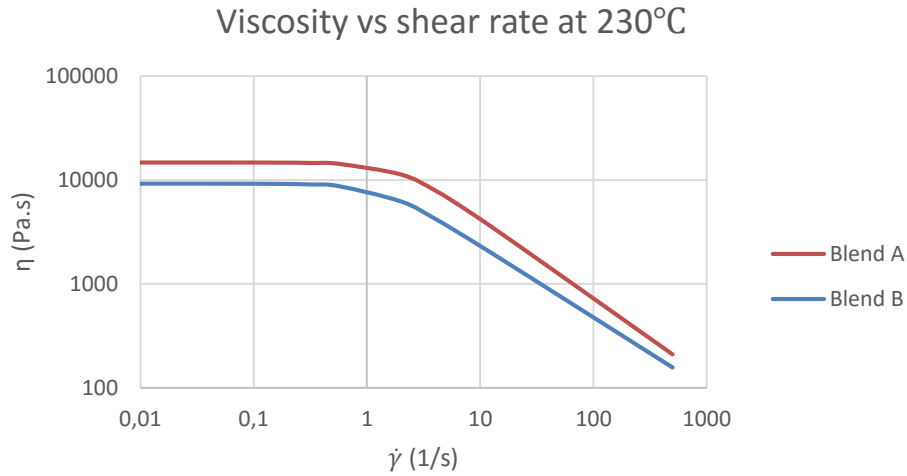


Figure 25 - Viscosity curves using the Carreau model for Blend A and B at 230 °C.

Besides rheological data, the OpenFOAM[®] solvers also need some properties of the blends like density (ρ), thermal conductivity (k) and specific heat capacity (c) to run the case. Because the materials in this study are blends of two polymers, the law of mixtures presented in Equation 11 can be applied in order to determine the required properties.

$$P_b = xP_1 + (1 - x)P_2 \quad (11)$$

where P_b is the property in study for the blend, P_1 and P_2 are the specific properties for material 1 and material 2 and x is the relative content of material 1.

Table 8 shows the percentages of each polymer that constitutes each blend and all the properties that have been calculated through Equation 11, using typical values of the properties for each polymer in study.

Table 8 - Relative content of blend materials and the properties calculated using the law of mixtures.

	% P_1	% P_2	ρ (kg/m^3)	k ($W/K.m$)	c ($J/kg.K$)
Blend A	70	30	937.9	0.375	1980
Blend B	30	70	919.1	0.275	1820

For the numerical runs, namely the extrusion case in Section 3.2, the solver needs some additional materials constants, that depend on the previous ones presented, namely the thermal diffusivity coefficient (DT) calculated using the values in Table 8 and alpha (α) which is calculated using the activation energy of the materials presented in Table 6 and the perfect gas constant (R). Equations 12 and 13 defines, respectively, the thermal diffusivity coefficient and the alpha value.

$$DT = \frac{k}{\rho c} \quad (12)$$

$$\alpha = \frac{E}{R} \quad (13)$$

Table 9 presents the values computed for these constants for each blend used.

Table 9 - Values of the thermal diffusivity coefficient and the alpha for the Blend A and B.

	DT (m^2/s)	α (K)
Blend A	$2.019 * 10^{-7}$	2489.782
Blend B	$1.64 * 10^{-7}$	4661.235

The viscosity model, the respective rheological constants of the model for the two blends, and the properties computed before were used to define the blends physical behaviour in the performed simulations.

3.2 Extrusion of Monofilaments

The extrusion of each blend was made in order to obtain one material filaments, later the same filaments were subject to mechanical tests to quantify their mechanical properties, as described in Ant3nio Abreu MSc thesis (Abreu, To be published). For assessment purposes, the extrusion process was then simulated using a single phase solver, developed by Ananth Rajkumar et al. and it is described and explained in the respective paper (Rajkumar et al., Accepted for publishing).

3.2.1 Geometry and operating conditions

The extrusion die used in the extrusion process was an existent extrusion die in the Polymer Engineering Department. The 3D geometry of the die is partially represented in Figure 26.

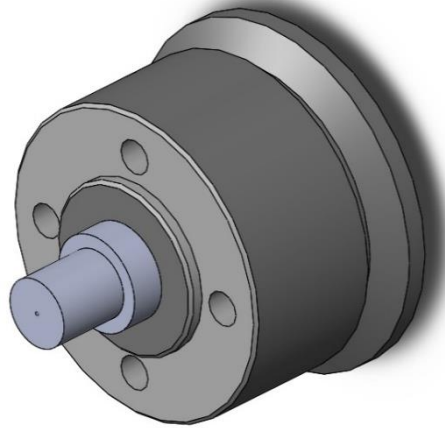


Figure 26 - 3D geometry of the extrusion die used in the extrusion process.

Using the 3D model represented above in the CAD software SolidWorks it was possible to obtain the flow channel geometry, where the polymer flows, which is necessary to construct the modelling domain and the respective mesh. For that, the tool used was the *Cavity* tool provided by the SolidWorks software, which is able to create a negative of the channel in a previously created block, as illustrated in Figure 27.

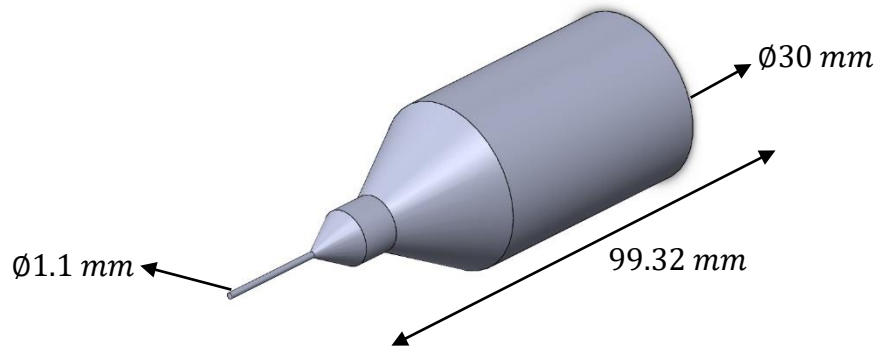


Figure 27 - Geometry of the extrusion die flow channel.

The channel has a circular geometry, where the inlet diameter is equal to 30 mm, the outlet diameter is 1.1 mm and the length of the channel is 99.32 mm. Analysing Figure 27, it is possible to observe that the channel has three constant section regions, intercalated by two convergent regions.

Regarding to the operating conditions, the mass flow rate used in the experimental procedure was 94.32 g/h and the temperature of the heating bands was set to 230 °C , a temperature higher enough to allow the melting and flow of the two types of polymers that compose the employed blends.

3.2.2 Mesh and boundary conditions

Observing Figure 27, it is possible to understand that the channel is axisymmetrical. This fact can be used to simplify the computational mesh employed and thus reduce the simulation time. Thus, applying the right patches to the mesh (Greenshields, 2015), it is possible to simulate only one small slice of the geometry and still get results as if the whole geometry had been simulated.

The mesh required for running the simulation was build using the *blockMesh* OpenFOAM® utility. A slice of 5° was used to represent the full flow channel. In Figure 28 are presented two views of a slice of the channel used in the simulations and the boundary conditions defined.

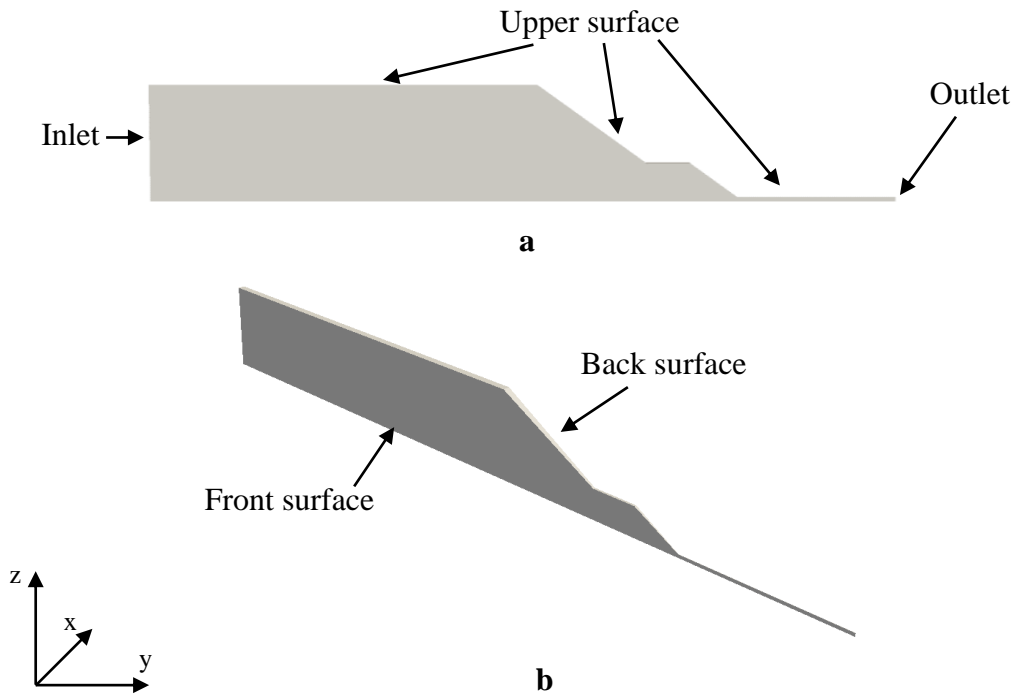


Figure 28 - Slice of the flow channel used in the simulations: (a) frontal view and (b) isometric view.

Finally, to create the mesh, the utility needs the number of cells that each block should contain in each of the three directions of the Cartesian coordinate system, and the patches of every outside face in each block.

Regarding the number of cells, for the y axis the number was calculated considering the length of each block in order to obtain an equal ratio between the number of cells and the length, in the z axis the number of cells was kept constant in all the blocks and in the x axis all the blocks have only one cell, as required by an axisymmetric model.

Concerning the boundary patches presented in Figure 28, the upper surface was defined as *wall*, the inlet (left surface with the higher diameter) and the outlet (right surface with the lower diameter) was defined as *patch*. The front and the back surface were defined as *wedge* and a symmetric axis was defined in order to define an axisymmetric geometry (Greenshields, 2015).

For this case study the *blockMesh* utility was used to generate de mesh. Three meshes were created being the first mesh (M1) the coarsest mesh and the third mesh (M3) is the refined, both illustrated in Figure 29, comprising 1362, 5448 and 21792 computational cells. The refinement performed was accomplish by doubling the number of cells in each direction (except in the x axis direction), thus quadrupling the number of cells in the computational mesh, as it can be concluded comparing the computational cell values mentioned above.

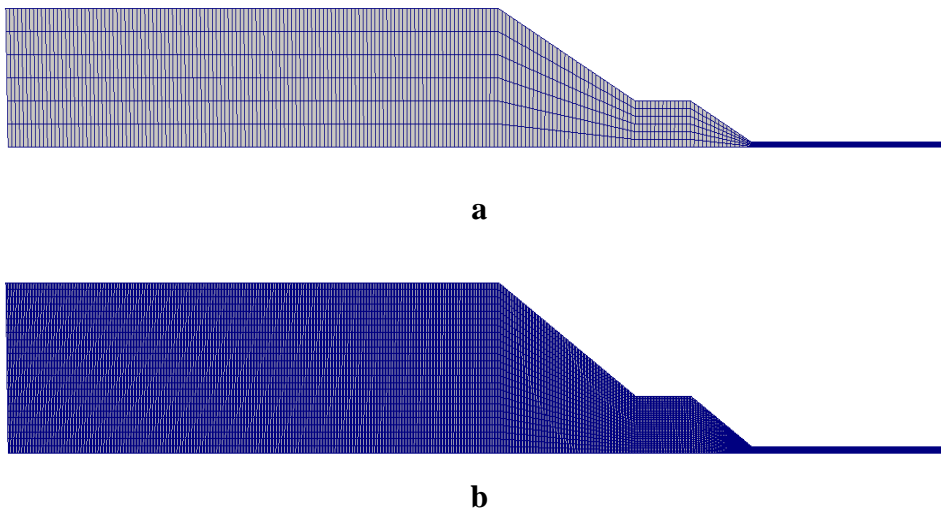


Figure 29 - Meshes used in the simulations of the extrusion of the filaments: (a) coarser mesh (M1) and (b) more refined mesh (M3).

Regarding to the boundary conditions, the solver requires to specify the velocity, the pressure and the temperature at all the different boundaries. In terms of velocity, considering the mass flow rate used in the experimental procedure, the diameter of the inlet and using Equations 3 and 4, it is possible to calculate the inlet velocities for both blend. Table 10 lists the inlet velocities obtained.

Table 10 - Inlet velocities of the Blend A and B in the extrusion process.

	Blend A	Blend B
Mass flow rate (g/h)	94.32	94.32
Density (kg/m³)	937.9	919.1
Inlet velocity (m/s)	3.95×10^{-5}	4.03×10^{-5}

Thus, since this is again a steady state case study, the velocity at the inlet is set to *fixedValue* with the corresponding value presented in Table 10. The outlet velocity is defined as fully developed (*zeroGradient*), which means that the velocity gradient at the

outlet is zero and at the walls the velocity is also defined as *fixedValue* but it is set to zero, because it was admitted that there is no slip between the fluid and the die wall.

In terms of pressure, since the velocity is fixed in the inlets and the walls, the pressure in this boundaries is set to *zeroGradient* and the outlet pressure is set as *fixedValue* and equal to zero.

The temperature was imposed in the inlet and in the boundary defined as *wall* (top surface of the geometry) in order to simulate the effect of heat provided by the heating bands in the flow and is set to 503.15 K (230 °C), which is the temperature used in the extrusion process. At the outlet the temperature distribution is assumed to be fully developed, thus this boundary is set to *zeroGradient*.

In all the boundary conditions mentioned before, the front and the back surface of geometry were defined as *wedge* and the symmetric axis, a face with null area that corresponds to a single edge, was defined as *empty*.

3.2.3 Results and discussion

In order to define the simulation time, it was performed a test simulation wherein the end time was defined as 2 seconds and was used a time step equal to 1×10^{-4} s seconds. The residuals of the variables of this simulation were plotted to found out whether the time simulated is sufficient for the residuals (error in the solution obtained) stabilize at low values, thus ensuring an accurate solution. Figure 30 it shows the evolution of the simulation residuals for all the variables in study during the time simulated (each iteration corresponds to 1×10^{-4} s).

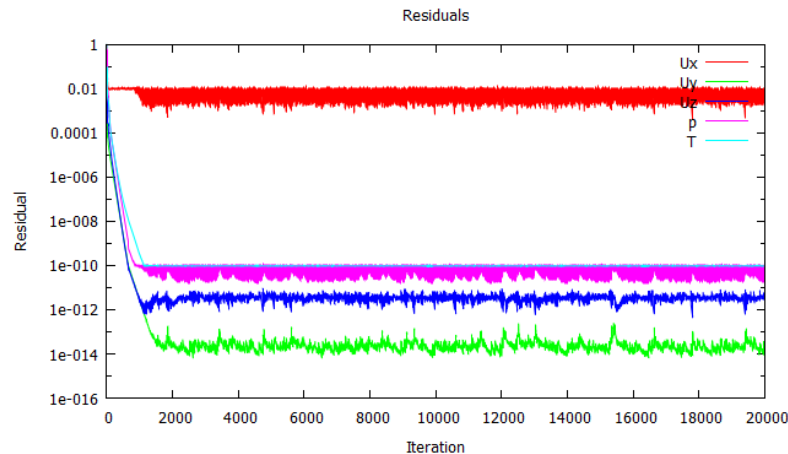


Figure 30 - Evolution of the residuals along the simulated time in the extrusion process.

Analysing the previous figure, it is possible to observe that after 0.2 s (2000 iterations) the residuals tend to stabilize at low values, except the velocity along the x axis which stabilizes at higher residual values because the geometry used is a wedge geometry.

To find out if the extrusion process reaches stable conditions, it was checked the evolution of the velocity, pressure and temperatures values along the simulated time in three different points of the domain, wherein Point 1 is near the inlet, Point 2 is at the middle of the channel and Point 3 is at the outlet, as presented in Table 11 (the temperature does not fluctuate in any instant of time, so its values were not presented in Table 11).

Table 11 - Evolution of the velocity and pressure values in three different points along the simulated time.

	Point 1		Point 2		Point 3	
Time (s)	U (m/s)	P (MPa)	U (m/s)	P (MPa)	U (m/s)	P (MPa)
0	0	0	0	0	0	0
0.5	7.6×10^{-5}	9.561	0.0002	9.559	0.04	0
1	7.6×10^{-5}	9.561	0.0002	9.559	0.04	0
1.5	7.6×10^{-5}	9.561	0.0002	9.559	0.04	0
2	7.6×10^{-5}	9.561	0.0002	9.559	0.04	0

Analysing Table 11, it is possible to conclude that in all points tested the velocity and the pressure values stabilize at more or less 0.5 s.

Considering all that, the two seconds simulated is more than enough for the simulation to achieve stable conditions and to ensure a solution with a high degree of accuracy. Therefore, it was used an end time of 2 s and a time step of 1×10^{-4} s in all the simulations performed.

The results obtained from the simulation for the pressure, the velocity and the temperature fields developed along the die for the two blends in study are presented in Figures 31, 32 and 33 using the mesh M3.

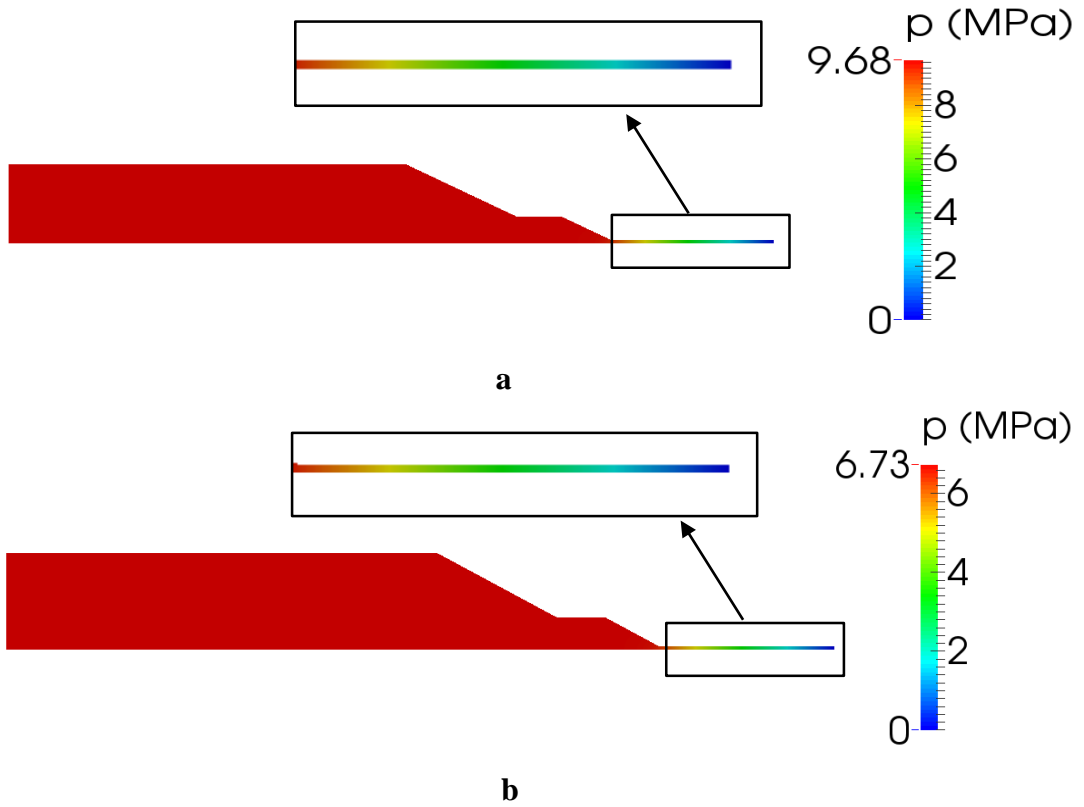


Figure 31 - Pressure field predicted by the code along the die during the extrusion process of the Blend A (a) and Blend B (b).

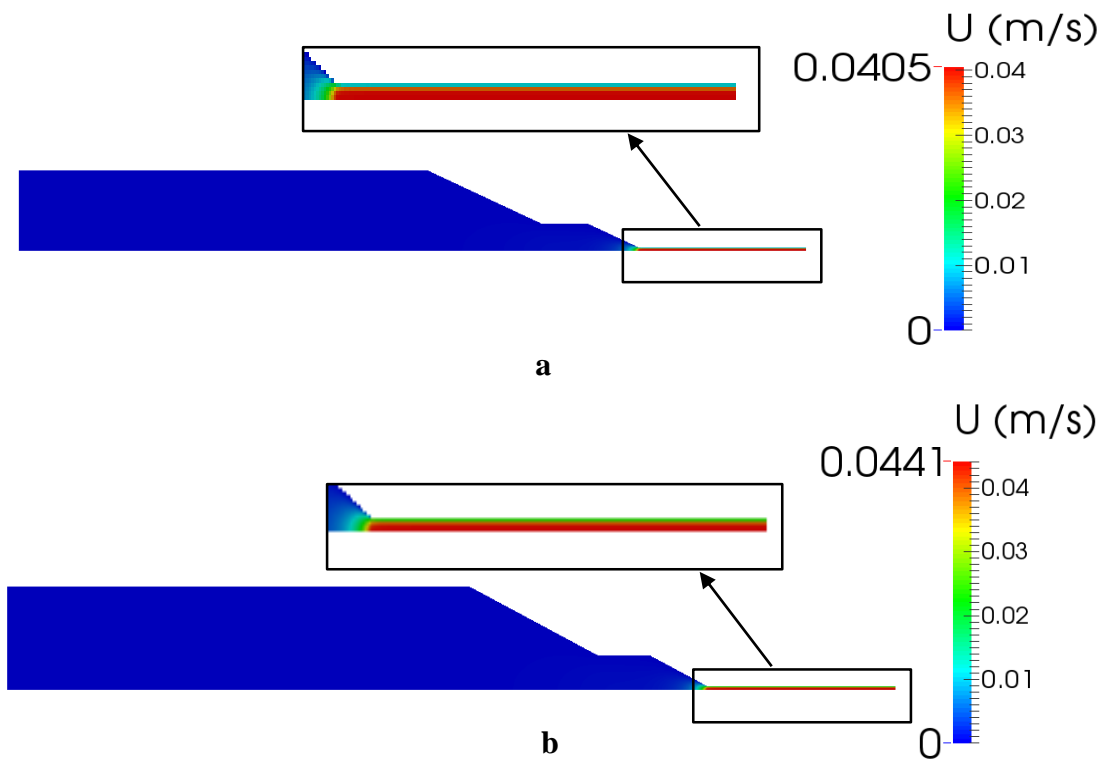


Figure 32 - Velocity field predicted by the code along the die during the extrusion process of the Blend A (a) and Blend B (b).

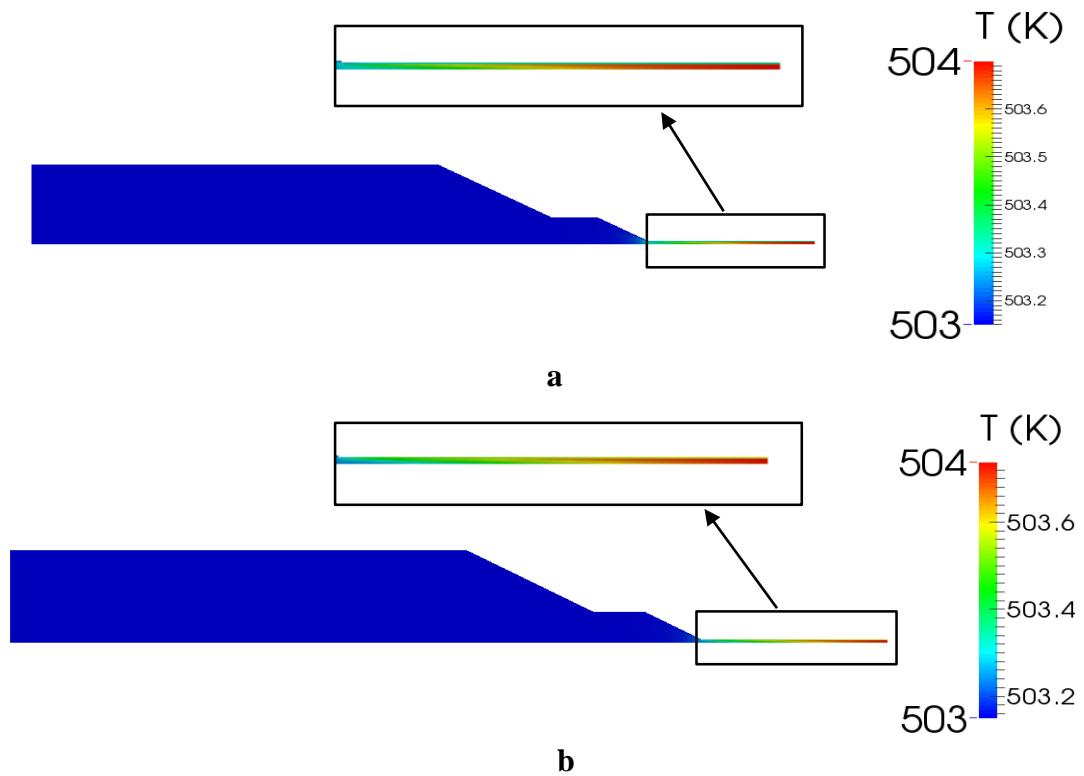


Figure 33 - Temperature field predicted by the code along the die during the extrusion process of the Blend A (a) and Blend B (b).

Regarding the pressure and velocity fields it is possible to observe that only in the parallel zone there is a significant change in the data values, due to the decrease in the die cross section area which causes an acceleration of the material, increasing the velocity and the pressure drop. Through the figures it can be pointed out that the total pressure drop in the die channel is circa 9.6 MPa for Blend A and 6.7 MPa for Blend B. The outlet velocity has a value more or less equal for the two blends which is 0.0405 m/s (2.43 m/min) for Blend A and 0.0441 m/s (2.65 m/min) for Blend B. In terms of temperature distribution, analysing Figure 33, it is possible to conclude that there is no significant viscous dissipation during the flow, since the temperature remains almost constant along the domain in all cases.

Using the pressure field results of each material obtained for each one of the three meshes, it's possible to obtain the value of the pressure in the exact spot where the pressure sensor is located. The pressure values obtained numerically on the three meshes were used to obtain the pressure value for an infinitely refined mesh, by following the Richardson extrapolation technique. In addition, the experimentally measured pressure values were compared with the numerical values doing the relative error between them. The results for the processing cases studied are presented on Table 12.

Table 12 - Pressures obtained using the simulations and experimentally in the same spot and the error between them.

	P_{M1} (MPa)	P_{M2} (MPa)	P_{M3} (MPa)	P_{∞} (MPa)	P_{real} (MPa)	Error (%)
Blend A	9.56	9.66	9.67	9.68	10.91	11.31
Blend B	6.67	6.72	6.73	6.73	9.24	27.2

The difference between the pressure computed on the infinitely refined mesh (P_{∞}) and the one computed on the more refined mesh (P_{M3}) is very small. In particular, for Blend B that difference is imperceptible due to the number of decimal places used for the values shown in Table 12. Thus, it can be concluded that the more refined mesh produces good results being very close to the ideal computational solution.

The pressure measured experimentally (P_{real}) presented in Table 12 for each blend is the average value computed using all the pressure data obtained. Beside the average values, it was also computed the standard deviation of each set values, obtaining a standard deviation of 0.38 MPa (4.1%) for Blend A and 0.12 MPa (1.8%) for Blend B. Comparing the computational solution for each blend with the respective experimental pressure, the relative error between the two values computed was 11.31% for Blend A and 27.2% for Blend B. Those two values are off the range of the experimental error obtained, which could be related to any mistake made in the experimental measurements, namely, in the pressure sensor calibration.

3.3 Coextrusion of the blends

In this Section it will be explained the simulations performed in order to describe the coextrusion process of the blends, whose main objective is to produce multifunctional filaments where Blend A is used to form the sheath and Blend B composes the core of the filaments. The simulations were performed using the multiphase solver *interFoam* which provides data about the pressure field, velocity field and interface between the materials and which was later compared with experimental results. All the experimental procedure and the experimental results achieved could be consulted in detail in António Abreu MSc (Abreu, To be published).

3.3.1 Geometry and operation conditions

The coextrusion die used in the experimental procedure was the same that Martins and his co-workers (Martins et al., 2014) employed in their experiments. The 3D model of that coextrusion die inner modules is presented in Figure 34.

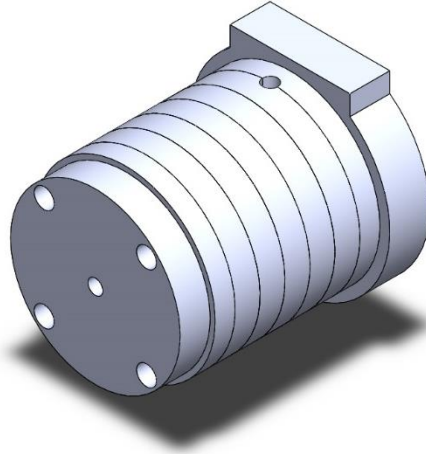


Figure 34 - 3D model of the coextrusion die modules used to produce the multifunctional filaments.

The process that has been used to obtain the geometry of the flow channels contained in the die was the same process used to obtain the channels in the extrusion die described in Section 3.2.1. In Figure 35 it is possible to observe the flow channel of the original coextrusion die.

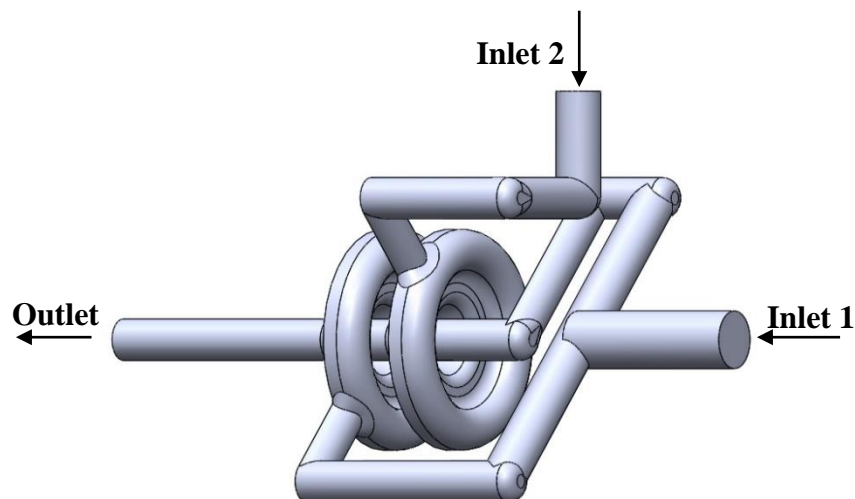


Figure 35 - Geometry of the flow channels of the original coextrusion die.

The original setup of the coextrusion die allows the production of filaments with three layers, where the material that enters inlet 1 is used to form the core and the sheath

of the filament and the material that enters inlet 2 forms the intermediate layer, as can be seen from Figure 35. Taking advantage of the modular design of this die, some changes in the modules configuration were made in order to obtain a die setup capable to produce filaments with only two layers (sheath and core), without changing the diameter of the manufactured filaments which is 3 mm and keeping the two inlets and the outlet as presented in Figure 35. Two configurations of the modules that allow to obtain the desired filaments were considered. Configuration 1 consists in blocking the flow of the outer layer, as it can be observed in Figure 36.

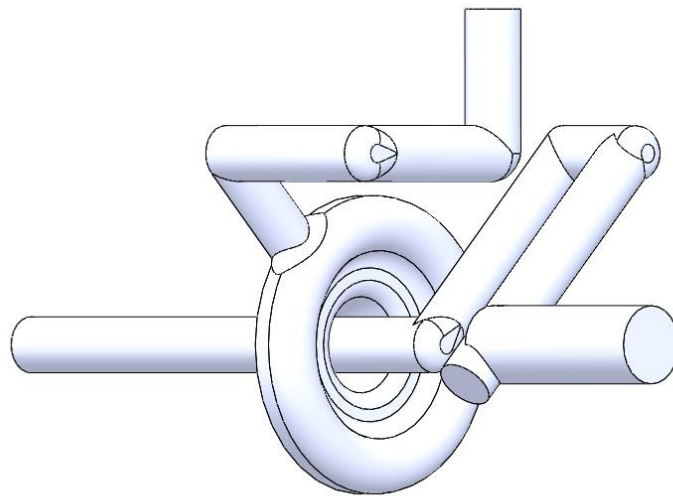


Figure 36 - Geometry of the coextrusion die flow channels using Configuration 1.

While Configuration 2, the only modification made to the die was to redirect the sheath material to the second distributor (extending the channel), where the two materials will join, forming the filament, and the core material was directed to the central channel and to the first distributor, as illustrated in Figure 37.

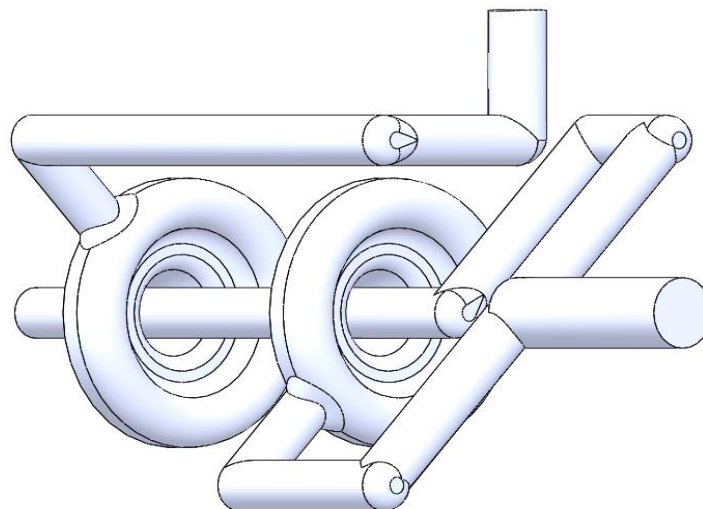


Figure 37 - Geometry of the coextrusion die flow channels using Configuration 2.

The two configurations will be simulated in order to identify the configuration that allows a more stable process, thus producing filaments with the best possible properties and characteristics.

Regarding to the operating conditions, the mass flow rate used in all the filament coextrusion simulations performed in this section was equal to the one used in the experimental procedure, which was 729.12 g/h .

3.3.2 Mesh and boundary conditions

The required meshes to run the simulations were created using the utility *cfMesh*, since the geometries used (Configuration 1 and Configuration 2) are quite complex. For that two STL file that contains the geometry data of the flow channel for each configuration, was generated with the help of SolidWorks. The subsequent step in the process was the definition the geometry boundaries using the opensource CAD *software* Salome.

According to Figure 35, the two inlets and the outlet faces are defined with type *patch*, which means that the fluid can enter (inlet) or exit (outlet) the channel through those faces. The rest of the geometry faces are defined with type *wall*, in which a null velocity must be imposed. Those boundaries must be saved in a STL file that will be used by *cfMesh* to create the mesh.

The maximum cell size defined for the first mesh (M1) created was 0.15 mm , then in order to perform a mesh refinement study, two more meshes were created applying a mesh refinement factor equal to 1.5. This means that at each refinement done the number of cells increases circa 3.2 times.

In order to provide a visual information about the detail of the refinement of the created meshes, in Figures 38 are presented the coarsest and the more refined meshes of the Configuration 2 geometry. Table 13 provides some data about these three meshes, being possible to observe the maximum cell size used and the increase of mesh cells in each mesh refinement.

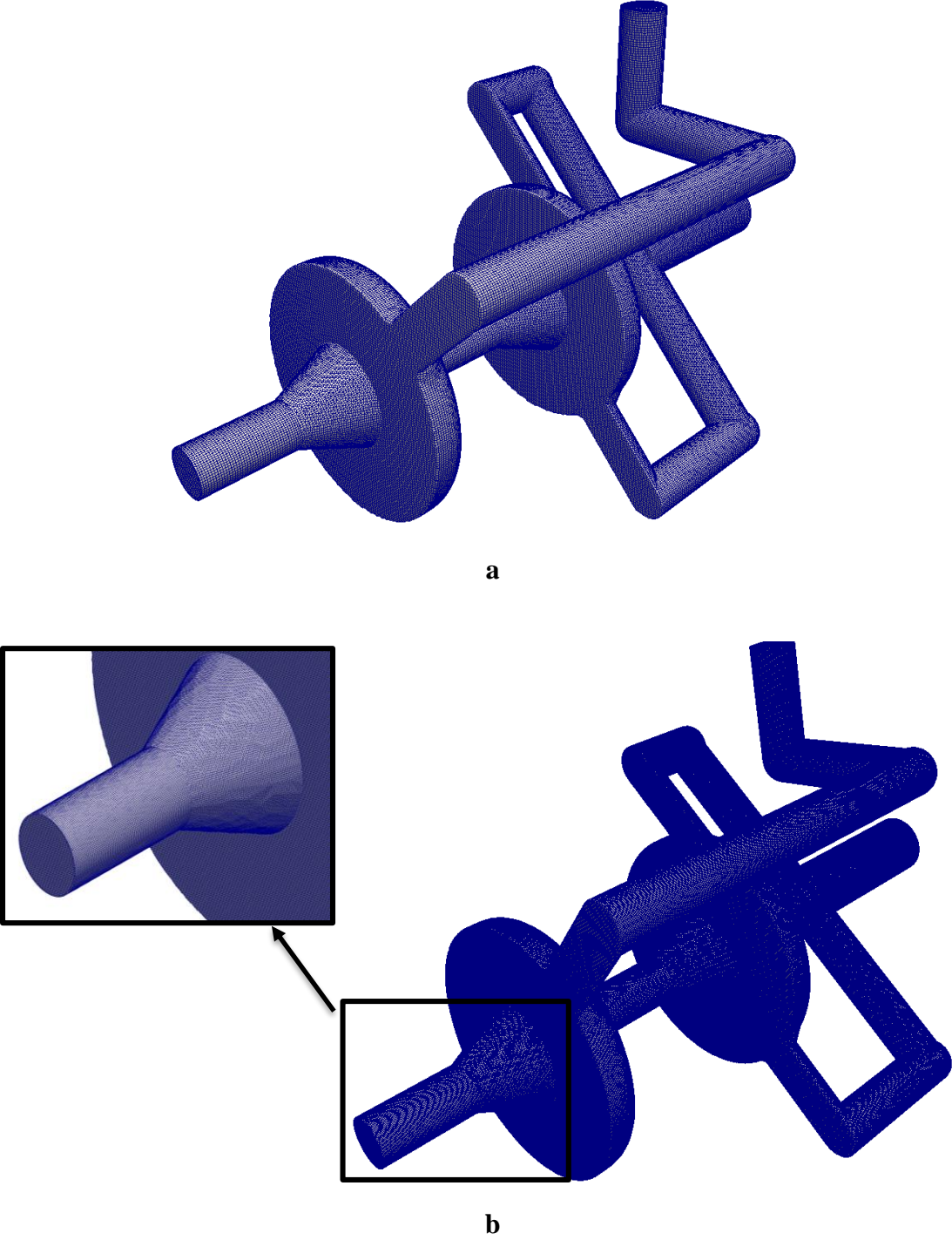


Figure 38 - Meshes created using Configuration 2 geometry: (a) coarser mesh (M1) and (b) more refined mesh (M3).

Table 13 - Relevant information about the meshes created using Configuration 2.

	Mesh 1 (M1)	Mesh 2 (M2)	Mesh 3 (M3)
Maximum cell size (mm)	0.15	0.1	0.067
Number of points	663644	2072491	6477170
Number of cells	590961	1907738	6106561

In terms of boundary conditions, the pressure and the velocity in all the different boundaries must be defined. Regarding the velocity, only in the two inlets is mandatory to compute de velocities, since it is assumed that there is null velocity at the walls and at the outlet the velocity is equal to the known velocity of the last mesh cell (*zeroGradient*). In order to compute the inlet velocity for each blend, Equations 3 and 4 were used with the respective inlet diameters (2.1 mm for the Blend B inlet and 1.5 mm for the Blend A inlet), the total mass flow rate and the percentage of each material in the filament (67% of Blend B and 33% of Blend A), which should be used to compute the mass flow rate of each individual blend. Table 14 summarizes the values obtained.

Table 14 - Inlet velocities of the Blend A and B in the coextrusion process.

	Inlet 1 (Blend B)	Inlet 2 (Blend A)
Total mass flow rate (g/h)	729.12	
Percentage (%)	67	33
Mass flow rate (g/h)	488.51	240.61
Density (kg/m³)	919.1	937.9
Inlet velocity (mm/s)	10.7	10.1

In terms of pressures, since the velocity is fixed at the inlets and walls, the pressure in this boundaries is set to *zeroGradient* and the outlet pressure is set as *fixedValue* and has a value equal to 0.

3.3.3 Results and discussion

Selection of the channels geometry configuration

The two configurations described above were tested to identify the configuration that allows a more stable process thus producing filaments with a stable interface between the two materials. Only one simulation was performed for each configuration, using the coarser mesh (M1) parameters. The end time of the simulations was set to 9 seconds and with a time step equal to 1×10^{-4} seconds. The simulation was performed using the adjustable time step option, which as the name implies, adjusts the time step in order to obtain convergence as soon as possible, thus minimizing the computational time. So the time step used was approximately 6.4×10^{-4} seconds.

Figure 39 shows the interface between the two materials at the exit of the die for two different simulation times, using Configuration 1. Figure 40 shows the flow of the materials along the coextrusion die using configuration 1.

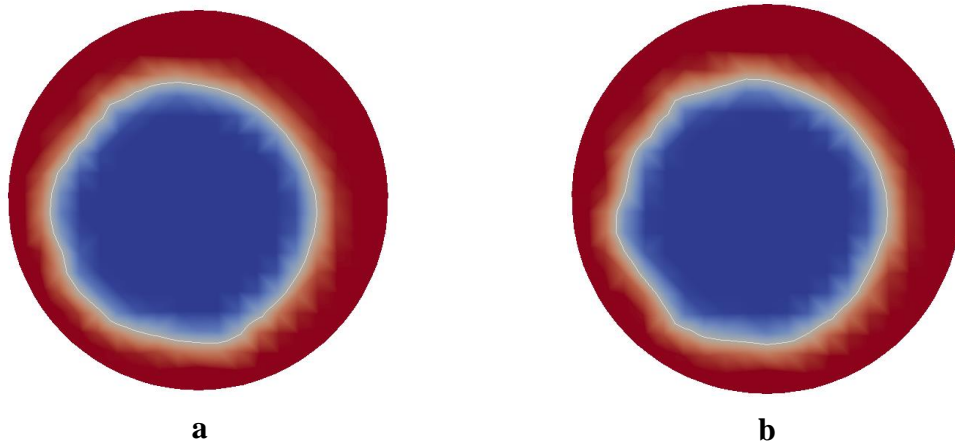


Figure 39 - Interface between the two materials at the die exit at (a) 7 seconds and at (b) 9 seconds for configuration 1.

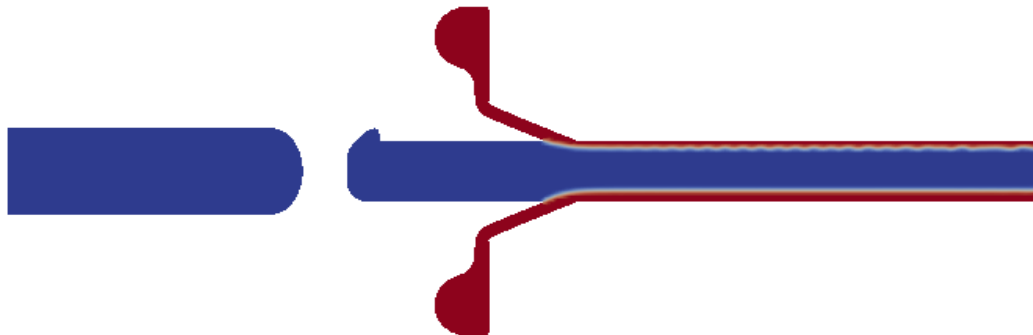


Figure 40 - Flow along one transversal section of the coextrusion die using configuration 1.

From Figure 39 it can be observed that the interface between the sheath and the core material does not remain constant over time. The geometry used promotes prolonged contact between the two materials, which together with the viscosity difference between the two blends causes the appearance of a wave like flow in the die parallel zone, as it is possible to observe in Figure 40, causing distortions in the interface. Considering the results achieved, it is possible to conclude that a geometry that promotes a less prolonged contact between the blends will be most suitable.

The simulation results for the Configuration 2 are represented in Figures 41 and 42, wherein in Figure 41 shows the interface between the two materials at the exit of the die for two different simulation times and in Figure 42 it is represented the flow of the materials along a transversal section of the die.

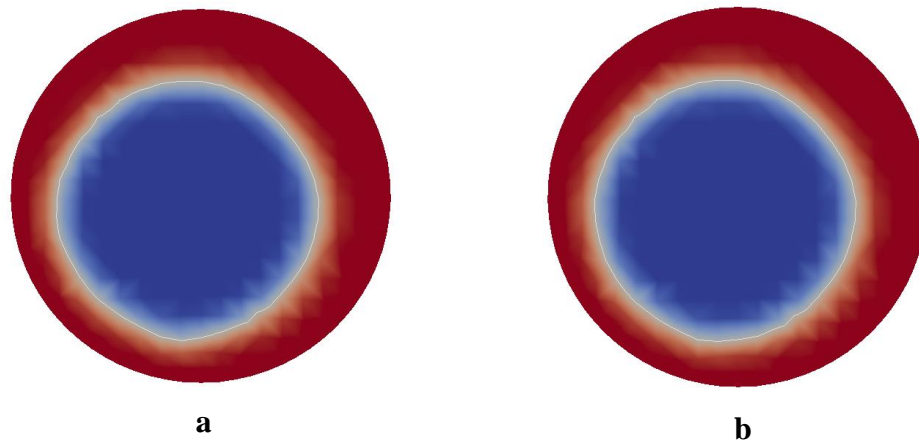


Figure 41 - Interface between the two materials at the die exit at (a) 7 seconds and at (b) 9 seconds for configuration 2.

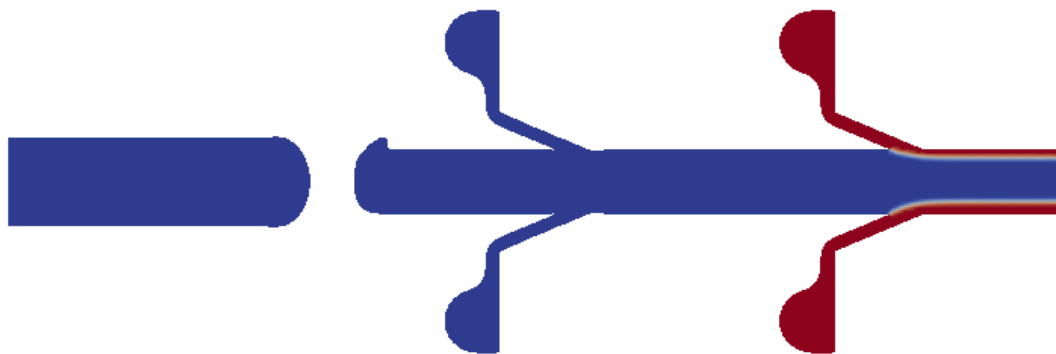


Figure 42 - Flow along one transversal section of the coextrusion die using configuration 2.

The interface of the sheath and core is more stable than the interface developed using configuration 1, but still presents very small variations with the time as Figure 41 shows. Analysing Figure 42 it is possible to observe that the flow is much more regular

and presents less instabilities, which contributes to achieving a more regular interface between the core and the sheath, and thus grants filaments with the best properties possible. Attending to this results, the Configuration 2 was used in all the filament coextrusion simulations hereafter.

Selection of the minimum end time of the simulations

Before run the remaining simulations, using the simulation of the Configuration 2 presented in the previous point, it was assessed what is the minimum time to be simulated that ensure a stable process, which was mainly done to save computational effort (due to the high number of cells in the created meshes).

Firstly, the residuals were plotted in order to find out whether the time simulated is sufficient for the same stabilize, thus achieving an accurate solution. Since the solver used (*interFoam*) primarily solves the pressure correction equation and then corrects the velocity field, the usual calculation of the momentum predictor, shown to be detrimental for convergence (Henry, 2005), thus only the residuals of the pressure are available for analysis. In Figure 43 the evolution on the simulation residuals during time can be observed.

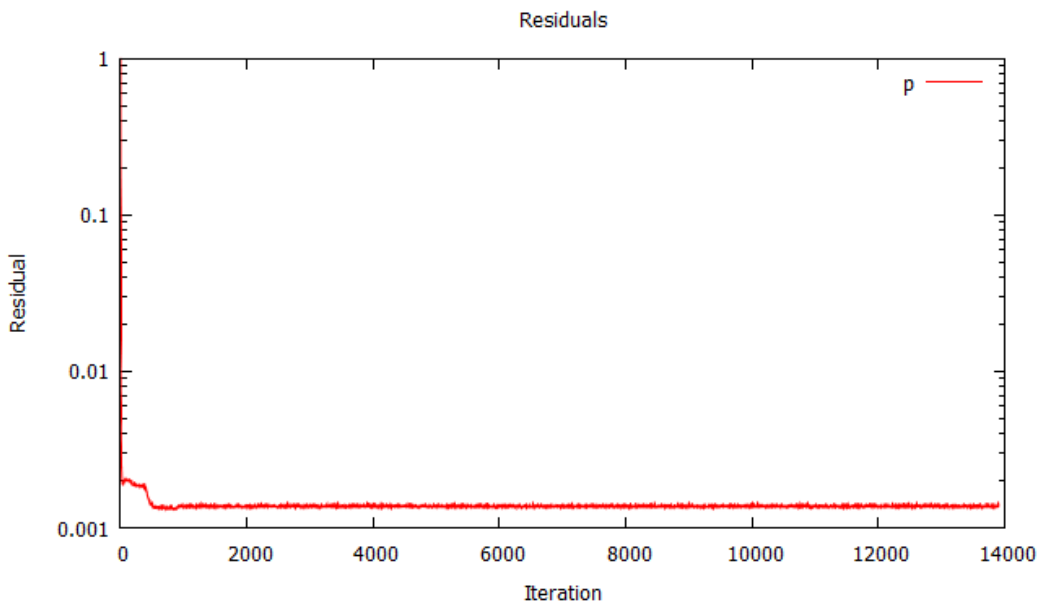


Figure 43 - Evolution of the residuals along the simulated time in the coextrusion process.

Through the analyses of Figure 43, it is possible to observe that after more or less 0.64 s (1000 iterations) the pressure residuals tend to stabilize at low value, thus ensuring an accurate solution.

But checking the interface geometry at the outlet, the pressure and the velocity along the simulated time it was observed that the interface and the pressure do not stabilize, presenting small changes over time. In Table 15 are presented the pressure and velocity values for four different points of the domain along the simulated time, whose locations are presented in Figure 44.

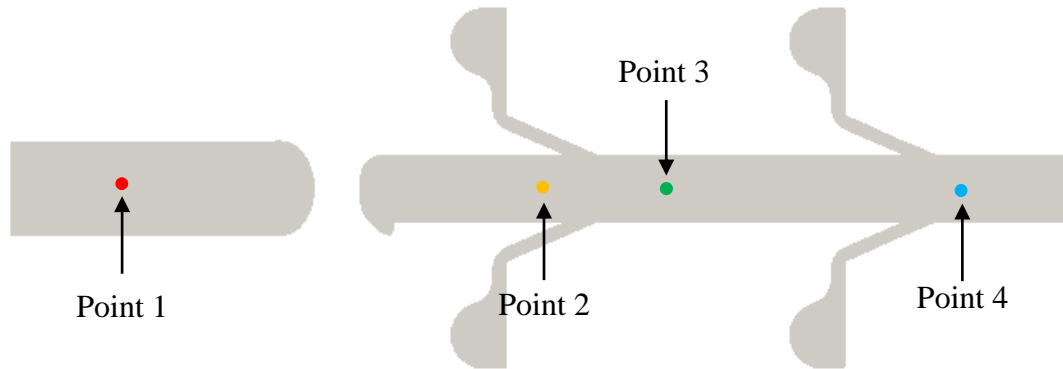


Figure 44 - Location of the four points of the domain used.

Table 15 - Evolution of the velocity and pressure values in four different points along the simulated time.

Time (s)	Point 1		Point 2		Point 3		Point 4	
	U (m/s)	P (MPa)	U (m/s)	P (MPa)	U (m/s)	P (MPa)	U (m/s)	P (MPa)
0	0	0	0	0	0	0	0	0
1	0.016	4.6	0.017	1.61	0.031	1.33	0.052	0.488
2	0.016	4.63	0.017	1.63	0.031	1.34	0.052	0.49
3	0.016	4.61	0.017	1.61	0.031	1.33	0.052	0.491
4	0.016	4.62	0.017	1.62	0.031	1.33	0.052	0.49
5	0.016	4.61	0.017	1.62	0.031	1.34	0.052	0.489
6	0.016	4.59	0.017	1.6	0.031	1.32	0.052	0.486
7	0.016	4.61	0.017	1.62	0.031	1.33	0.052	0.488
8	0.016	4.62	0.017	1.61	0.031	1.33	0.052	0.49
9	0.016	4.61	0.017	1.62	0.031	1.33	0.052	0.489

Analysing Table 15, it is possible to observe that in all four points the velocity stabilizes at circa 1 s and although the pressure values are floating, the differences between these are not very significant.

Regarding the interface, analysing the results was noticed that from 4.5 seconds the changes in the interface location were residual, as it can be observed through Figure 45, that shows the interface location after 2.5, 4.5 and 5.5 seconds.

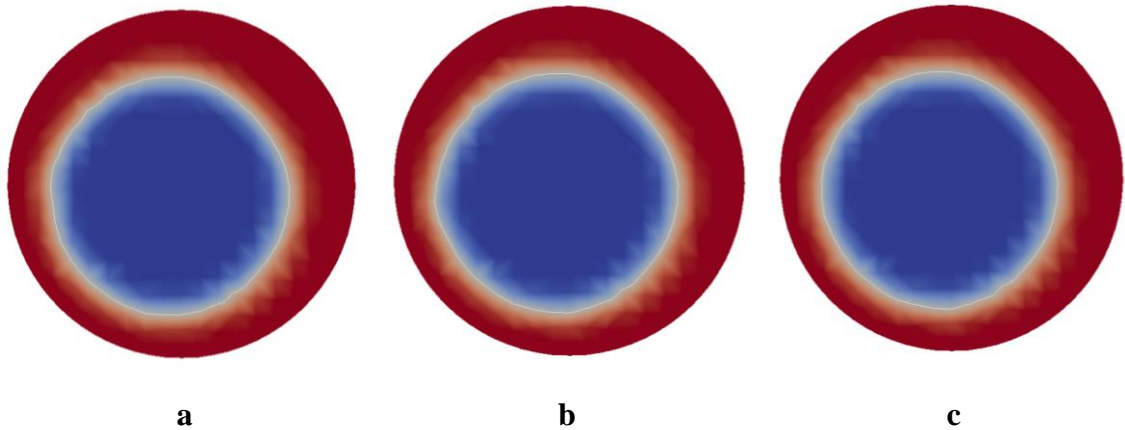


Figure 45 - Interface location between the two materials at 2.5 seconds (a), at 4.5 seconds (b) and at 5.5 seconds (c).

Considering all the facts stated above, the minimum time that permits to reach a steady process for the processing conditions simulated in the next case studies was defined as 4.5 s.

Assessment of the pressure drop prediction capabilities

The first computational result to be compared with the experimental one was the pressure field. The pressure drop along the coextrusion die obtained with the more refined mesh is shown in Figure 46.

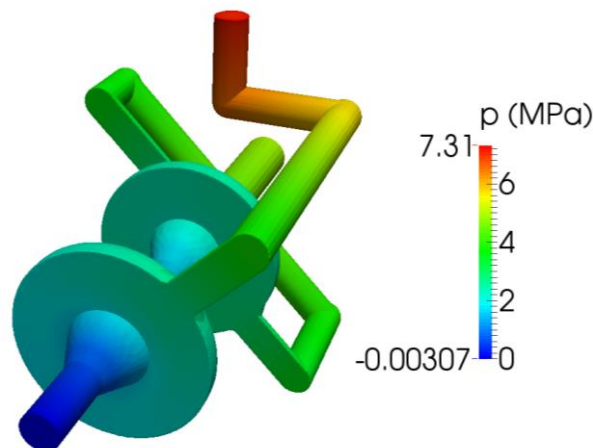


Figure 46 - Pressure drop along the coextrusion die obtained with the more refined mesh.

Analysing Figure 46 it is possible to conclude that the pressure decreases smoothly and monotonically along the flow channel.

In order to compare the pressure drop measured experimentally with the equivalent obtained using the simulations, it is necessary to obtain the pressure at the exact local where the sensor pressure was mounted. The sensor was mounted in the

channel that transports the blend used to produce the core of the filament and in a section of the channel that was not represented in the 3D file of the die, thus it was not possible to include that section in the geometry used in the simulations presented in Figure 37. Hence, the pressure drop in the missing channel region, which has a length of 40 mm, was computed through Equation 14 (Carneiro & Nóbrega, 2012), which represents the total pressure drop in a circular channel, using the Power Law constants for Blend B and that value was added to the pressure provided by the simulation for the last superior point in the inlet of the blend.

$$\Delta P = \frac{2kL}{R^{(3n+1)}} \left(\frac{4Q}{\pi} \right)^n \quad (14)$$

where ΔP (MPa) is the pressure drop, k (Pa.sⁿ) is the consistency index, L (m) is the length of the channel, R (m) is the radius of the channel, n is the Power Law index and Q (m³/s) is the flow rate of the Blend B.

The pressure values at the die inlet and the pressure drop corrected using Equation 14 are given in Table 16.

Table 16 - Values of pressure at the die inlet, in the missing section and the corrected pressure.

	Mesh 1 (M1)	Mesh 2 (M2)	Mesh 3 (M3)
Pressure drop at the inlet (MPa)	4.91	4.94	4.98
Pressure drop in the additional region (MPa)	1.11		
Total pressure drop (MPa)	6.02	6.05	6.09

Analysing the total pressure drop obtained in the three meshes, it is possible to observe that all the values are almost coincident, which means that the solutions are almost independent of the degree of refinement in the mesh.

The values of the corrected pressure were plotted in a graph of pressure in function of the mesh cell size. The points were approximated with a quadratic function, where the

point that intercepts the y axis corresponds to the pressure value in an infinitely refined mesh. The graph in study is illustrated in Figure 47 (both axes are in logarithmic scale).

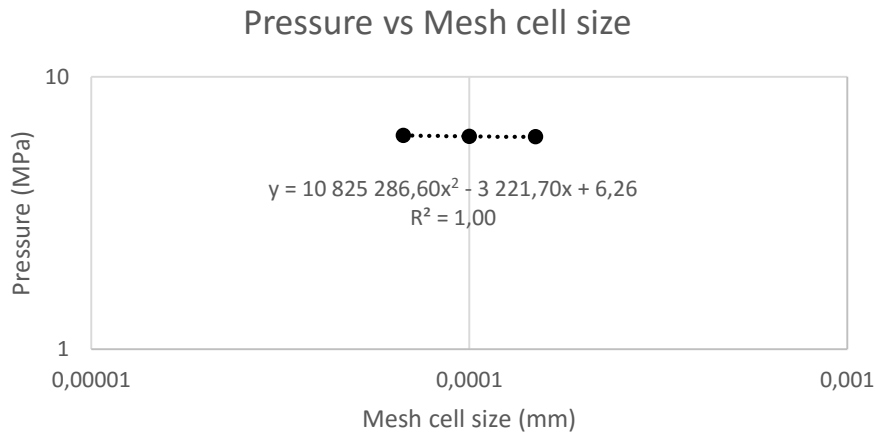


Figure 47 - Pressure in function of the mesh cell size.

Through the analysis of Figure 47, it is possible to conclude that the points represented fit perfectly to a quadratic function, wherein the determination coefficient (R^2) is 1 which means that the error between the function and the three points is null. Using the equation of the quadratic function shown in the graph, the interception of the function with the y axis represents an extrapolation of the value for a mesh with null cell size, a methodology similar to the Richardson extrapolation. In this way, the pressure drop value obtained in the infinitesimally refined mesh is 6.26 MPa.

The solver accuracy to predict the pressure drop value can be assessed by computing the relative error between the extrapolated pressure drop to the infinitely refined mesh and the experimental pressure value, which has a value of 6.19 MPa. The error obtained has a value of 1.13%, meaning that the solver gives a good prediction of the pressure drop along the die.

Assessment of the interface prediction capabilities

Regarding the interface location results, the methodology described and used in Section 1 to isolate the interface points was also applied in this case study, to identify the interface points coordinates at the outlet (the interface can be observed on Figure 45b). Those points were then plotted in a graph presented in Figure 48.

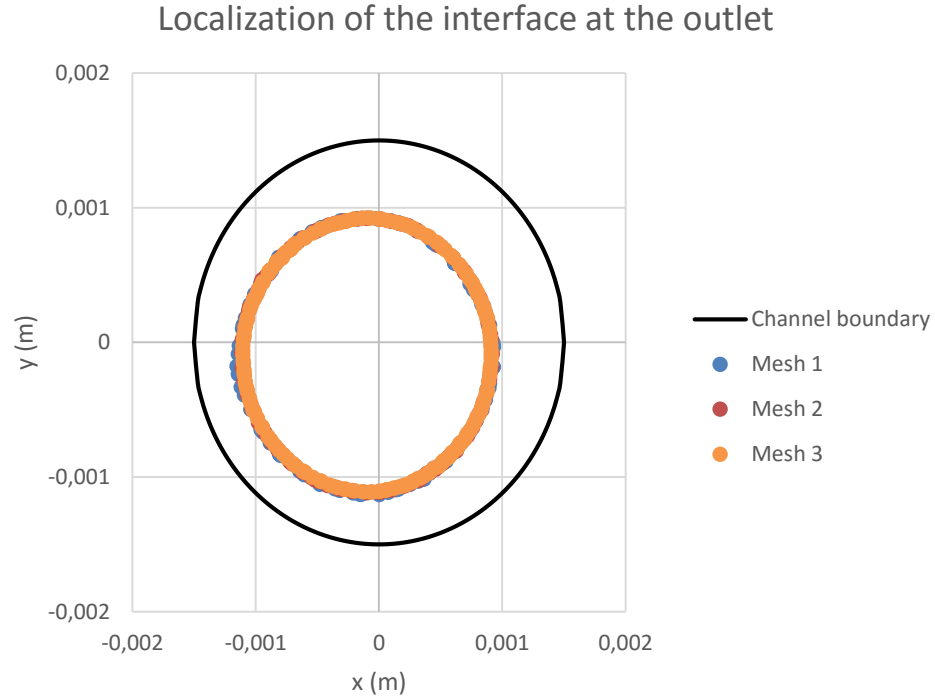


Figure 48 - Interface location at the outlet in each mesh used.

The interface locations obtained in the three meshes are almost coincident, which means that the solutions are almost independent of the degree of refinement in the mesh. In addition, it was found that the interface centre location is not equal to the centre of the channel. To quantify and study the centre and the eccentricity of the interface in the two blends, the interface points were fitted to the equation of an ellipse, given by Equation 15, using the *Solver* tool provided with Microsoft Excel.

$$\left(\frac{x-h}{a}\right)^2 + \left(\frac{y-k}{b}\right)^2 = 1 \quad (15)$$

where h and k are the ellipse centre coordinates, and a and b are the ellipse semi axis.

Table 17 presents the values of the ellipse constants for the three meshes used, and also the extrapolated values using Richardson extrapolation, i.e., for an infinitely refined mesh.

Table 17 - Constants of the ellipse equation for all meshes and the ones calculated using the Richardson extrapolation.

	Mesh 1 (M1)	Mesh 2 (M2)	Mesh 3 (M3)	Richardson extrapolation
<i>h</i> (mm)	-0.11	-0.097	-0.0962	-0.0961
<i>k</i> (mm)	-0.1	-0.096	-0.093	-0.092
<i>a</i> (mm)	1.04	1.02	1.01	1
<i>b</i> (mm)	1	1.011	1.009	1.01

As stated before it can be seen, from the results presented on Table 17, that the interface centre is slightly off the channel centre, since the h and k constants are not null. In addition, it was found that the interface centre is deviated circa 0.1 mm in the negative x -axis and y -axis in relation to the channel centre. As the constants a and b are slightly different from each other it is possible to compute the ellipse eccentricity (e), through Equation 16.

$$\frac{\sqrt{a^2 - b^2}}{a} = e \quad (16)$$

The value of e computed, using the extrapolated constants values, is 0.14, which confirms that the interface is not a circumference, for which the e value is 0.

Using the constants calculated with the Richardson extrapolation it is possible to plot the equation of the ellipse in order to compare that interface with a picture of the filament cross section produced experimentally. Figure 49 represents the interface between the two blends through the equation of the ellipse calculated using the Richardson extrapolation and Figure 50 the microscopy picture of the filament.

Representation of the interface using the ellipse

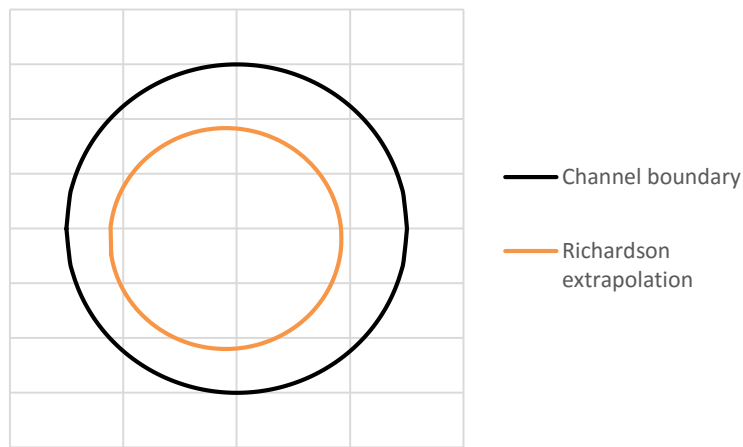


Figure 49 - Interface shape obtained using the extrapolated parameters.

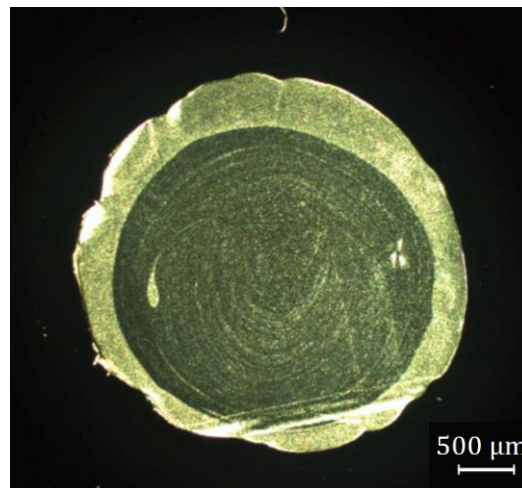


Figure 50 - Microscopy picture of the produced filaments (Abreu, To be published).

Comparing the two figures it is possible to conclude that the simulation results are very similar to the filament microscopy picture, showing that the interface is not centred and the interface has an ellipse-like form, confirming all the results presented before, and causing an uneven thickness on the sheath layer.

Considering the results relative to pressure and interface location, it can be concluded that *interFoam* solver showed to be suitable to simulate the filament coextrusion process, producing reliable and accurate results very similar to the reality.

4. DESIGN OF A SEMI INDUSTRIAL MULTIFILAMENT COEXTRUSION DIE

The results presented in Sections 2 and 3 show that OpenFOAM® framework is an appropriate tool to simulate coextrusion processes, mainly due to the very good agreement obtained between numerical and experimental results. Thus, in this section that tool will be used to support design and the optimization of a semi industrial multifilament coextrusion die, in order to minimize the probability of possible instabilities that could occur during the actual coextrusion process.

The die conceived had to meet some requirements that had been imposed by the company. Firstly, the die must be capable to coextrude two different materials (Blend A forms the sheath and Blend B forms the core of the filament) with several different percentages of each one, and with that should allow to modify the filament configurations depending on the specific application to be used. The second requirement is that the die must be capable to coextrude simultaneously 10 filaments with 1,1 *mm* of diameter at the die exit. The die has also to be capable to coextrude filaments at a mass flow rate between 1,8 *kg/h* and 2,4 *kg/h* without flow instabilities, thus ensuring a good operative window. Lastly, in order to save time and resources, the global measures and the die connections have to be equal to a die that already exists at the Lankhorst company. This will allow the use of the same heater and connections to the extruders for both dies, the currently available and the new to be designed.

4.1 Die constructive solution

As already stated, there are a few specifications for the coextrusion die to be designed, being the most important, in terms of design, the fact that the new die need to have the same size and geometry as the die that Lankhorst owns. The “model” die has cylinder like geometry, with height and diameter, respectively, of 77 *mm* and 110 *mm*. The complete die comprises three parts: the die frame, which has a diameter and height of 110 and 62.5 *mm*, respectively, the spinneret and the cover, that allows to secure the spinneret in the die frame and which has a diameter and height of 110 and 13.5 *mm*,

respectively. The die that will be developed must use the same cover and possess a die frame similar to the old one, containing the original geometry and measures. Figure 51 shows the assembly that includes the die owned by Lankhorst and the respective heater, which gives an idea of the global measures and the final format of the tool.

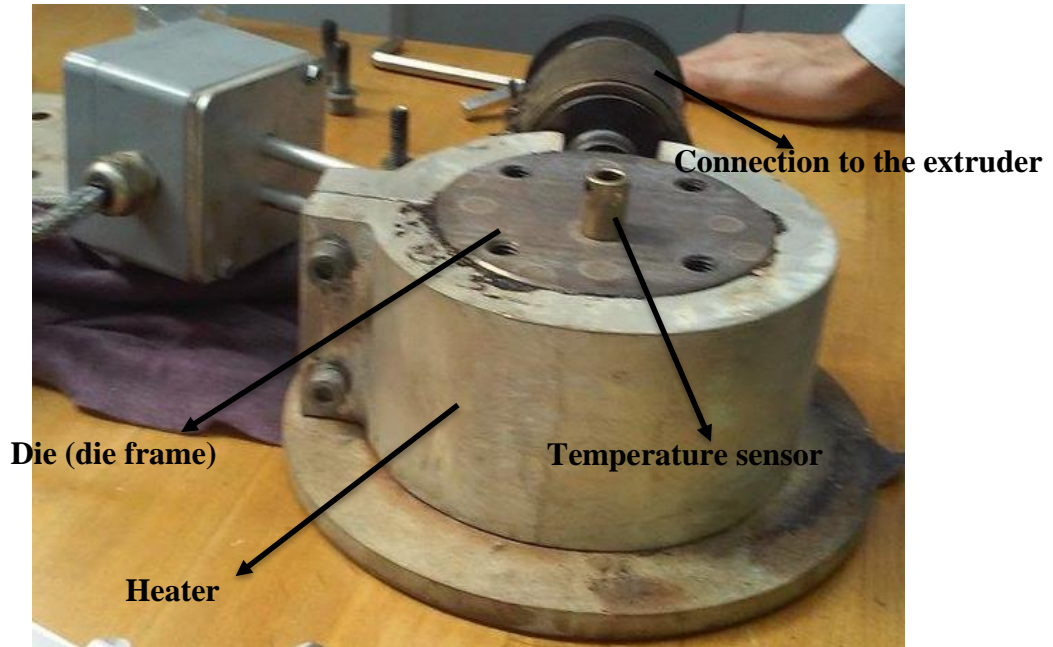


Figure 51 - Assembly of all the components that composes the die that Lankhorst owns.

Regarding to die channels, attending to all the requirements and especially to the design requirement already explained, two different constructive solutions for die channels design were considered. In Figures 52 and 53 two preliminary 3D drawings that illustrate the two possible solutions are shown.

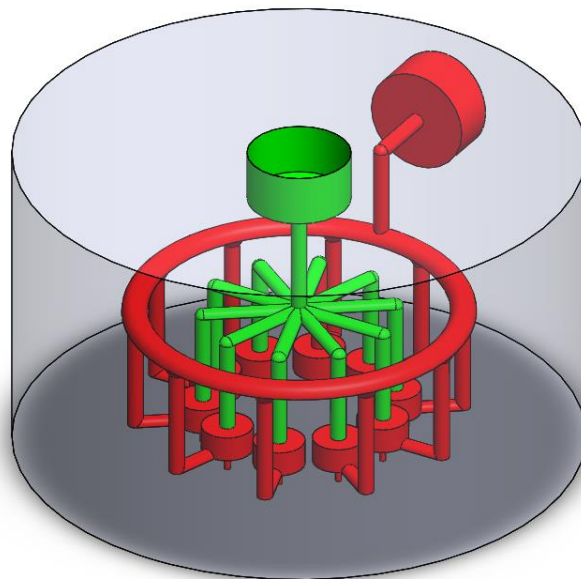


Figure 52 - Design of the multifilament coextrusion die channels for Solution 1.

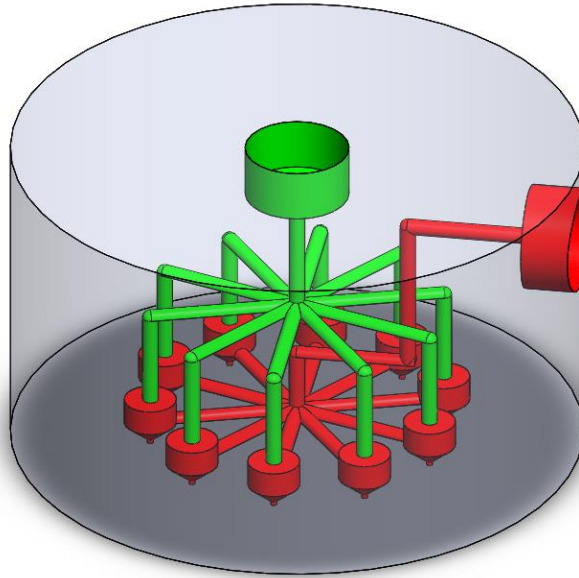


Figure 53 - Design of the multifilament coextrusion die channels for Solution 2.

The main difference between the two solutions is the way the sheath material, represented by the red channels, is guided to the distributor where the two materials are joined forming the filament with the required diameter and material distribution. In Solution 1 the sheath material enters the die and is guided to a circular channel that distributes the sheath material by ten individual channels which are connected to each distributor, while in Solution 2 when the material enters the die it is guided by two channels to the die centre where it is distributed by ten channels that lead to the individual distributors. In both solutions the core material, represented by the green channels, enters the die and the flow is divided in ten channels that leads to the distributors.

The chosen solution was the Solution 2 due to its inherent balance, because whatever the path that the sheath material enters through, the distance travelled to the distributor is always the same, which does not happen in Solution 1, as it can be concluded by the analysis of Figures 52 and 53. That fact helps to reduce the probability of unconformities caused by uneven flow distribution.

The channels and the distributors were dimensioned following an iterative methodology, in order to achieve a solution that produces a stable flow without instabilities. After that, two typical values for the angle defined between the distributor convergent channel and the outlet channel considered, which are 60° and 70° , will be tested using the simulations and the chosen value will be the one that will enable the production of a filament with an interface between the two materials as stable and centred

as possible, with the smallest pressure drop possible. The approaches followed in the dimensioning of the channels and the distributors and the results achieved will be presented more ahead in this section.

Considering the design solution of the channels and the overall design requirements, a modular die was conceived where the modules (four) are inside the die frame and all these modules form the flow channels. That configuration was chosen in order to make it easier to manufacture the die, because due to the complexity of the flow channels geometry their machining in a single metal block would be impossible. Hence, with this solution it is possible to machine the channels in individual metal parts and then those parts could be assembled inside the die frame to construct the channels. The other advantage of this solution is the possibility to perform corrections of the channels without the need to make a new die, being only changed the module that contains the channel to be modified. In Figures 54(a) and 54(b) are presented the 3D model of the designed die and a down view of that model, respectively, where is possible to observe all components of the die and the modular solution adopted.

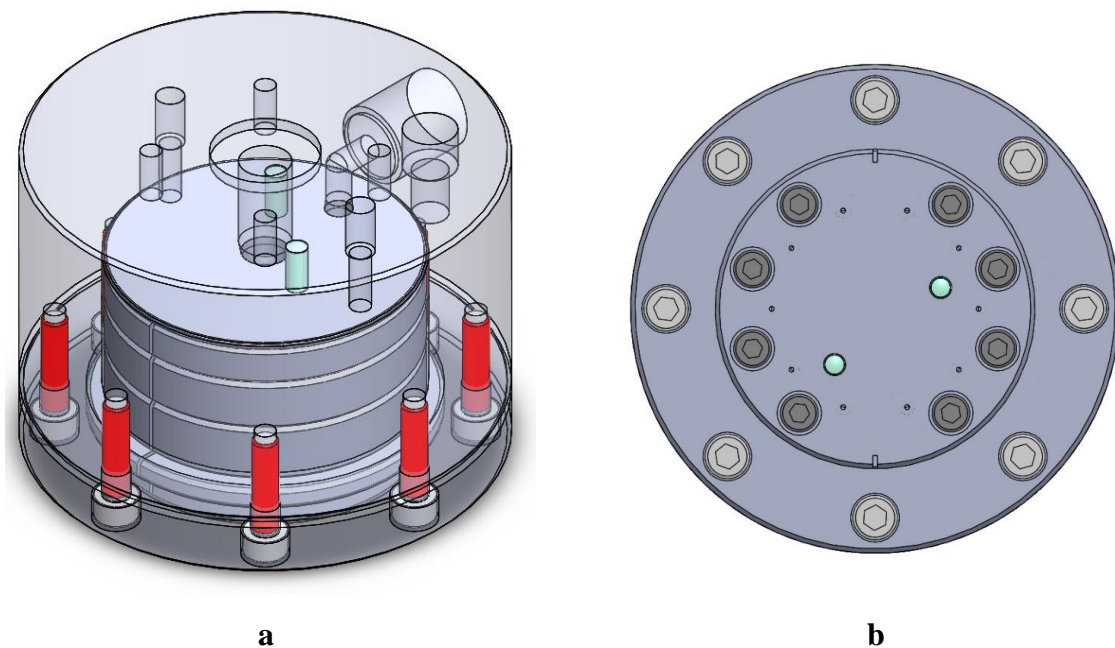


Figure 54 - Overall view of the 3D model of the designed die (a) and bottom view of the 3D model of the designed die (b).

From Figure 54 it is possible to identify all the parts that compose the final design of the die. Besides the components that already have been mentioned before, two different sets of screws are needed (one is M5x55 and the other is M6x25) in order to fix the components that could move in the right place. Two pins, with diameter and length of 5 mm and 60 mm, respectively, are also needed in order to avoid the misplacement (by rotation) of the modules. In the die frame it is possible to notice some holes that are needed to mount and bolt the adaptors to make the connections between the die and the extruders, and a connection to mount a temperature sensor in order to provide a better control of the process to the user.

4.2 Mesh and boundary conditions

Regarding the geometry, attending to the complexity of the channel system designed, only the distributor together with the die exit will be simulated because in theory that is the only place that can promote uneven flow (notice the upstream regions are geometrically identical). This allows to reduce the effort of the calculations. In Figure 55, it is illustrated the typical geometry of the distributor used to create the mesh. The methodology applied in the creation of the mesh was the same that has been used to create the mesh of the coextrusion die, which is described in Section 3.

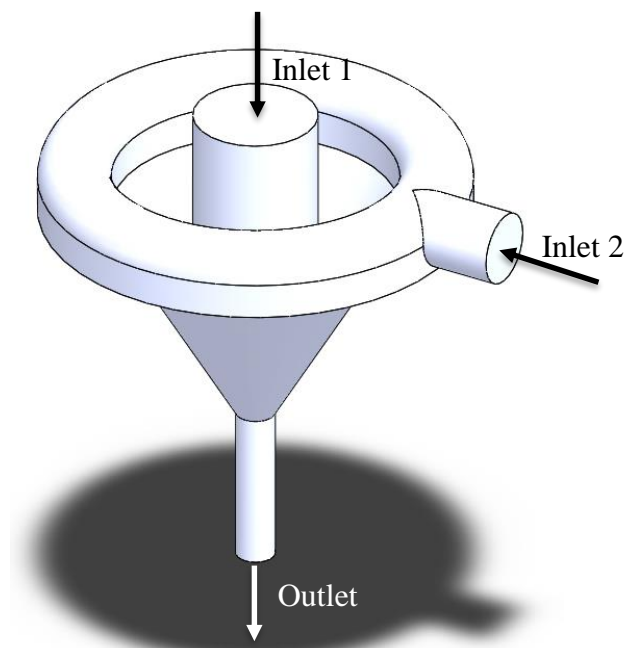


Figure 55 - Typical geometry of the distributor used to create the mesh.

During the dimensioning of the channels, the measures of the channels, namely the diameters of the inlets and the height of the circular channel, the geometry of the distributor, the thickness and the angle of the convergent channel were changed in order to attempt to reach a design that ensures a stable process, thus requiring the creation of a high number of meshes.

The maximum cell size defined to create the required meshes was 0.11 mm and, because that number was not sufficient to create the convergent channel in some of the meshes created, in that specific part of the geometry a factor of refinement equal to 2 was defined when necessary, which means that the maximum cell size in that region is equal to 0.055 mm . Due to the large number computational cells, the computational time needed to reach a solution could range from three days to two weeks (depending on the geometry and the mesh parameters used), so if more refinements were made to the mesh, the simulations of those meshes would take a huge computational time, in the range of months, and need a large amount of computational resources. Considering the previous facts and the high number of simulations that may be necessary to run, after careful consideration was decided that is not worth to perform those refinements to the original mesh, since the degree of refinement of the mesh is similar to the one adopted in the previous sections, therefore accurate results are expected. In Figure 56 is presented an example of the typical mesh created and used in the simulations and in Table 18 some data about that mesh is listed.

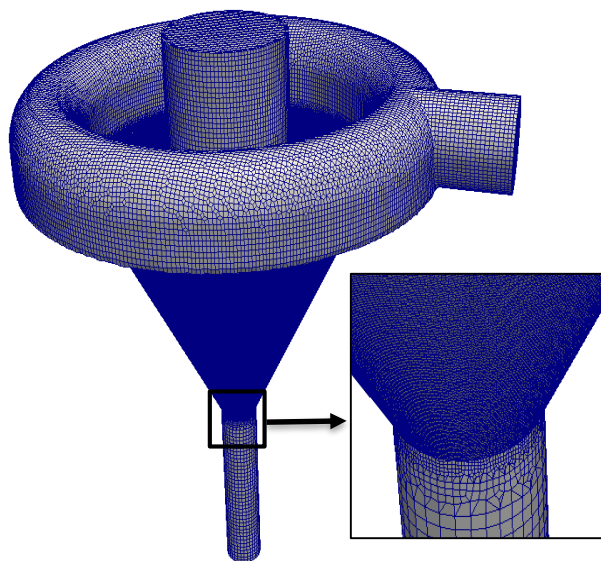


Figure 56 - Example of a typical mesh used in the simulations.

Table 18 - Relevant information about the example of a typical mesh used in the simulations.

	Mesh 1 (M1)
Overall maximum cell size (mm)	0.11
Maximum cell size at the convergent channel (mm)	0.055
Number of points	1822924
Number of cells	1407078

The boundaries defined are also equal to the coextrusion case studied in Section 3, where the two inlets and the outlet faces are defined with type patch, which means that the fluid can enter (inlet) or exit (outlet) the channel through those faces and the rest of the geometry faces are defined with type wall, in which a null velocity must be imposed.

Concerning the boundary conditions, like in the previous coextrusion case, the velocity only has to be imposed at the inlets.

Thus, to compute the velocities of each blend at the respective inlet, it is necessary to apply Equations 3 and 4 using the diameters of the inlets, the total mass flow rate (for one distributor) and the percentage of each material in the filament, which is used to compute the mass flow rate of each individual blend. Following the specifications of the die to be designed, the die has to work at different flow rates and with many different relative percentages of each blend. Hence, seven simulations were performed, in order to test the coextrusion die with different total and relative flowrates. The Reference case was defined based on the company indications, and was used for the most detailed design studies performed. Table 19 summarizes the conditions employed for all the cases in study.

Table 19 – Inlet velocities of the Blend A (inlet 2) and Blend B (inlet1) in the coextrusion process.

	Reference		Case 1		Case 2		Case 3		Case 4		Case 5	
	Core	Sheath	Core	Sheath	Core	Sheath	Core	Sheath	Core	Sheath	Core	Sheath
Total mass flow rate (kg/h)	0.24		0.18		0.24							
Percentage (%)	74.5	25.5	74.5	25.5	90	10	80	20	70	30	60	40
Mass flow rate (g/h)	178.8	61.2	134.1	45.9	216	24	192	48	168	72	144	96
Density (kg/m³)	919.1	937.9	919.1	937.9	919.1	937.9	919.1	937.9	919.1	937.9	919.1	937.9
Inlet velocity (mm/s)	5.7	5.5	4.2	4.3	6.9	2.2	6.1	4.3	5.3	6.5	4.6	8.7

The pressure boundary conditions are the same as in the coextrusion case presented in Section 3. All the boundary conditions are defined in the same type of files that were mentioned in Section 3.

4.3 Results and discussion

Selection of the minimum end time of the simulations

Initially, all the coextrusion simulations used to dimension the channels and the distributor were performed up to 9 seconds, using the adjustable time step option enabled, being the average time step used approximately 6×10^{-5} s. However, due to the increased complexity of the geometries under study the computational meshes require a large number of cells (the more complex meshes contain a number of cells between 1400000 and 1900000). Thus, the computational time required to obtain converged results increases, for instance, the last iteration took circa 2 weeks to run (in a 24 processors parallel run). So in order to reduce the computational time, the range of time covered required to achieve fully developed conditions was studied in detail.

Similarly to the methodology followed in Section 3, the residuals of the linear algebraic systems of equations were plotted and it was possible to find out whether the minimum time for the residuals stabilize at low values and consequently, ensure an accurate solution. Figure 57 shows the evolution on the simulation pressure residuals during the iteration time.

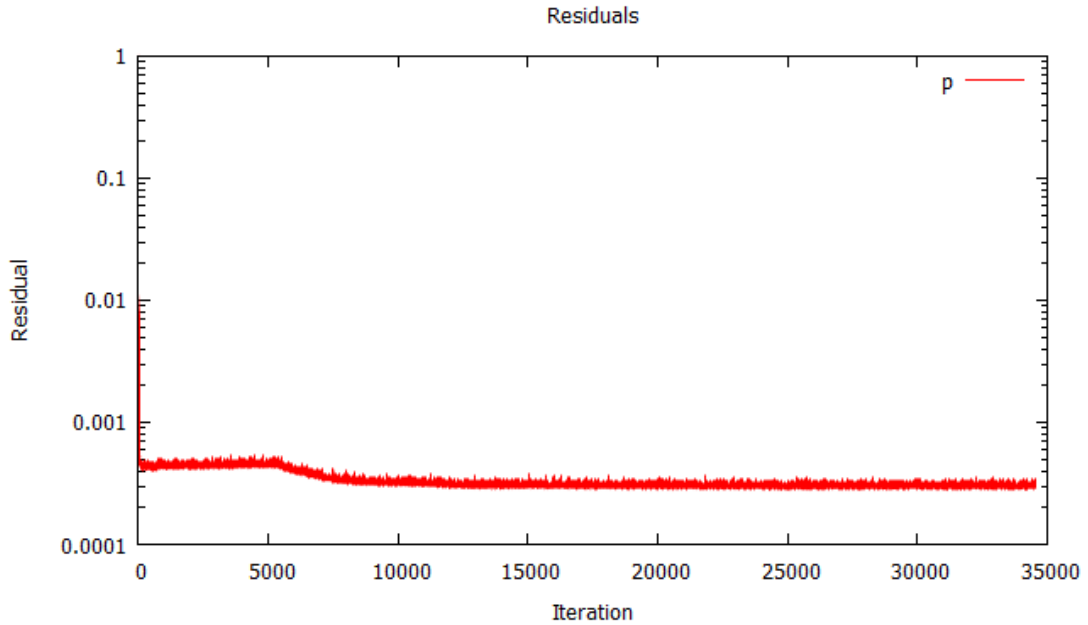


Figure 57 - Evolution of the residuals along the simulated time in the coextrusion process.

Although in Figure 57 is not represented the residuals for the whole simulated time, it is possible to note that at approximately 10000 iterations (0.6 s) the pressure residuals tend to stabilize at low values, thus ensuring an accurate solution.

In order to find out the minimum time required to reach steady state conditions, the evolution of velocity and pressure was monitored in four different points of the computational domain, as presented in Figure 58. The velocity and pressure data taken in those point along time is presented in Table 20.

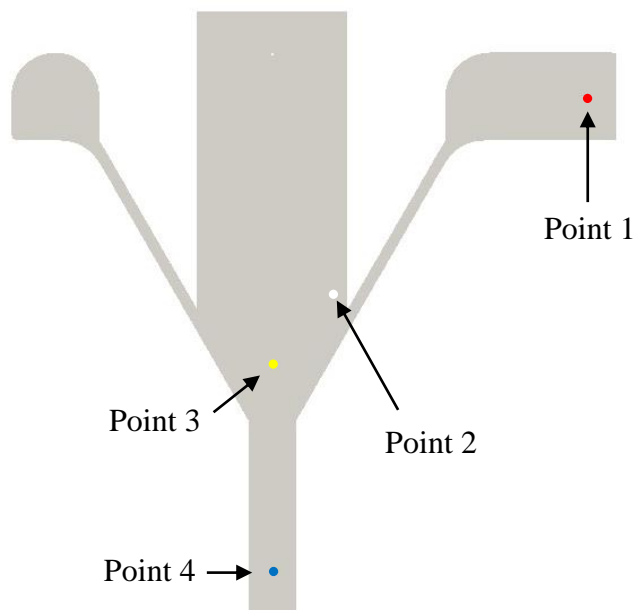


Figure 58 - Location of the four points of the domain used.

Table 20 - Evolution of the velocity and pressure values in four different points along the simulated time.

Time (s)	Point 1		Point 2		Point 3		Point 4	
	U (m/s)	P (MPa)	U (m/s)	P (MPa)	U (m/s)	P (MPa)	U (m/s)	P (MPa)
0	0	0	0	0	0	0	0	0
1	0.007	6.11	0.0021	2.31	0.033	2.2	0.121	0.41
2	0.007	6.12	0.0026	2.31	0.033	2.2	0.121	0.41
3	0.007	6.08	0.0028	2.3	0.032	2.2	0.121	0.41
4	0.007	6.07	0.0029	2.3	0.032	2.2	0.121	0.41
5	0.007	6.07	0.003	2.3	0.032	2.2	0.121	0.41
6	0.007	6.06	0.003	2.3	0.032	2.2	0.121	0.41
7	0.007	6.08	0.003	2.3	0.032	2.2	0.121	0.41
8	0.007	6.1	0.003	2.3	0.032	2.2	0.121	0.41
9	0.007	6.07	0.003	2.3	0.032	2.2	0.121	0.41

Analysing the values given in Table 20, it is possible to conclude that the pressure in Point 1 presents small variations, the pressure and the velocity in Point 2 stabilize after circa 3 and circa 5 s, respectively, and the velocity in Point 3 stabilizes after circa 3 s, being the remaining values very stable. Considering these results, it is possible to conclude that to achieve fully developed conditions the simulation should cover up to 5 s of the process evolution (since the variations of pressure in Point 1 are very small and they were neglected).

Figures 59 and 60 present the phase distribution at four different times each. A visual analysis these results allows to conclude that after approximately 4.5 s steady state flow conditions are achieved, which further reinforces the results presented before.

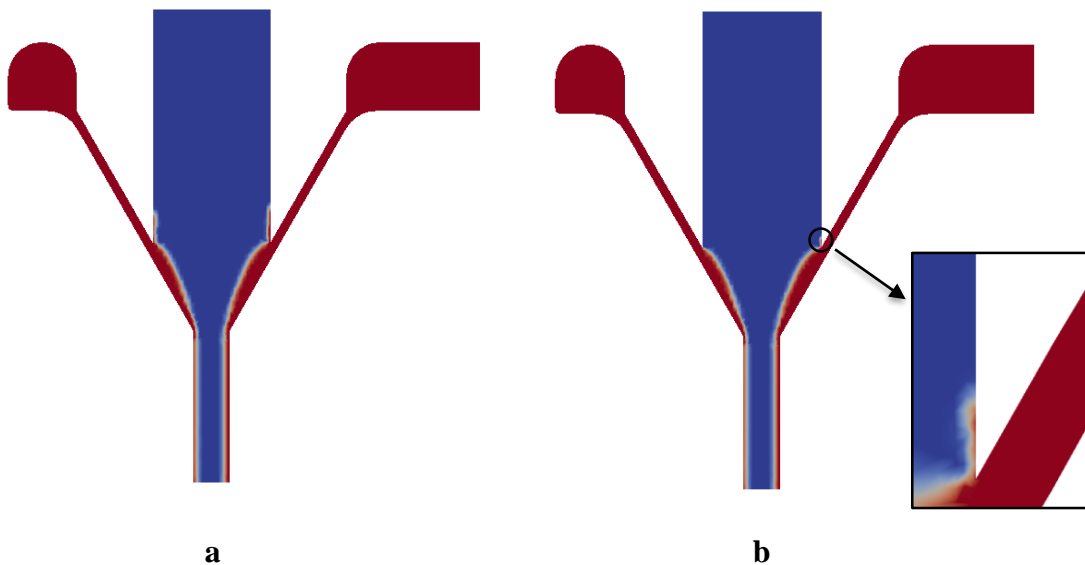


Figure 59 - Representation of the undeveloped flow at: (a) 1 second and (b) 4 seconds.

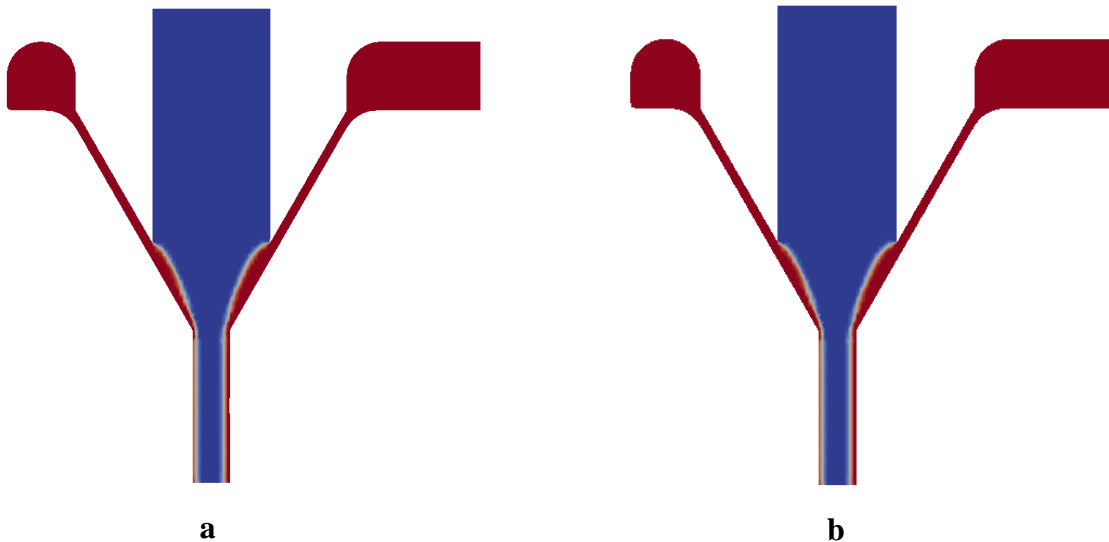


Figure 60 - Representation of the developed flow at: (a) 4.5 second and (b) 6 seconds.

The conclusions of these studies were employed just for the case studies used to select the most adequate convergent angle and for the case studies with different total and relative flowrates (with the boundary conditions stated in Table 19), where the system evolution was studied just up to 6 s. For the remaining, studies that were performed initially, the system evolution was computed up to 9 s.

Dimensioning of the channels and distributors

In relation to the measures and geometry of the channels and distributors, several iterations were done in order to achieve a solution that produces a stable flow without instabilities. In the first iteration, the diameters values of the channel were settled with values that according with the previous experience seemed reasonable (3 mm for the core channels and 1.8 mm for the sheath channels), and the geometry of the distributor was kept circular and symmetric. In this solution the flow presented instabilities and there was an undesired rearrangement of the sheath and core materials, caused by an unbalanced flow in the distributor, as it is shown in the flow distribution presented in Figure 61.

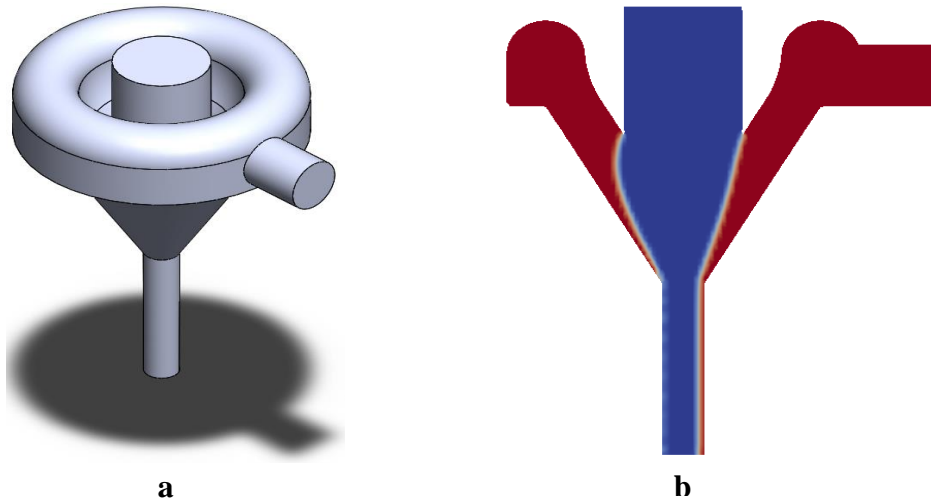


Figure 61 - Distributor created in the first iteration: geometry (a) and flow of the blends in the distributor (b).

In the following eleven iterations, the geometry of the distributor was changed in each iteration in order to attempt to compensate the unbalanced flow detected in the initial solution, which had a deficit of flow on the opposite site to the inlet 2, thus attempting to reach a stable solution, free of flow instabilities. In all the attempts, the flow presented the same problems as in the first iterations but the layer rearrangement was reduced, as Figure 62 shows.

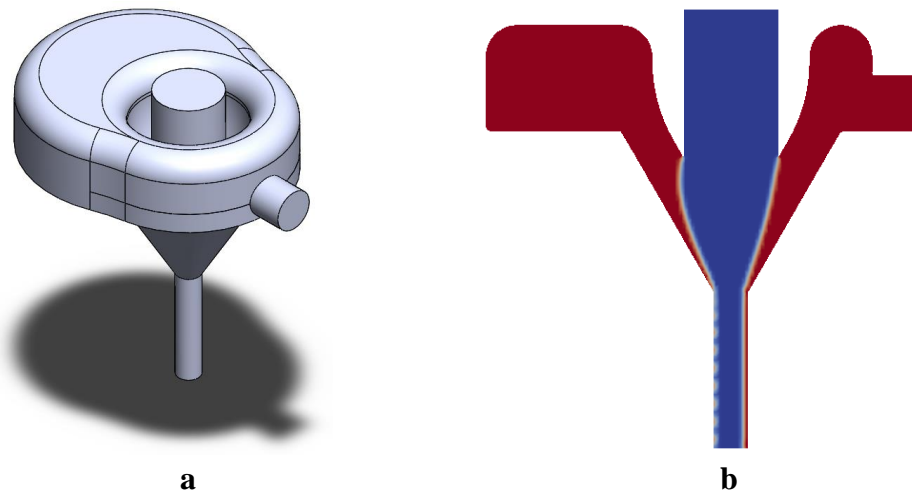


Figure 62 - Distributor created in the sixth iteration: geometry (a) and flow of the blends in the distributor (b).

Another approach was followed, and it consisted in trying to match the areas of the channels according to the relative proportion of the blend that passes through them (the proportions are the same as the Reference case presented in Table 19). Firstly, the diameter of the channel where the Blend B enters was defined and is equal to 11 mm. Then with that value the respective cross section area was calculated. Using the value of the previous area, the area of the channel that transports the Blend A is calculated through

the relative percentages of the materials presented in the filament as represented in Equation 17. With that area value it is possible to determine the value of the diameter of those channels, which is 6.4 *mm*.

$$A_{blend A channel} = \frac{A_{blend B channel}}{\%_{blend B}} * \%_{blend A} \quad (17)$$

To obtain the diameters of the branch channels of each blend, the respective area was divided by ten (because the main channel gives rise to 10 branch channels), and then with that value through the expression of the area of the circle it was possible to determine the diameter of the two types of branch channels. In Table 21, all the diameters of the channels for each blend are summarized.

Table 21 - Diameters and areas of the channels for each blend.

	Blend A	Blend B
Diameter of the main channel (<i>mm</i>)	6.4	11
Cross section area of the main channel(<i>mm</i>²)	32.53	95.03
Cross section area of the branch channel(<i>mm</i>²)	3.253	9.503
Diameter of the branch channel (<i>mm</i>)	2.04	3.48

After the dimensioning of the channels it is necessary to dimension the distributors. To accomplish that, the cross section area of the two types of branch channels were summed in order to discover the total area of material at the distributor. With that total area, through the expression of the area of the circle, it was possible to determine the diameter of the channel when the two blends are joined. Subtracting that value from the diameter of the branch channel for Blend B it is possible to determine the distance between the branch channel and the distributor wall, which is equal to 0.3 *mm*. In Figure 63 is possible to observe a scheme of the distributor, where the distance calculated before is represented by *x*.

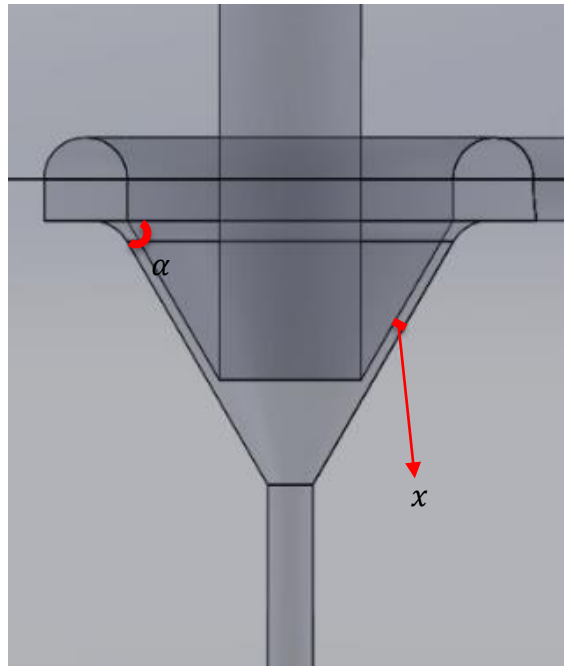


Figure 63 - Representation of the distributor used in the design of the die

With this approach a stable solution was accomplished, where the layer rearrangement was improved significantly, as it can be observed in Figure 64.

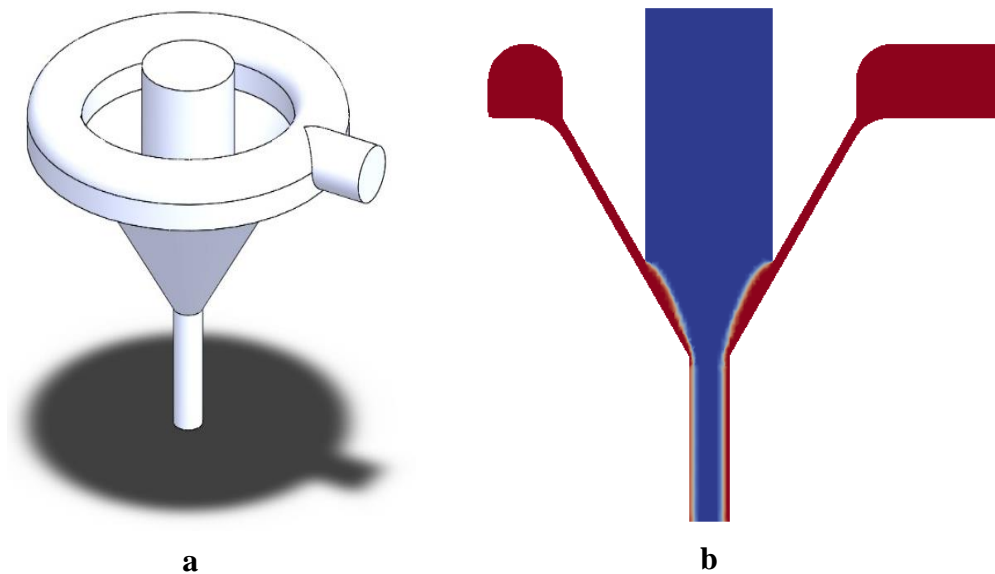


Figure 64 - Distributor created in the last iteration: geometry (a) and flow of the materials in the distributor (b).

Regarding the angle α presented in Figure 63, defined between the distributor convergent channel and the outlet channel, two typical values for that angle, 60° and 70° were considered. The chosen value of that angle will be the one that enables the production of a filament with an interface between the two materials as stable and centred as possible and with the smallest pressure drop. Thus, the efficiency of both angles was measured through the interface location between the two materials at the die exit (outlet)

and through the pressure drop obtained in the two cases. For the studied geometries the pressure drop in the distributor is mainly affected by two factors, which are the length of the channel and the extensional deformation rate, both promoting a larger pressure drop when enlarged. Since the distributor with an angle of 60° possess a smaller length of the channel and a higher extensional deformation rate than the distributor with an angle of 70° , it is not possible to anticipate which alternative promotes the smallest pressure drop, thus their effect was studied numerically.

Figures 65 and 66 present the location of the interface between the two materials and the pressure distribution obtained for the two alternative designs, respectively.

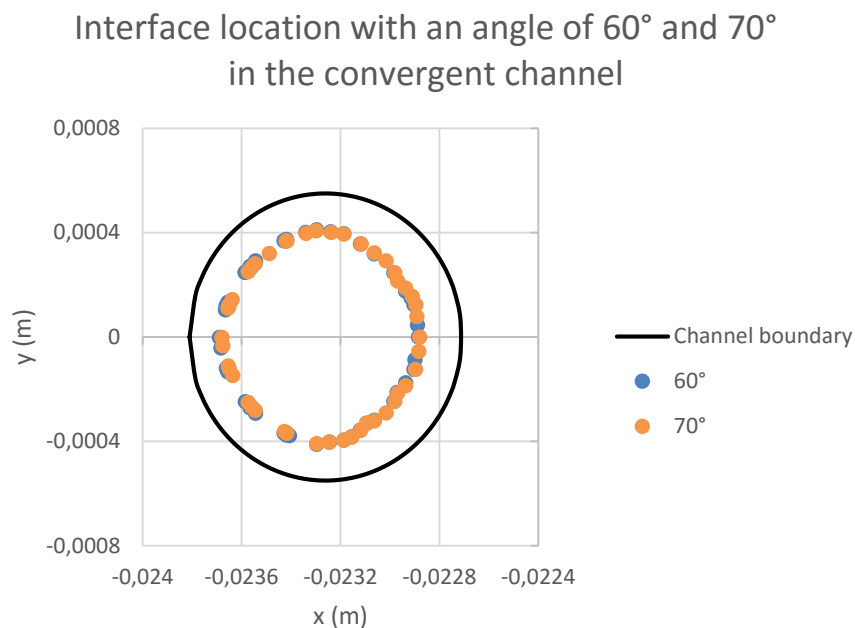


Figure 65 - Interface location with an angle of 60° and 70° in the convergent channel of the die.

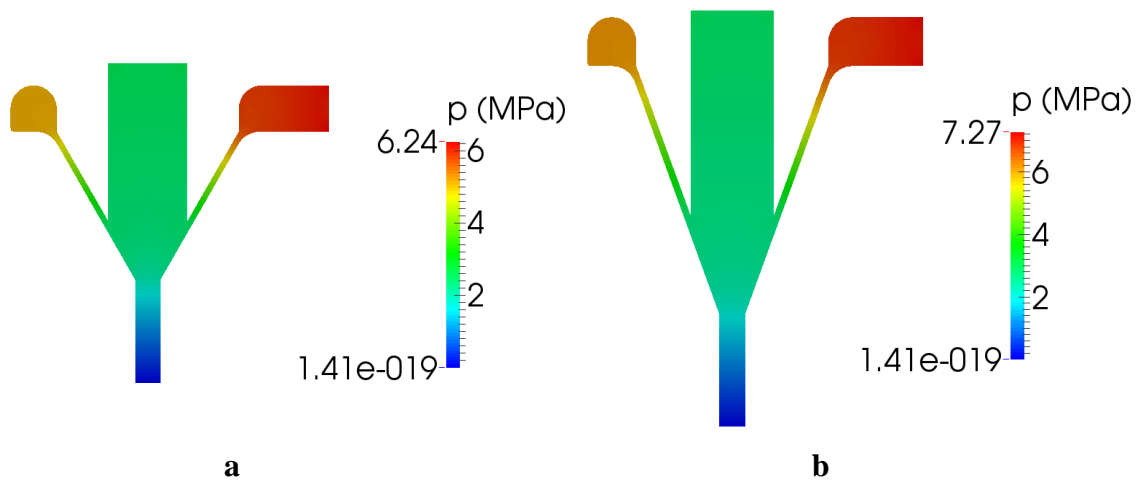


Figure 66 - Pressure drop in the two distributors in study: (a) with an angle of 60° and (b) with an angle of 70° in the convergent channel.

Analysing Figure 65 it is possible to conclude that there is no major difference between a convergent channel with an angle of 60° or 70°, because the data points for 70° are almost identical to the data points for 60°. Regarding the pressure drop, it is possible to conclude that the pressure drop is smaller in the distributor with an angle of 60°, which means that the effect of the channel length prevails over the one of the extensional deformation rate. Therefore, the distributor with the 60° angle was select for the tool to be designed. As an additional advantage, this geometry requires a smaller quantity of computational cells and, thus, less computational time.

But before this design is approved to run the remaining simulations, it was computed the shear rates (using Equations 18 and 19) and the respective shear stresses (using the rheological models of the blends) developed in each channel of the system using all the different processing conditions defined in Table 19, in order to verify if these values were not higher than the limit of the material can stand, thus overcoming the critical shear stress of the material. Equations 18 and 19 represent the shear rate in a circular channel and in an annular channel (used to calculated the shear rate in the distributor), respectively (Carneiro & Nóbrega, 2012), and in Table 22 are presented the shear rates and shear stresses computed.

$$\dot{\gamma} = \frac{4Q}{\pi R^3} \frac{3n + 1}{4n} \quad (18)$$

where $\dot{\gamma}$ (s^{-1}) is the shear rate, Q (m^3/s) is the flow rate, R (m) is the radius of the channels and n is the Power Law index.

$$\dot{\gamma} = \frac{6Q}{\pi(R_e + R_i)(R_e - R_i)^2} \frac{2n + 1}{3n} \quad (19)$$

where R_e (m) is the external radius of the channels and R_i (m) is the internal radius of the channels.

Table 22 - Shear rates and shear stresses developed in each of channel in all the processing conditions considered.

	Reference		Case 1		Case 2		Case 3		Case 4		Case 5	
	$\dot{\gamma}$ (s^{-1})	τ (MPa)	$\dot{\gamma}$ (s^{-1})	τ (MPa)	$\dot{\gamma}$ (s^{-1})	τ (MPa)	$\dot{\gamma}$ (s^{-1})	τ (MPa)	$\dot{\gamma}$ (s^{-1})	τ (MPa)	$\dot{\gamma}$ (s^{-1})	τ (MPa)
Core main channel	6.4	0.02	4.8	0.018	7.8	0.021	6.9	0.021	6.1	0.02	5.2	0.019
Sheath main channel	12.9	0.045	9.7	0.042	5.1	0.035	10.2	0.042	15.2	0.047	20.3	0.05
Core branch channel	20.4	0.029	15.3	0.027	24.6	0.031	21.9	0.03	19.1	0.029	16.4	0.027
Sheath branch channel	39.9	0.059	30	0.055	15.7	0.047	31.3	0.055	47	0.061	62.7	0.065
Parallel zone	1014.5	0.123	760.9	0.115	1017.6	0.123	1015.6	0.123	1013.6	0.123	1011.5	0.123
Distributor	215.3	0.086	161.5	0.081	84.4	0.07	168.9	0.082	253.3	0.09	337.7	0.096

Analysing the values presented in Table 22, it can be noticed that the highest shear rates develop in the parallel zone of the die, leading to shear stresses of circa 0.12 MPa (computed using the rheological model of Blend A). As explained by Macosko (Macosko, 1994), the typical critical shear stress of the polymeric materials is 0.1 MPa, so it is possible to conclude that the die is operating in the limit of the material. However, since the diameter of this channel cannot be changed, the only way to fix this potential problem is to decrease the mass flow rate used. So, it will be performed a study to assess if the decrease in the flow rate used affects the process stability and the filament produced.

Effect of the mass flow rate used on the filaments produced

Regarding the simulations using different mass flow rates, an approach similar to the one described in Section 3 was followed. The interface points obtained from the simulation were fitted using Excel to an ellipse equation (Equation 15) and to a circumference equation, presented in Equation 20, in order to evaluate the eccentricity and the centre of the filament interface.

$$(x - c)^2 + (y - d)^2 = r^2 \quad (20)$$

where c and d are the coordinates of the circumference centre and r is the radius.

In Figures 67 and 68 it is possible to observe the graphical representation of the interface points and the ellipse and circumference equations for the Reference case and for Case 1, respectively, and in Table 23 are listed the constants of the two equations for both cases.

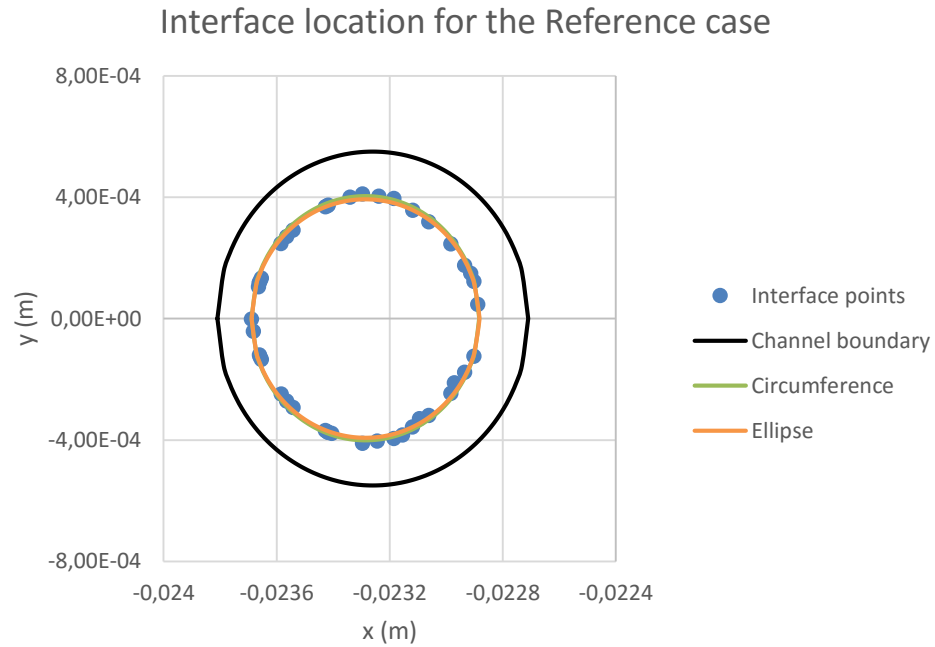


Figure 67 - Interface location and graphical representation of the equations for the Reference case.

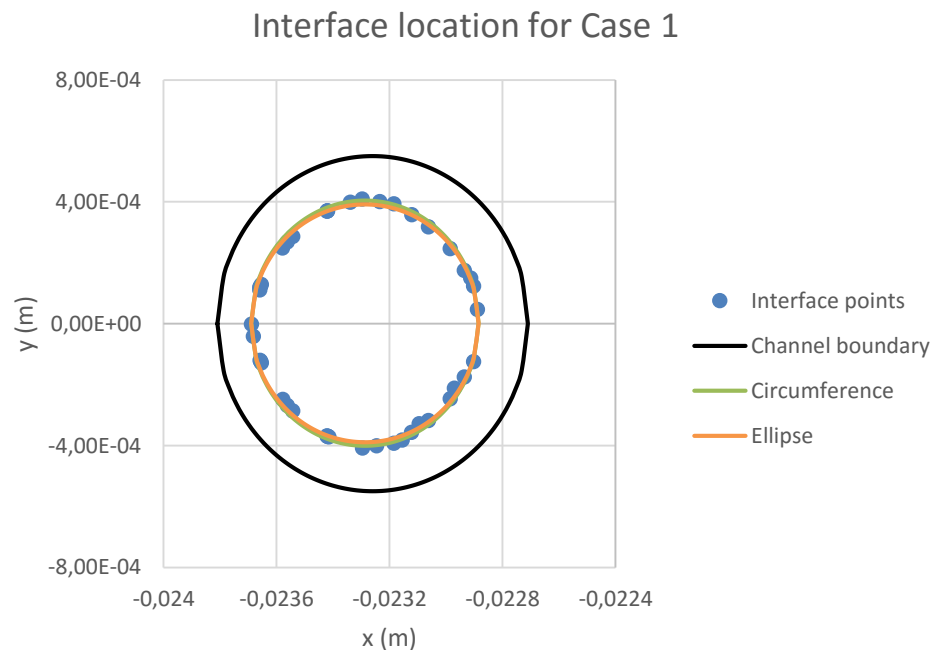


Figure 68 - Interface location and graphical representation of the equations for Case 1.

Table 23 - Constants of the ellipse and the circumference equations for the Reference case and for Case 1.

	Reference	Case 1
<i>h</i> (mm)	-23.29	-23.29
<i>k</i> (mm)	$7.85 * 10^{-4}$	$1.21 * 10^{-3}$
<i>a</i> (mm)	0.4	0.4
<i>b</i> (mm)	0.39	0.39
<i>c</i> (mm)	-23.29	-23.29
<i>d</i> (mm)	$1.66 * 10^{-3}$	$1.61 * 10^{-3}$
<i>r</i> (mm)	0.4	0.4

According to Figures 67 and 68 and Table 23, both cases produce very similar results as the constants of the equations are almost identical in the two cases. In both cases the interface is a little bit off centre comparing with regards to the channel centre (which is x equals to -23.26 mm and y equals to 0 mm) as it can be noticed through the thickness of the sheath layer which is not constant.

In terms of eccentricity, through the analysis of the ellipse constants equation it is possible to conclude that the interface has a small eccentricity, however that eccentricity is not very noticeable at the figures and can only be distinguished due to the difference between the two semi axis of the ellipse (the a and b constants). Applying Equation 16 the eccentricity (e) of the interface has a value of 0.22 for the Reference case and 0.24 for Case 1, which are almost identical.

To evaluate the quality of the produced filament, its minimum and maximum sheath thickness was also measured, and the values obtained are listed in Table 24 for the two studied cases.

Table 24 - Minimum and maximum sheath thickness of the filament for the Reference case and for Case 1.

	Reference	Case 1
Minimum thickness of the sheath (mm)	0.12	0.12
Maximum thickness of the sheath (mm)	0.19	0.19

As it could be seen in Table 24 the minimum and the maximum sheath thickness are equal in both cases. When these values are compared with the circumference radius in the interface, the minimum thickness is 18% smaller than the radius and the maximum thickness is 30% bigger than the radius.

Another parameter that was evaluated was the cylindricity of the filament interface, which gives an idea of the tolerance of the interface location. To assess that, the interface locations along the die parallel zone (the channel between the convergent channel and the die exit) were obtained and then the distance to the centre of the interface was computed. After that, the smallest and the highest values obtained were chosen and corresponded to the tolerance of the radius of two hypothetic cylinders where the interface has to be included between them. In Table 25 are listed the tolerances obtained for the interface location for both cases.

Table 25 - Minimum and maximum tolerance (radius) of the interface location in Reference case and Case 1.

	Reference	Case 1
Minimum radius (mm)	0.38	0.38
Maximum radius (mm)	0.42	0.42

Analysing the values presented in Table 25, it is possible to determine that the interface has to be contained between two cylinders with 0.42 mm and 0.38 mm in radius for both cases.

Regarding the velocity and pressure profiles for the two cases, attending to the fact that different mass flow rates were used, the velocity at the die exit and the pressure drop have slightly different values for each case, wherein the Reference case present the higher values. Figures 69 and 70 represents, respectively, the velocity profile and the pressure drop along the distributor in the Reference case and Figures 71 and 72, the velocity profile and the pressure drop in Case 1.

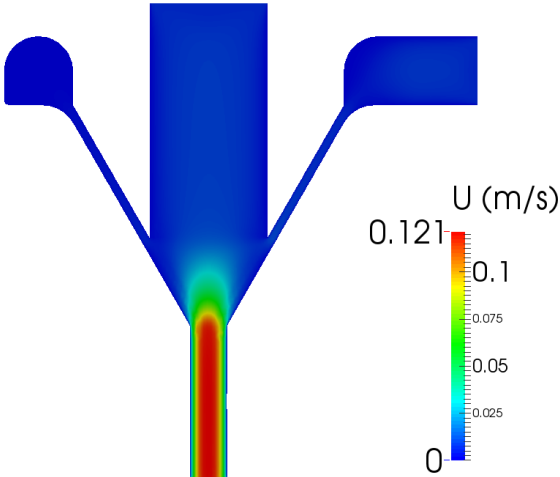


Figure 69 - Velocity profile along the distributor in the Reference case.

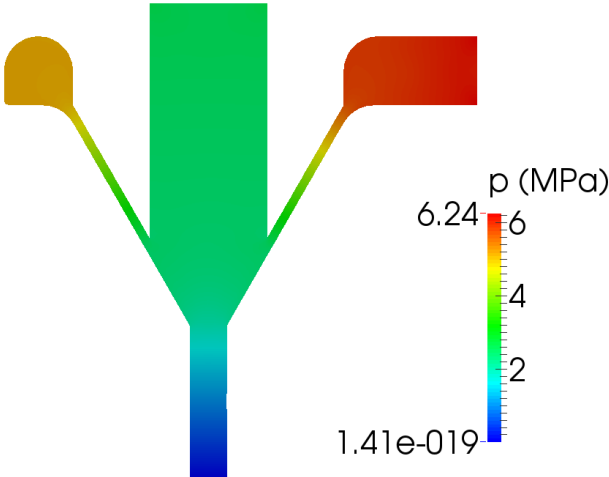


Figure 70 - Pressure field along the distributor in the Reference case.

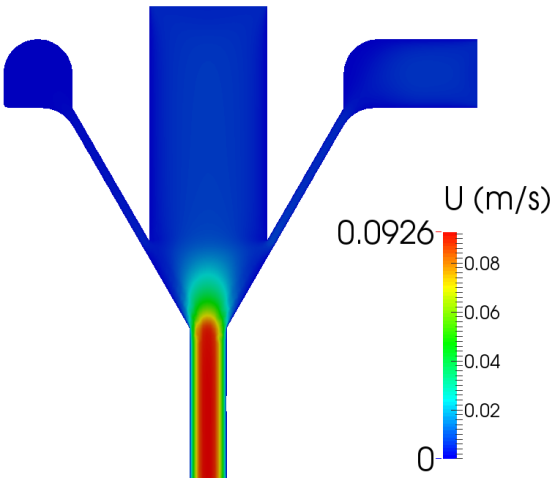


Figure 71 - Velocity profile along the distributor in Case 1.

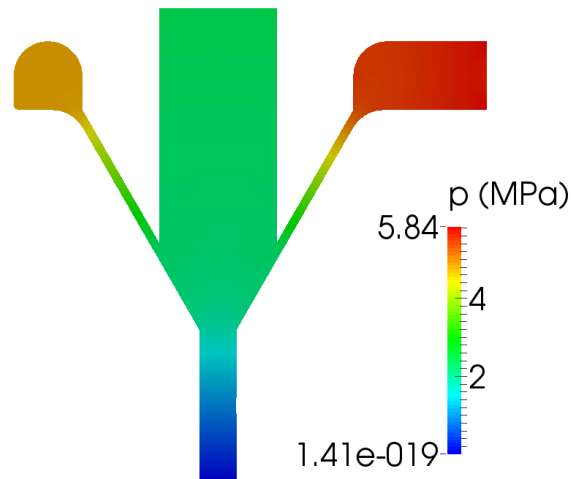


Figure 72 - Pressure field along the distributor in Case 1.

Through the analyses of the previous figures, it is possible to conclude that for both cases studied the velocity profile presents an acceleration of the material at the die parallel zone, due to the small channel diameter and before that the velocity is much smaller than the one developed in the parallel zone. Regarding the pressure field, it is possible to conclude that the pressure decreases smoothly and monotonically along the flow channel. Therefore, no potential problems were identified in the velocity field and in the pressure drop of the die that could cause instabilities in the coextrusion process.

Attending to all the results obtained it is possible to conclude that reducing the mass flow rate used, there is no big impact in the stability of the process and the filaments produced will be similar. So, as stated above the shear rates developed in the parallel zone may affect the quality of the filament, therefore if in the experimental trials the filaments present defects the mass flow rate used can be reduced, without affect the performance of the die, in order to fix these defects.

Effect of blend percentage on the filaments produced

Regarding the simulations using different percentages of blends, only Case 2 shows a severe layer rearrangement, motivated by the higher proportion of core in relation to the sheath. That phenomenon appear in the die parallel zone and it is characterized by a rupture of the interface, as it can be observed in Figure 73.

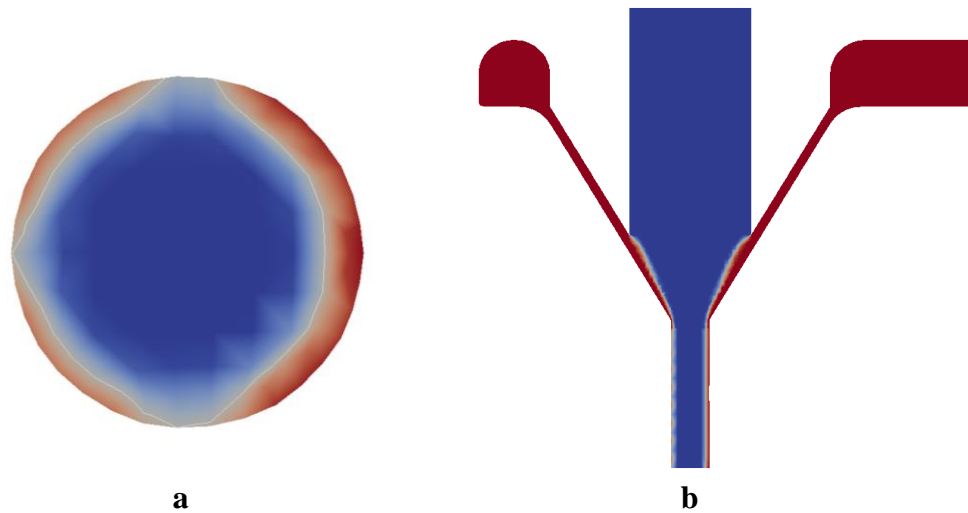


Figure 73 - Interface location in Case 2: (a) rupture of the interface and (b) instabilities in the die parallel zone.

Therefore, only Cases 3, 4 and 5 will be subjected to an analysis equal to the one performed for the cases with different mass flow rates. Thus, following the same methodology, the interface points were fitted to an ellipse equation (Equation 15) and to a circumference equation (Equation 18). In Figures 74, 75 and 76 show the graphical representation of the interface points and the equations for all the cases, and in Table 26 are listed the constants of the two equations for all the same cases.

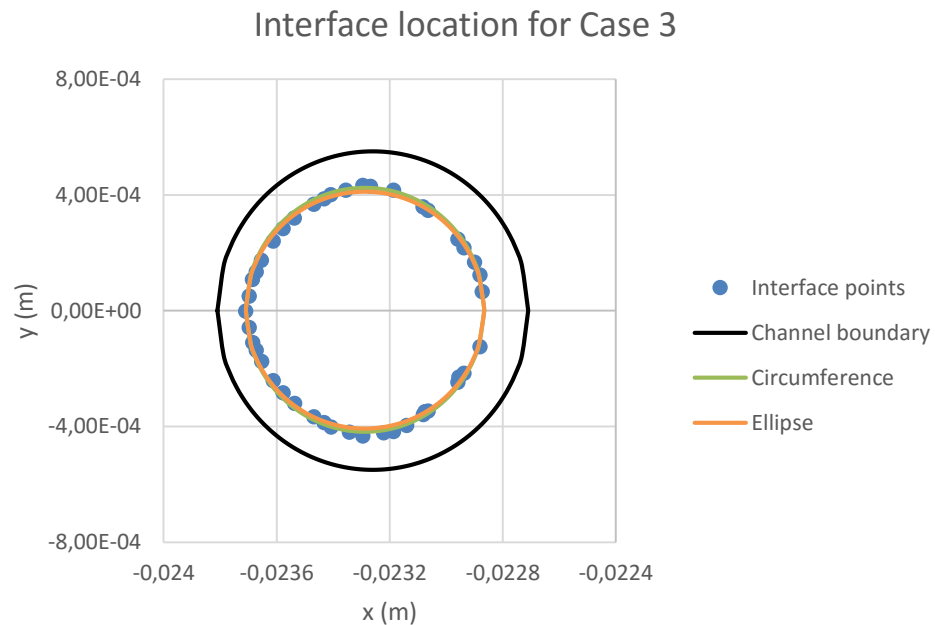


Figure 74 - Interface location and graphical representation of the equations for Case 3.

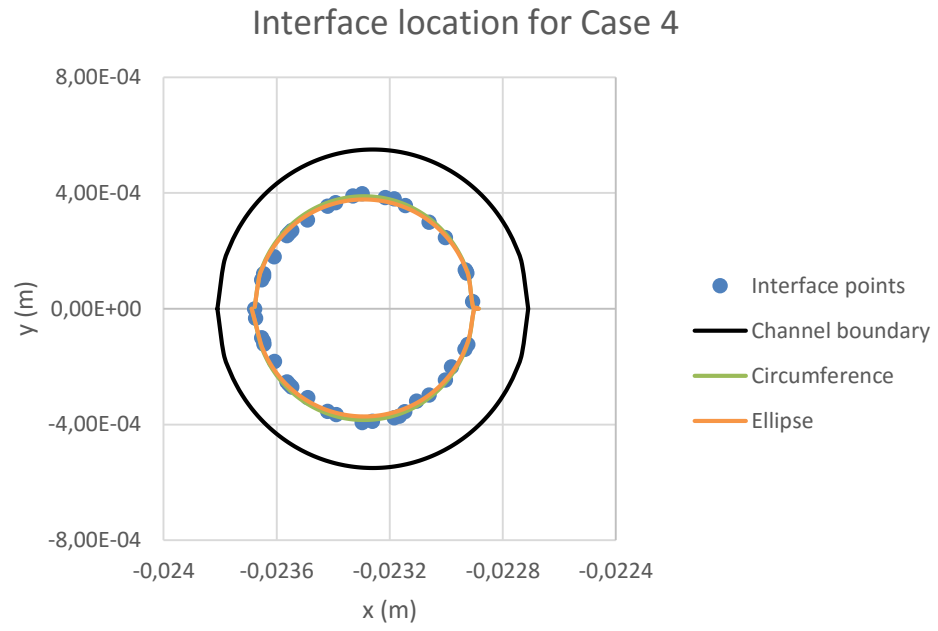


Figure 75 - Interface location and graphical representation of the equations for Case 4.

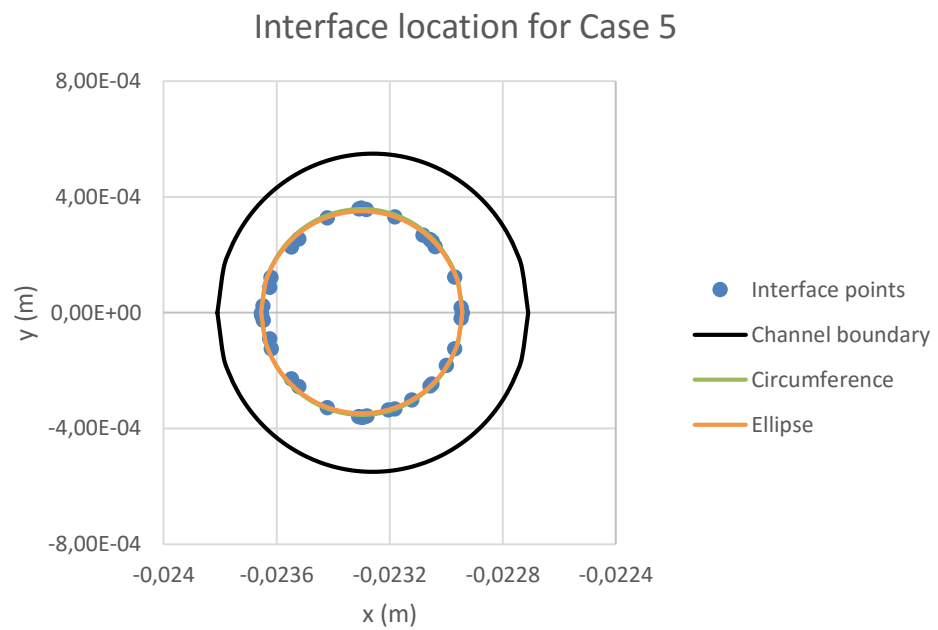


Figure 76 - Interface location and graphical representation of the equations for Case 5.

Table 26 - Constants for the ellipse and circumference equations for Cases 3, 4, and 5.

	Case 3	Case 4	Case 5
<i>h</i> (mm)	-23.29	-23.29	-23.3
<i>k</i> (mm)	$1.78 * 10^{-3}$	$2.55 * 10^{-3}$	$1.35 * 10^{-3}$
<i>a</i> (mm)	0.42	0.39	0.36
<i>b</i> (mm)	0.41	0.38	0.35
<i>c</i> (mm)	-23.29	-23.29	-23.3
<i>d</i> (mm)	$2.89 * 10^{-3}$	$1.98 * 10^{-3}$	$1.98 * 10^{-3}$
<i>r</i> (mm)	0.42	0.39	0.36

Just like in the previous two cases, in all the simulated cases the interface is slightly off centre with regards to channel centre. Regarding the axis values of the ellipse and the circumference, analysing Table 26 it is possible to observe that these values are decreasing from Case 3 to Case 5, motivated by the increase of the percentage of sheath material used in the composition of the filament.

In terms of eccentricity, through the analyses of the ellipse equation constants it is possible to conclude that the interface possesses a very small eccentricity. Like in the Reference case and in Case 1, the eccentricity is not very noticeable at the figures and only can be distinguished due to the difference between the two semi axis of the ellipse (the *a* and *b* constants). Through Equation 16 is possible to compute the eccentricity (*e*) of the interface and the values obtained were 0.22 for Case 3 and 4 and 0.23 for Case 5, being the values obtained very similar, as in the previous studies.

With regards to the thickness of the sheath, in Table 27 are listed the minimum and the maximum distances of the interface points to the channel boundary, corresponding to the minimum and the maximum thickness of the filament sheath for Cases 3, 4 and 5.

Table 27 - Minimum and maximum thickness of the filament sheath for Cases 3, 4 and 5.

	Case 3	Case 4	Case 5
Minimum thickness of the sheath (mm)	0.10	0.13	0.16
Maximum thickness of the sheath (mm)	0.17	0.21	0.24

From the results of Table 27, it is possible to conclude that both the minimum and the maximum thickness of the sheath are increasing, wherein Case 3 has the smallest values and Case 5 has the highest values, which can be explained through the percentages of each blend in the filament for each case study. Comparing the interface circumference radius (last line of Table 26) with the thickness values presented in Table 27, it can be concluded that the minimum thickness is 22%, 19% and 20% smaller and the maximum thickness is 31%, 26% and 22% larger than the radius value for Cases 3, 4 and 5 respectively.

Finally, the interface cylindricity of the filament, which gives an idea of the tolerance of the interface location, was computed, being the results shown in Table 28.

Table 28 - Minimum and maximum tolerance (radius) of the interface location in Cases 3, 4 and 5.

	Case 3	Case 4	Case 5
Minimum radius (mm)	0.4	0.37	0.33
Maximum radius (mm)	0.44	0.4	0.37

Analysing the values presented in Table 28, it is possible to conclude that the tolerance values are more or less constant, the minimum and maximum values are decreasing from Case 3 to Case 5, due to the increase of the percentage of the Blend A in the filament, which increases the thickness of the external layer, thus reducing the radius of the interface.

The velocity field and the pressure drop in all the three cases are very similar to each other and to the same result computed for the Reference case presented in Figures 69 and 70. In Appendix D are included the velocity field and the pressure fields for Cases 3, 4 and 5.

Considering the results obtained it is possible to conclude that the coextrusion die may be used to produce filaments in a range of formulations between Case 3 (20% of Blend A and 80% of Blend B) and Case 5 (40% of Blend A and 60% of Blend B) without instabilities in the process and the filaments fulfil all the requirements.

Attending to the results described during this section, it was established that the die designed meets the requirements imposed by the company, thus it can be manufactured. So in order to do that, the technical drawings of all the components of the die, which are required to help the manufacture process of the die, were made. These technical drawings are presented in Appendix E.

5. CONCLUSIONS AND FUTURE WORK

5.1 Conclusions

The work presented in this MSc Thesis had as main objective the design of a coextrusion system (die) for the production of multifunctional filaments, capable of producing simultaneously 10 filaments with different filament formulations.

To achieve the main objective described in the last paragraph the OpenFOAM[®] framework was firstly used on a few verification/assessment cases studies, in order to evaluate the accuracy of the calculations.

The first validation case consisted in the simulation of a 2D sheet coextrusion die, being the numerical predictions compared to results available on the literature. Regarding the interface development and the flow streamlines, two of the three cases studied were in agreement with the results presented in the literature, while the results for the third case presented an average error higher than the other two cases, which can be justified by an eventual error in the benchmark paper used to compare our results. In addition, the results provided by the two different meshing methodologies, using *cfMesh* and *blockMesh* utilities were very similar.

The second and the third assessment case studies consisted in comparing the computational predictions with data collected in experimental studies of monofilament extrusion and coextrusion. The comparison was made in terms of pressure drop and the interface shape of the coextruded filaments, being the results obtained in these assessment case studies allowed to conclude that OpenFOAM[®] is suitable to model the extrusion/coextrusion process and thus able to support in the design of processing tools.

Concerning the design of the filament coextrusion die, the devised die flow channel constructive solution was studied and detailed with the support of the open source computational library OpenFOAM[®], which was used to simulate the flow of the blends (which compose the filaments) in the die channels. Thus, it was possible to observe if any instabilities in the flow were present, if the flow is balanced and if the die manage to produce sheath and core filaments as centred as possible.

In terms of design of the channels, initially two possible constructive solutions were considered, but ultimately it was selected the solution that promotes a uniform distribution of the flow before enter the distributor, wherein the sheath and core filament is formed. The channels of that solution were dimensioned using the simulations provided by the OpenFOAM[®], in order achieve a solution that allow the production of filaments with the required specifications.

The ability of the designed die to produce filaments at different mass flow rates and with different percentages of sheath and core were also tested. Regarding the simulations with different mass flow rates, the results showed that there is no major difference in using different mass flow rates, once the filaments produced have very similar characteristics. Concerning the ability of the die to produce filaments with different percentages of sheath and core, the results achieved suggested that the die can be used to produce filaments ranging from 20% of sheath and 80% of core to 40% of sheath and 60% of core.

5.2 Future work

During this MSc project it was assessed and confirmed the ability of the computational library OpenFOAM[®] in simulate the filament coextrusion process, which enabled the design of semi-industrial filament coextrusion die.

From the promising results achieved in this project, it is suggested to advance with the designed die manufacturing and experimental testing, which would further assess the computational library employed in this kind of applications.

If the results of the experimental trials suggested that the filaments produced are in accordance with the company expectations and standards, and if the production of filaments with this technology is profitable, then the process can be scaled to an industrial level (manufacturing and using a die capable of develop high production rates).

BIBLIOGRAPHIC REFERENCES

- Abreu, A. (To be published). *Coextrusion of multifuncional fibres*. MSc thesis, Universidade do Minho, Departamento de Engenharia de Polímeros, Guimarães.
- Agassant, J.-F., Arda, D. R., Combeaud, C., Merten, A., Münstedt, H., Mackley, M. R., . . . Vergnes, B. (2006). Polymer Processing Extrusion Instabilities and Methods for their Elimination or Minimisation. *International Polymer Processing*, 21(3), 239-255.
- Andersson, J. (2011). *Simulation of Wave Induced Forces on Semi Submerged Horizontal Cylinders Using OpenFOAM®*. MSc thesis, Chalmers University of Technology, Department of Shipping and Marine Technology , Göteborg.
- Carneiro, O. S., & Nóbrega, J. M. (2012). Main Issues in the Design of Extrusion Tools. In O. S. Carneiro, & J. M. Nóbrega, *Design of Extrusion Forming Tools* (p. 292). Smithers Rapra Technology Ltd.
- Dooley, J. (2002). *Viscoelastic flow effects in multilayer polymer coextrusion*. PhD thesis, Technische Universiteit Eindhoven, Eindhoven.
- Dugan, J. S. (2010, July 19). *Specialty Markets - Bicomponent Fibers*. Retrieved March 2, 2016, from Textile World: <http://www.textileworld.com/textile-world/nonwovens-technical-textiles/2010/07/specialty-markets-bicomponent-fibers/>
- Ferreira, A., Costa, P., Carvalho, H., Nobrega, J. M., Sencadas, V., & Lanceros-Mendez, S. (2011). Extrusion of poly(vinylidene fluoride) filaments: effect of the processing conditions and conductive inner core on the electroactive phase content and mechanical properties. *Journal of Polymer Research*, 18(6), 1653–1658.
- Giles, H. F., Wagner, J. R., & Mount, E. M. (2004). *Extrusion: The Definitive Processing Guide and Handbook*. William Andrew Publishing.
- Glauß, B., Steinmann, W., Walter, S., Beckers, M., Seide, G., Gries, T., & Roth, G. (2013). Spinnability and Characteristics of Polyvinylidene Fluoride (PVDF)-based Bicomponent Fibers with a Carbon Nanotube (CNT) Modified Polypropylene Core for Piezoelectric Applications. *Materials*, 6, 2642-2661.

- Gonçalves, N. D. (2013). *Computer Aided Design of Extrusion Forming Tools for Complex Geometry Profiles*. PhD thesis, Universidade do Minho, Departamento de Engenharia de Polímeros, Guimarães.
- Greenshields, C. J. (2015, December 13). *OpenFOAM - User Guide*. Retrieved from Sourceforge: <http://foam.sourceforge.net/docs/Guides-a4/UserGuide.pdf>
- Haider, J. (2013). *Numerical Modelling of Evaporation and Condensation Phenomena*. Universitat Stuttgart, Institut für Raumfahrtssysteme, Stuttgart.
- Hannachi, A., & Mitsoulis, E. (1993, September). Sheet Coextrusion of Polymer Solutions and Melts: Comparison between Simulation and Experiments. *Advances in Polymer Technology*, 12(3), 217-231.
- Henry. (2005, July 1). *Why sometimes momentum predictor step is not performed [Online forum comment]*. Retrieved August 18, 2016, from CFD Online: <http://www.cfd-online.com/Forums/openfoam-solving/60558-why-sometimes-momentum-predictor-step-not-performed.html>
- Herreras, N., & Izarra, J. (2013). *Two-Phase pipeflow simulations with OpenFoam*. Msc thesis, Norwegian University of Science and Technology, Department of Energy and Process Engineering, Trondheim.
- Juretić, F. (2015, May). *cfMesh - User Guide*. Retrieved March 5, 2016, from cfMesh: http://cfmesh.com/wp-content/uploads/2015/09/User_Guide-cfMesh_v1.1.pdf
- Kostic, M., & Reifschneider, L. (2006). Design of Extrusion Dies. *Encyclopedia of Chemical Processing*.
- Macosko, C. W. (1994). *Rheology: Principles, Measurements, and Applications*. Wiley-VCH.
- Martins, R. S., Gonçalves, R., Azevedo, T., Rocha, J. G., Nóbrega, J. M., Carvalho, H., & Lanceros-Mendez, S. (2014). Piezoelectric Coaxial Filaments Produced by Coextrusion of Poly(vinylidene fluoride) and Electrically Conductive Inner and Outer Layers. *Journal of Applied Polymer Science*, 131(17).
- Perdikoulis, J., Zatloukal, M., & Touré, B. (2004). The Application of Simulation in Co Extrusion Processes. *TAPPI PLACE Conference*, (pp. 743-749). Indianapolis.
- Rajkumar, A., Ferrás, L., Fernandes, C., Carneiro, O., M.Becker, & Nóbrega, J. (Accepted for publishing). Design guidelines to balance the flow distribution in complex profile extrusion dies. *International Polymer Processing*.
- Rauwendaal, C. (2014). *Polymer Extrusion* (5th ed.). Hanser Publications.

- Riquelme, A. T. (1995). *Finite Element Analyses of Layer Non-uniformity in Polymer Coextrusion Flows*. PhD thesis, McMaster University, Chemical Engineering, Hamilton.
- Schrenk, W., & Alfrey, T. (1978). Coextruded Multilayer Polymer Films and Sheets. In D. R. Paul, & S. Newman, *Polymer Blends*. New York: Academic Press.
- Stephens, D. (2016, January 4). *Deciding between Open Source and Proprietary CFD software*. Retrieved July 13, 2016, from Applied CCM: <https://www.appliedccm.com/deciding-between-open-source-and-proprietary-cfd-software/>
- Verhoeven, O. (2011). *Trailing Edge Noise Simulations using IDDES in OpenFOAM*. MSc thesis, Delft University of Technology, Faculty of Aerospace Engineering, Delft.
- Vlachopoulos, J., & Strutt, D. (2003). The Role of Rheology in Polymer Extrusion. *New Technology for Extrusion Conference*, (pp. 20-21). Milan.
- Wang, J., Langhe, D., Ponting, M., Wnek, G. E., Korley, L. T., & Baer, E. (2013). Manufacturing of polymer continuous nanofibers using a novel co-extrusion and multiplication technique. *Polymer*, 55(2), 673-685.
- Wuthrich, B. (2007). *Simulation and validation of compressible flow in nozzle geometries and validation of OpenFOAM for this application*. MSc thesis, Swiss Federal Institute of Technology Zurich, Institute of Fluid Dynamics, Zurich.

APPENDIXES

Appendix A – Developed flow in the more refined mesh created using *blockMesh*

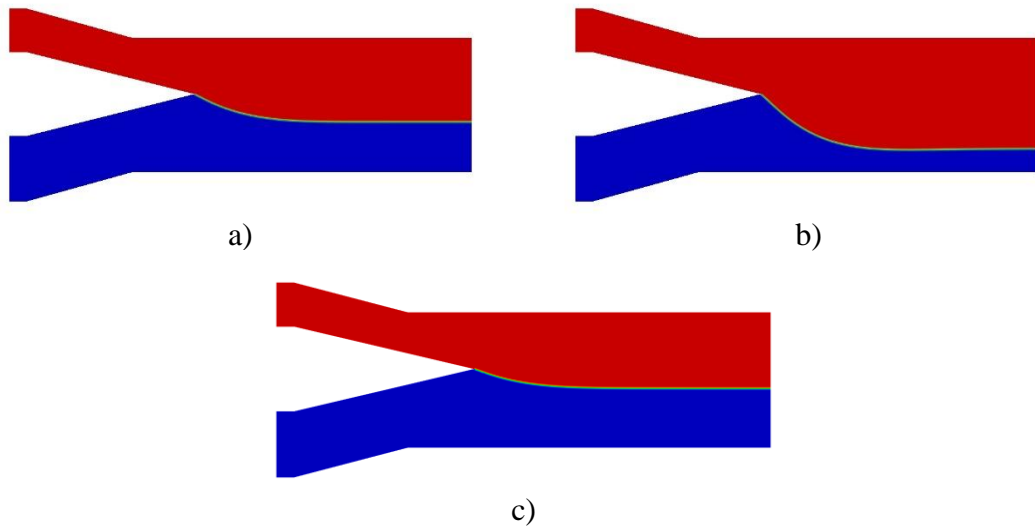


Figure 77 - Representation of the fully developed flow for the more refined mesh created using *blockMesh* in: a) Case 1; b) Case 2; c) Case 3.

Appendix B – Interface in cases with mesh created using *blockMesh*

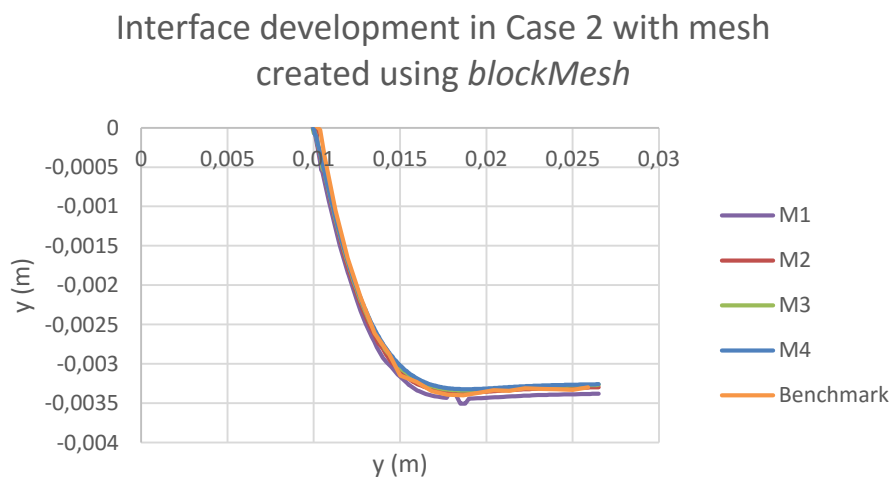


Figure 78 - Interface coordinates for Case 2 (mesh created using *blockMesh*).

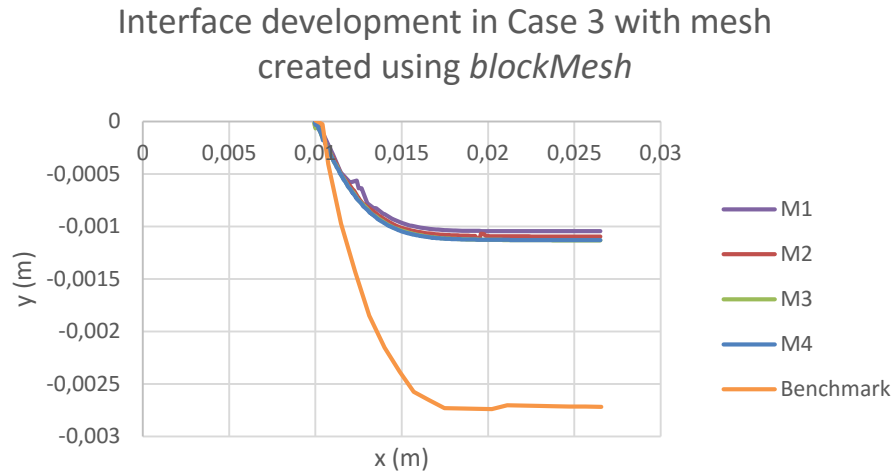


Figure 79 - Interface coordinates for Case 3 (mesh created using *blockMesh*).

Appendix C – Streamlines in cases with mesh created using *blockMesh*

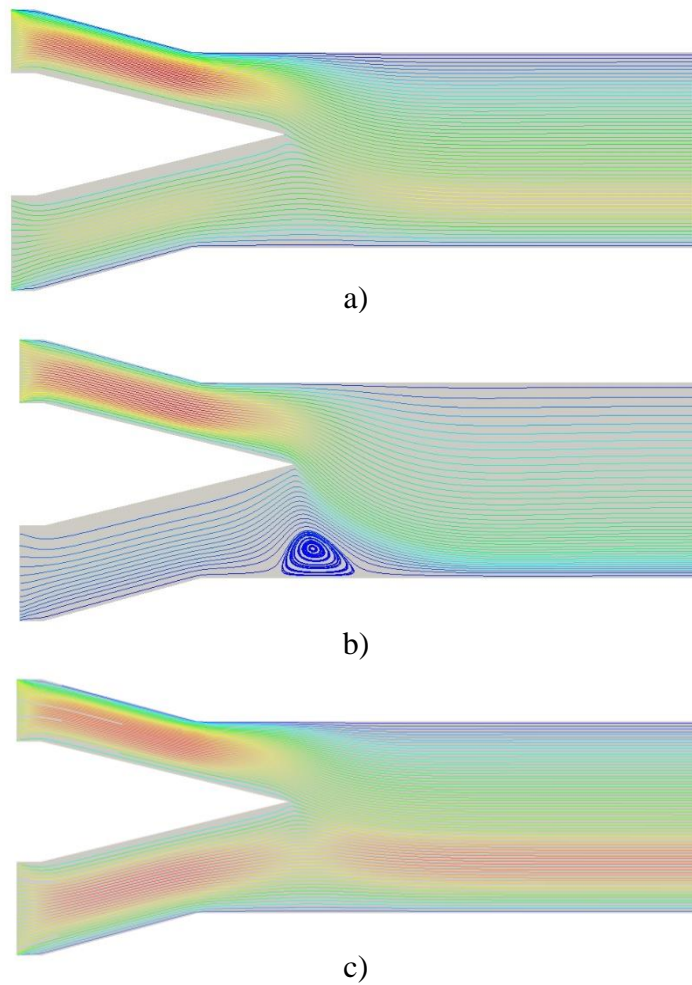


Figure 80 - Representation of the streamlines for the more refined mesh created using *blockMesh* in: a) Case 1; b) Case 2; c) Case 3.

Appendix D – Velocity profile and pressure field in Cases 3, 4 and 5

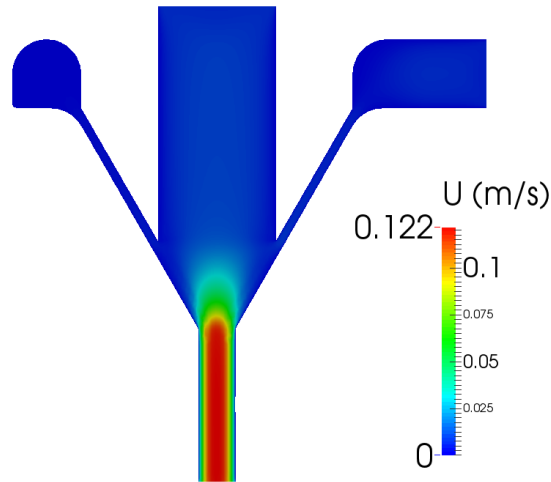


Figure 81 - Velocity profile along the distributor in Case 3.

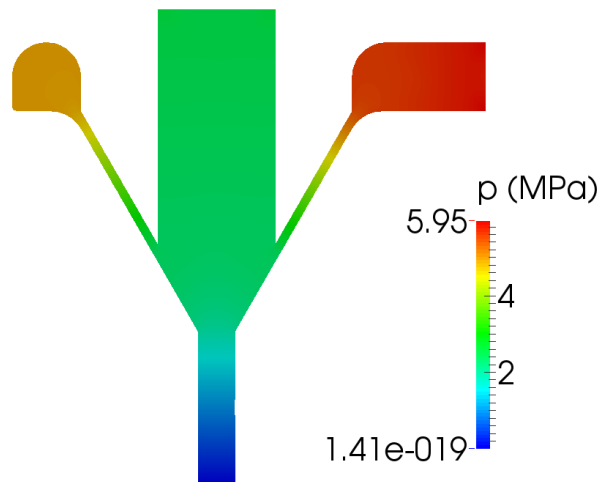


Figure 82 - Pressure field along the distributor in Case 3.

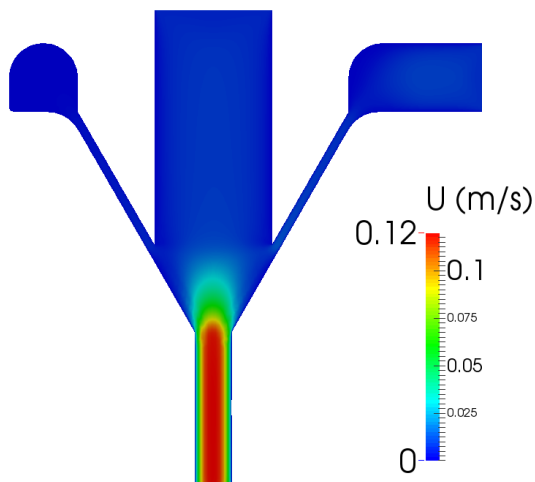


Figure 83 - Velocity profile along the distributor in Case 4.

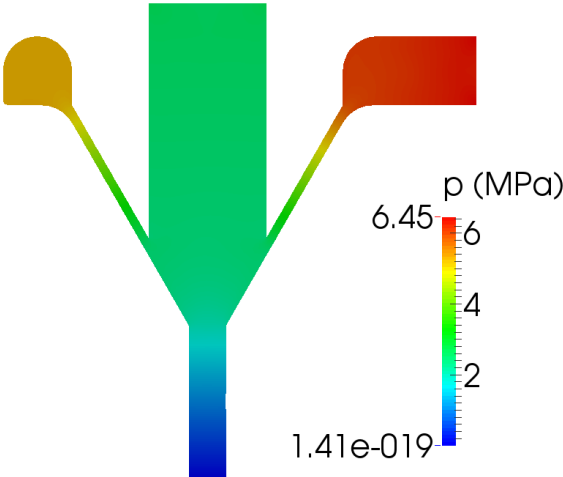


Figure 84 - Pressure field along the distributor in Case 4.

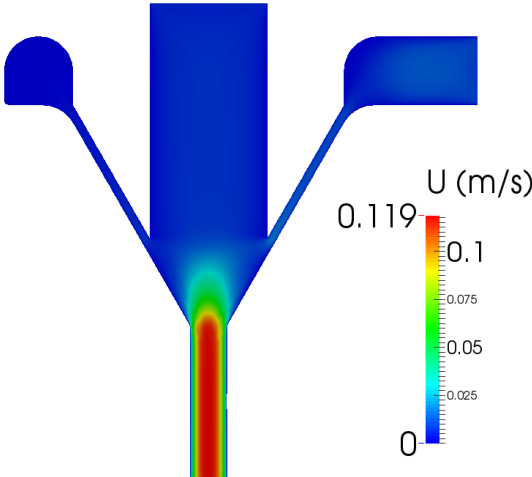


Figure 85 - Velocity profile along the distributor in Case 5.

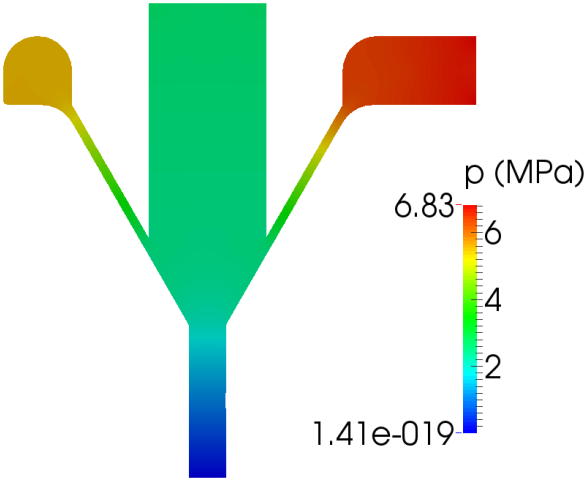


Figure 86 - Pressure field along the distributor in Case 5.

Appendix E – 2D drawings of all components of the filament coextrusion die

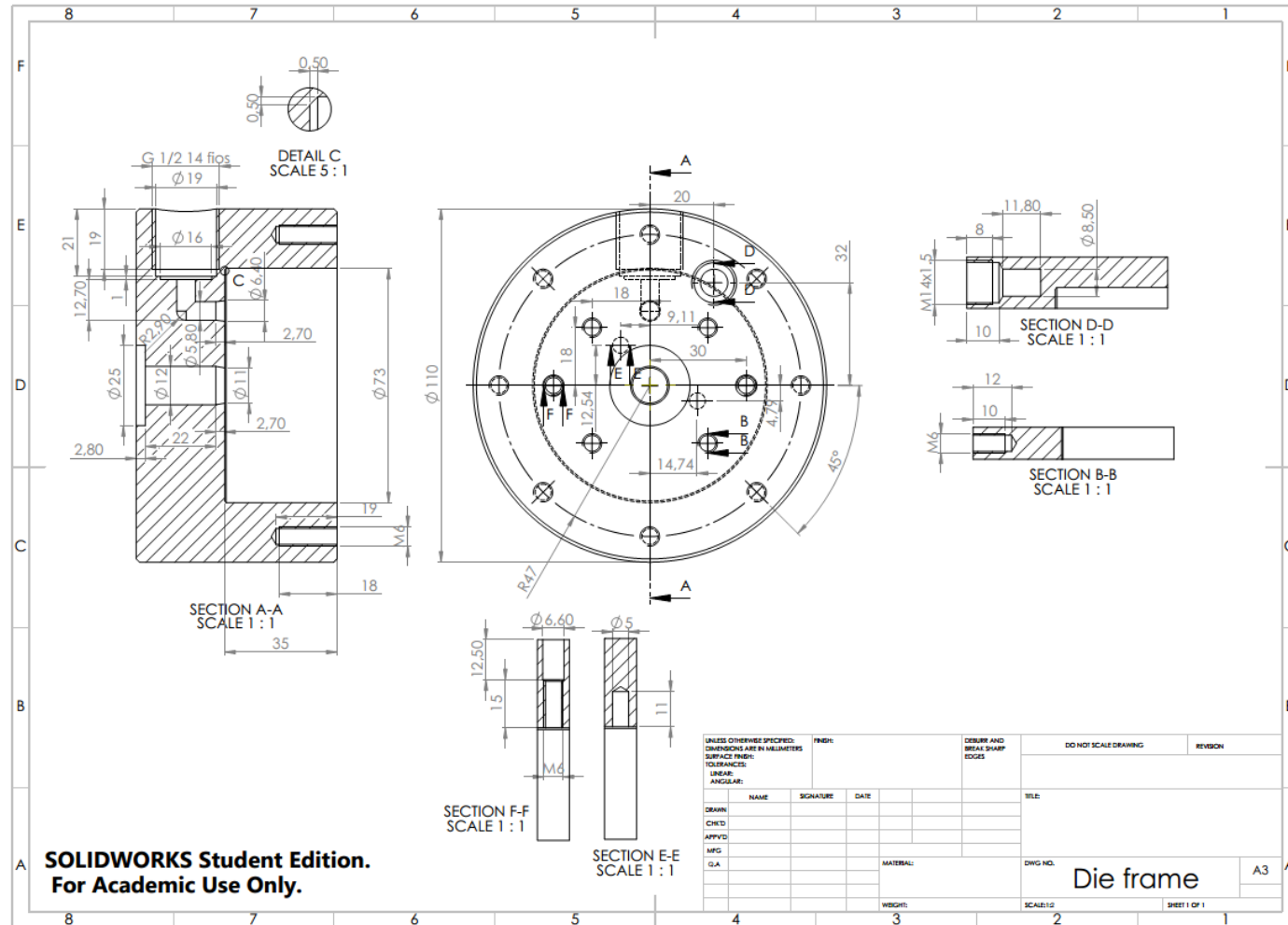


Figure 87 - 2D drawing of the filament coextrusion die frame.

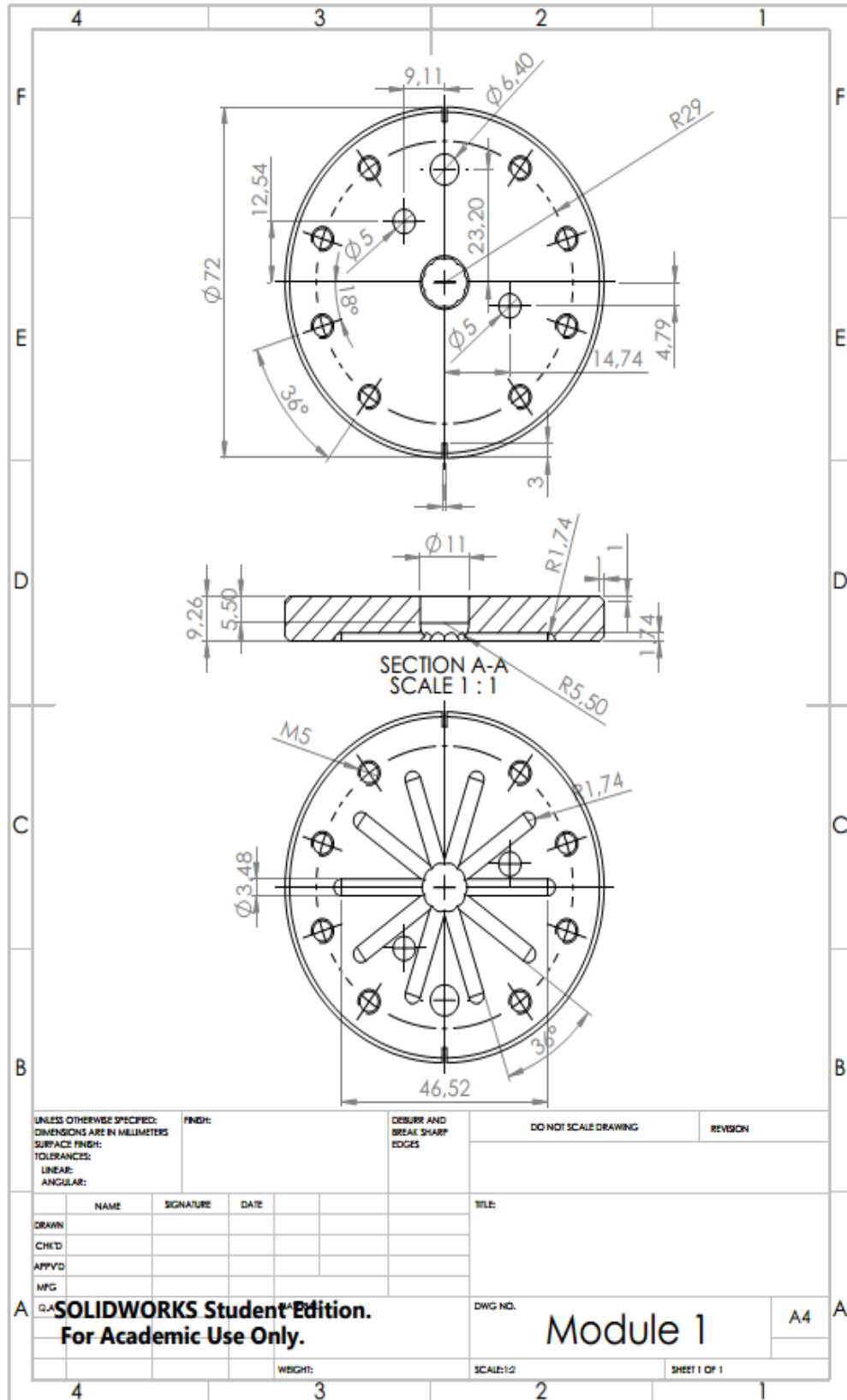


Figure 88 - 2D drawing of the module 1 of the filament coextrusion die.

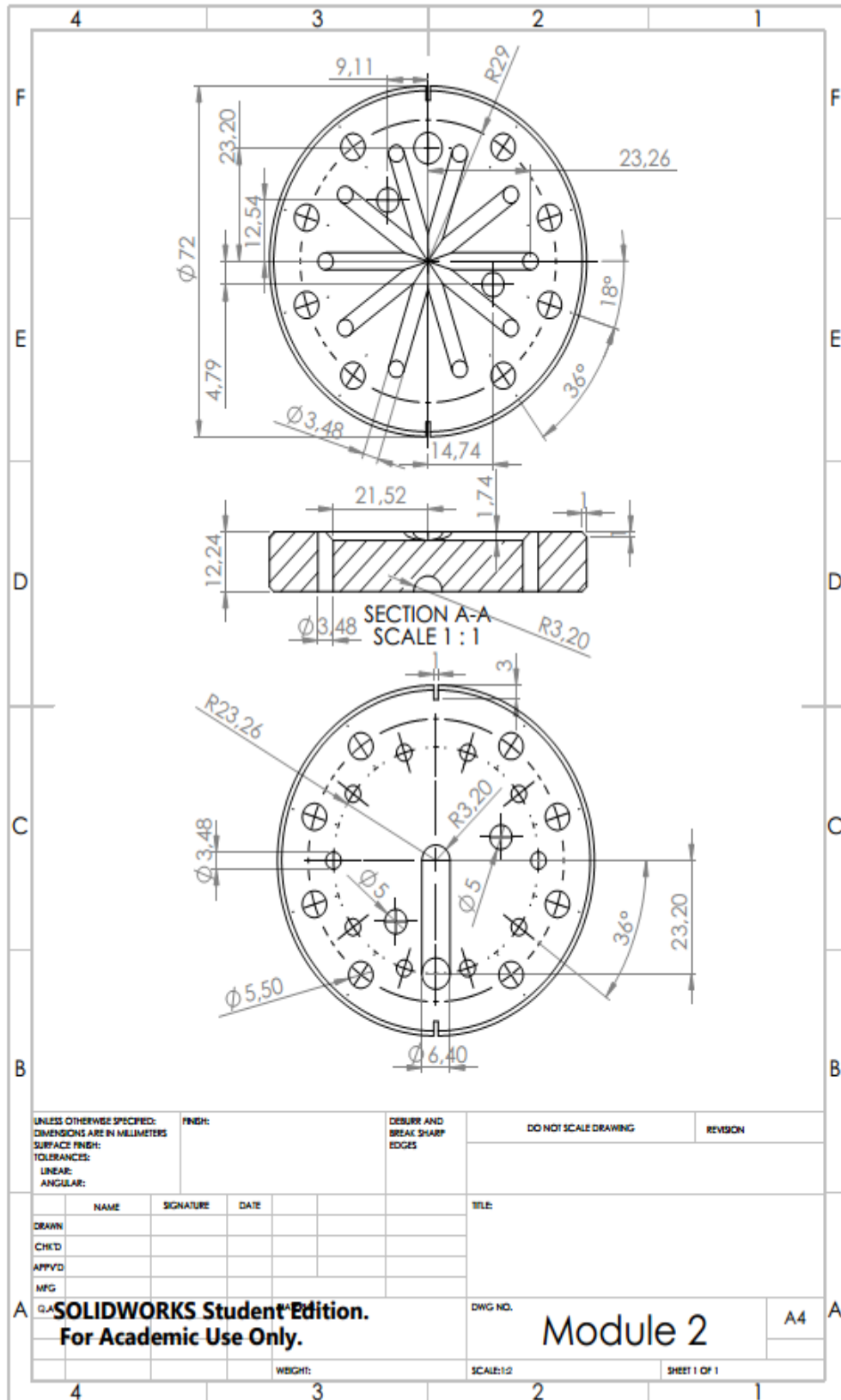


Figure 89 - 2D drawing of the module 2 of the filament coextrusion die.

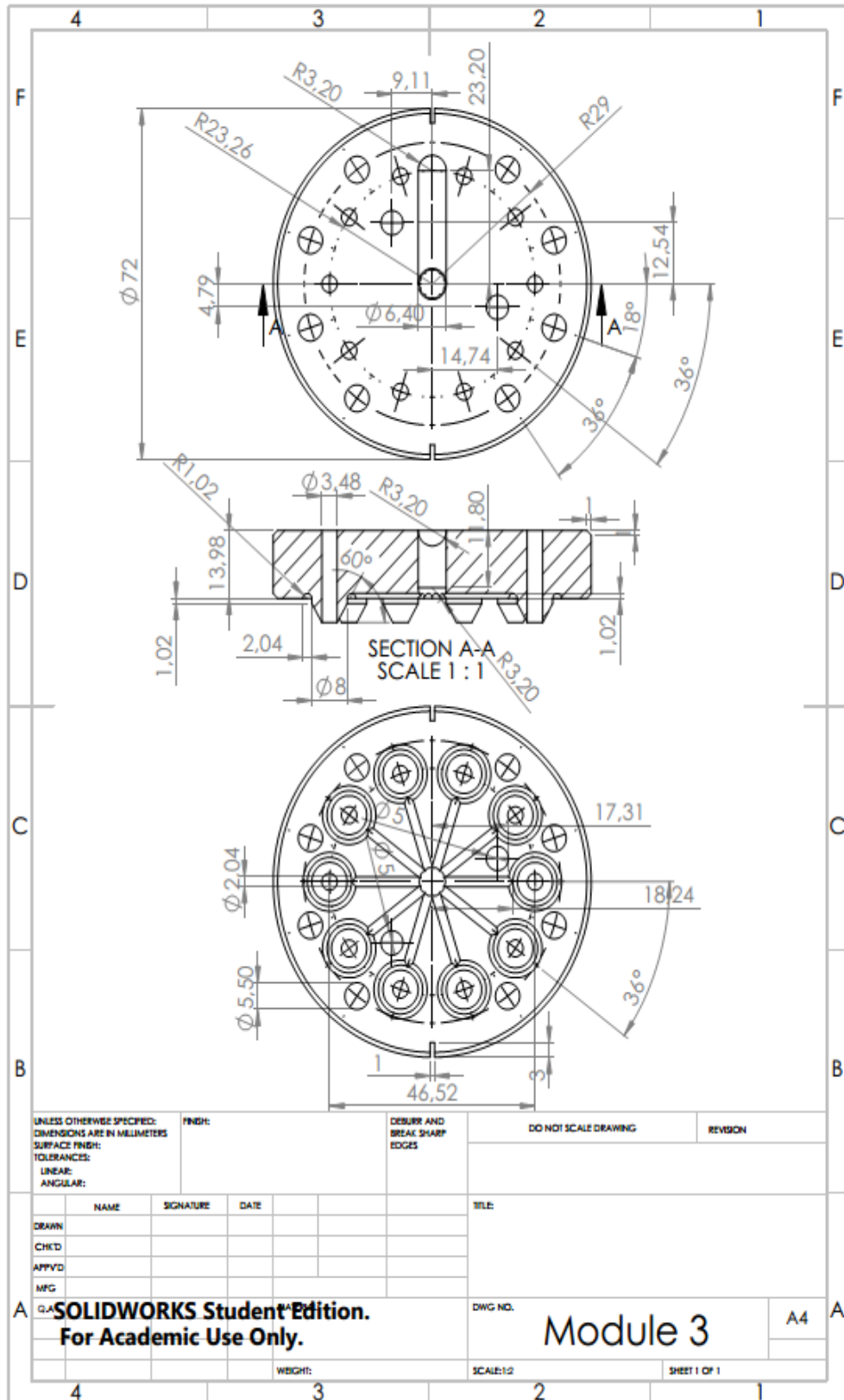


Figure 90 - 2D drawing of the module 3 of the filament coextrusion die.

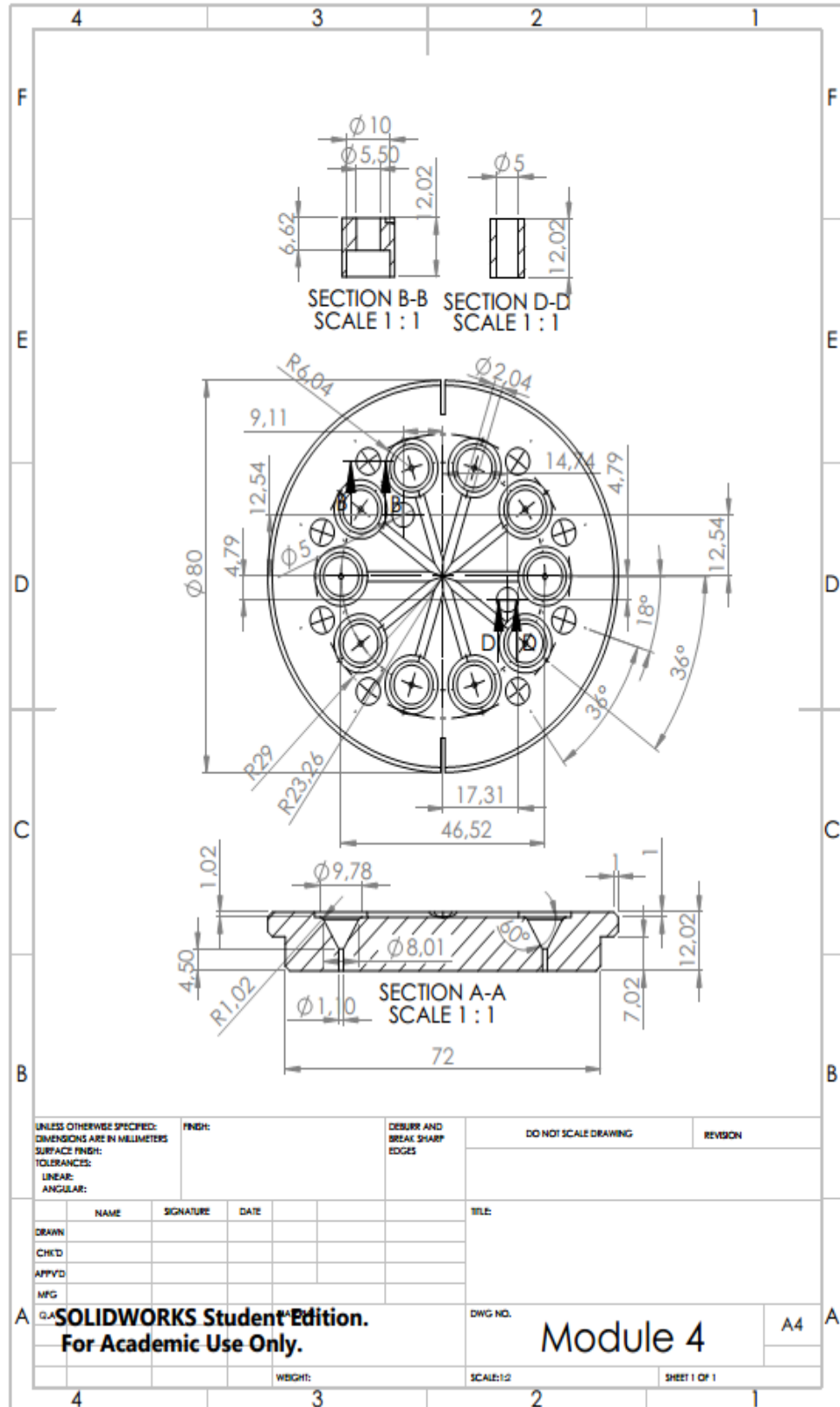


Figure 91 - 2D drawing of the module 4 of the filament coextrusion die.

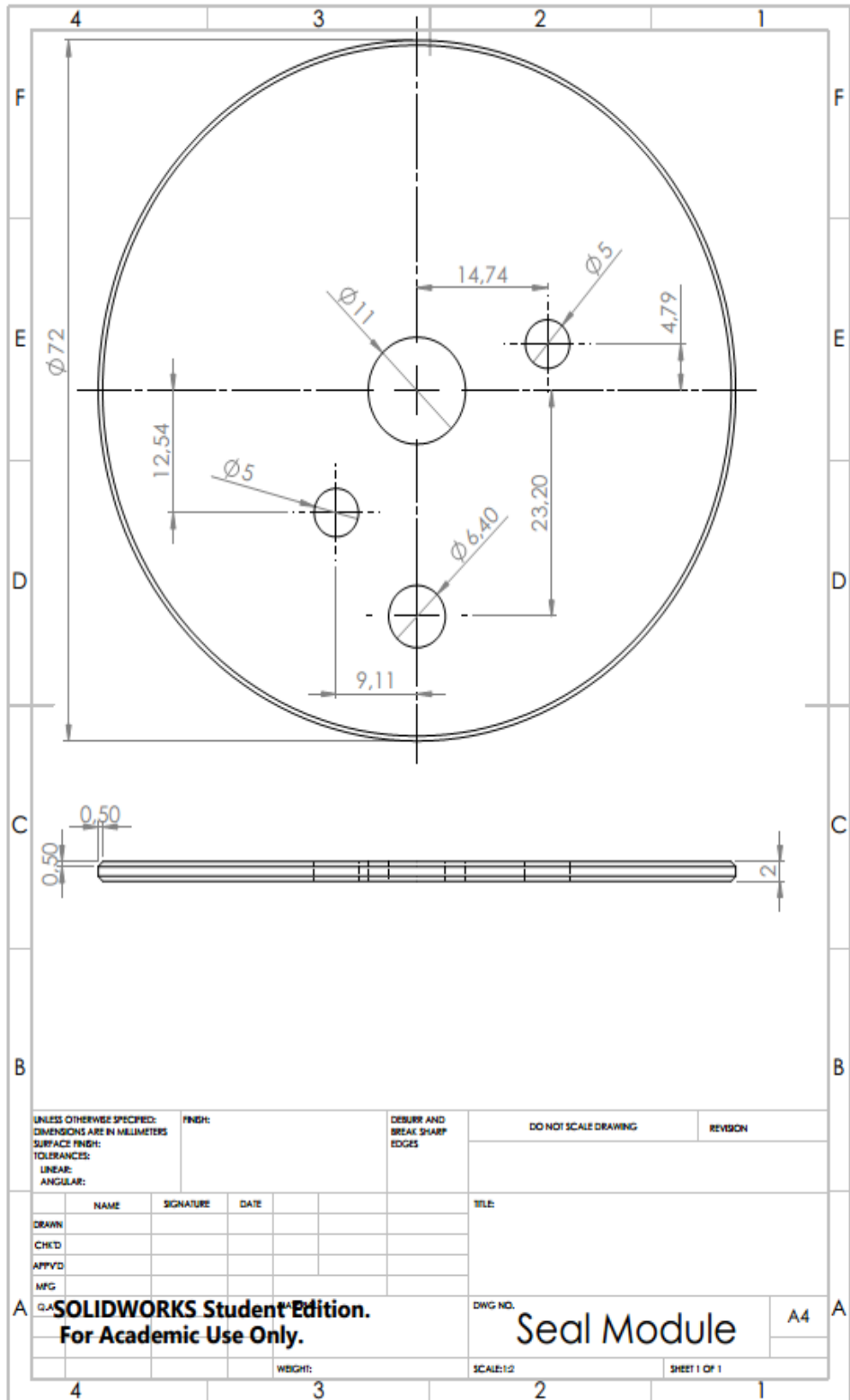


Figure 92 - 2D drawing of the seal module of the filament coextrusion die.

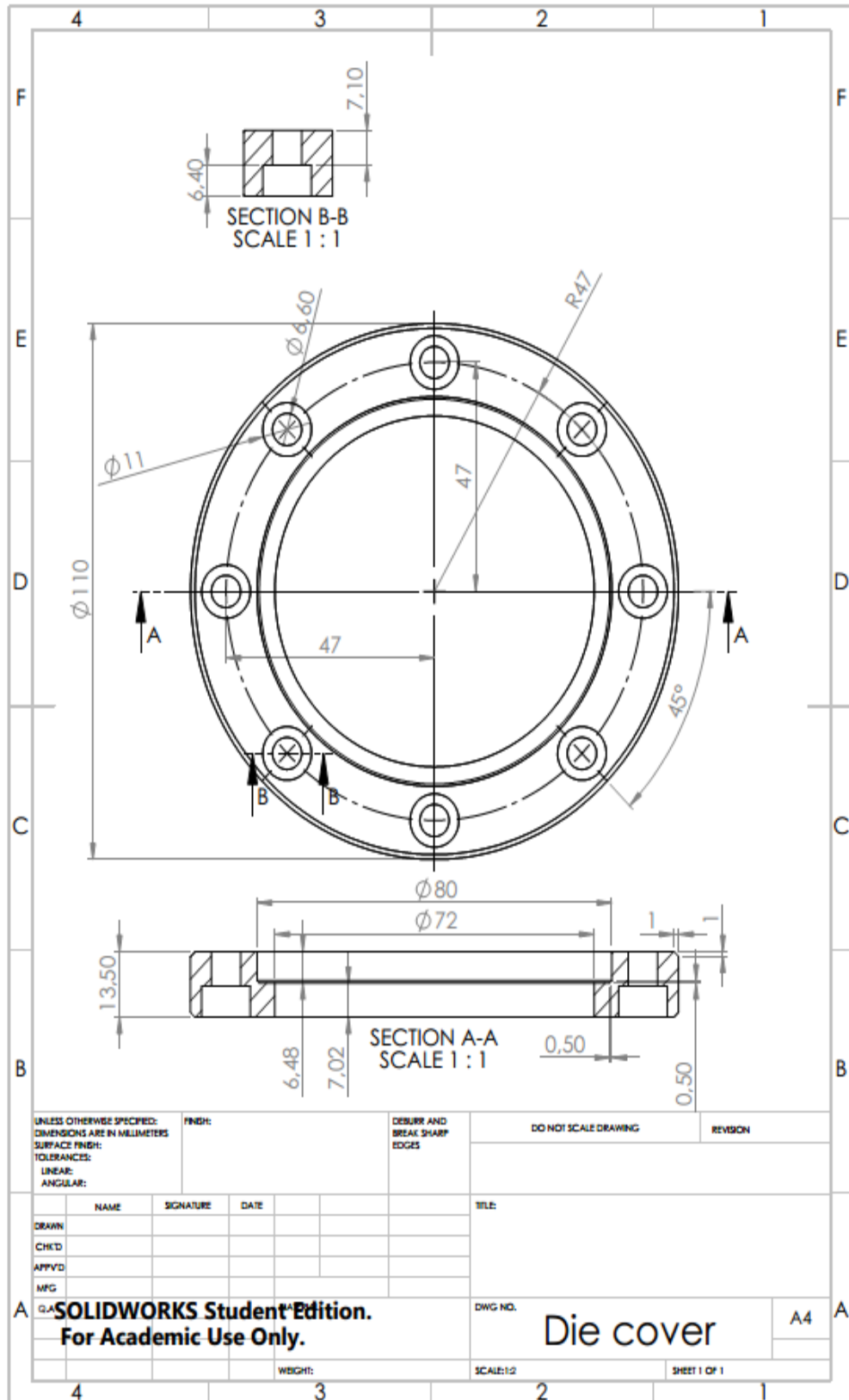


Figure 93 - 2D drawing of the filament coextrusion die cover.